MODELING OF MIXED-MODE DELAMINATION IN COMPOSITE T-JOINTS

A THESIS SUBMITTED TO
THE GRADUATE SCHOOL OF NATURAL AND APPLIED SCIENCES
OF
MIDDLE EAST TECHNICAL UNIVERSITY

BY
HASAN GÜLAŞIK

IN PARTIAL FULFILLMENT OF THE REQUIREMENTS
FOR
THE DEGREE OF MASTER OF SCIENCE
IN
THE DEPARTMENT OF AEROSPACE ENGINEERING

JANUARY 2014

Approval of the thesis:

MODELING OF MIXED-MODE DELAMINATION IN COMPOSITE T-JOINTS

submitted by **HASAN GÜLAŞIK** in partial fulfillment of the requirements for the degree of **Master of Science in Aerospace Engineering Department, Middle East Technical University** by,

Prof. Dr. Canan Özgen
Dean, Graduate School of **Natural and Applied Sciences** _____

Prof. Dr. Ozan Tekinalp
Head of Department, **Aerospace Engineering** _____

Assoc. Prof. Dr. Demirkan Çöker
Supervisor, **Aerospace Engineering Department, METU** _____

Examining Committee Members

Prof. Dr. Altan Kayran
Aerospace Engineering Department, METU _____

Assoc. Prof. Dr. Demirkan Çöker
Aerospace Engineering Department, METU _____

Asst. Prof. Dr. Ercan Gürses
Aerospace Engineering Department, METU _____

Prof. Dr. Levent Parnas
Mechnical Engineering Department METU _____

Prof. Dr. Suat Kadıoğlu
Mechnical Engineering Department METU _____

Date: 29.01.2014

I hereby declare that all information in this document has been obtained and presented in accordance with academic rules and ethical conduct. I also declare that, as required by these rules and conduct, I have fully cited and referenced all material and results that are not original to this work.

Name, Last name: Hasan GÜLAŞIK

Signature :

ABSTRACT

MODELING OF MIXED-MODE DELAMINATION IN COMPOSITE T-JOINTS

Gülaşık, Hasan

M.Sc., Department of Aerospace Engineering

Supervisor: Assoc. Prof. Dr. Demirkan Çöker

January 2014, 125 pages

Stiffened panel, consisting of skin and stiffeners, is the main design option for aerospace structures. When manufactured with laminated composite materials, they provide high strength/stiffness to weight ratio, resulting in high performance and less fuel consumption. T-joint is one of the typical configurations for composite stiffened panels which consist of a skin panel and stiffeners co-bonded or co-cured together with a filler material between them. T-joints are prone to delaminations between skin/stiffener plies and debonds between skin-stiffener-filler interfaces. In this study, delamination/debond behavior of a co-bonded composite T-joint is investigated with 2D finite element method. A commercial FEA software, Abaqus with zero-thickness cohesive elements with bilinear cohesive law is used to simulate delamination/debond at all ply interfaces and bonding lines in the structure. Numerical results for the T-joints show that, delamination/debond initiation and propagation scenarios are different for 0°, 45° and 90° pull loads which simulate different loading conditions in aerospace structures. Different failure initiation mechanisms of the T-joints observed in the literature are captured in a parametric study for 0° pull load with geometry and material property changes. Failure initiation and propagation behaviors, load displacement curves, initial and max failure loads and stress fields are affected by the property changes. Generally, mixed-mode behavior is observed in the failure initiation and propagation stages. Additionally, in the numerical studies of the

DCB, ENF and MMB delamination tests, Abaqus CZM is validated with the analytical solutions and the numerical and experimental data from the literature.

Keywords: Composite Stiffened Panel, T-joint (T-section), Delamination/Debond, Cohesive Zone Method (CZM)

ÖZ

KOMPOZİT T-BİRLEŞMELERİNDE KARIŞIK MODLU DELAMİNASYON MODELLEMESİ

Gülaşık, Hasan

Yüksek Lisans, Havacılık ve Uzay Mühendisliği Bölümü

Tez Yöneticisi : Doç. Dr. Demirkan Çöker

Ocak 2014, 125 sayfa

Güçlendirilmiş panel, kabuk ve güçlendiricilerden oluşan, havacılık ve uzay yapıları için başlıca tasarım seçeneğidir. Kompozit malzemelerden üretildiklerinde, ağırlığa karşı yüksek güç/katılık oranı ile yüksek performans ve düşük yakıt tüketimi sağlarlar. Tipik bir güçlendirilmiş panel konfigürasyonu olarak T-kesitler, kabuk, güçlendirici ve bunların arasında bir dolgu malzemesinin birbirine yapıştırılmasıyla veya birlikte pişirilmesiyle oluşur. T-kesitler, kabuk/güçlendirici tabaka ara yüzeylerinde delaminasyona ve kabuk/güçlendirici/dolgu yapışma yüzeylerinde ayrılmaya maruz kalabilirler. Bu çalışmada, birbirine yapıştırılmış kompozit bir T-kesitin delaminasyon/ayrılma davranışı 2B sonlu elemanlar analiz metodu ile araştırılmıştır. Ticari bir sonlu elemenlar analiz pogramı Abaqus'te, bilineer yapışkan bölge metodu kullanan 0 kalınlıklı yapışkan elemanlar, yapıdaki tüm tabakalar arasında ve yapışma yüzeylerinde kullanılarak, deleminasyon/ayrılma davranışı simüle edilmiştir. T-kesit sayısal sonuçları göstermektedir ki, delaminasyon/ayrılma başlangıç ve ilerleme senaryoları, hava yapılarındaki değişik yük koşularını simüle etmek için kullanılan 0°, 45° ve 90° çekme yük koşullarında farklıdır. Literatürde gözlenen çeşitli T-kesit yıkım başlangıç mekanizmaları, 0° çekme yükü altında, değiştirilmesini içeren parametrik bir çalışma ile yakalanmıştır. Yıkım başlangıç ve ilerleme davranışları, yük-deplasman eğrileri, ilk ve azami hasar yükleri ve gerilme dağılımları malzeme ve geometri özelliklerinin değişimlerinden etkilenmiştir. Yıkım başlangıcı ve

ilerlemesinde, genel olarak karışık modlu bir davranış gözlenmiştir. Ek olarak, Çift Ankastre Kiriş (ÇAK), Son Çentik Bükme (SÇB) ve Karma Modlu Bükme (KMB) delaminasyon test sayısal çalışmalarında, Abaqus yapışkan bölge metodu analitik çözümlerle ve sayısal ve deneysel literatür verileriyle doğrulanmıştır.

Anahtar kelimeler: Güçlendirilmiş Kompozit Panel, T-kesit, Delaminasyon/Ayrılma, Yapışkan Bölge Metodu

to my family

ACKNOWLEDGMENTS

I would like to thank to Assoc. Prof. Dr. Demirkan Çöker for his supervising during the thesis.

I would like to express my gratitude to the examining committee members, Prof. Dr. Altan Kayran, Asst. Prof. Dr. Ercan Gürses, Prof. Dr. Levent Parnas, Prof. Dr. Suat Kadıoğlu and Assoc. Prof. Dr. Ayşegül Askan Gündoğan, for their interest and feedbacks.

I would like to thank to Assoc. Prof. Dr. Ayşegül Askan Gündoğan for her guidance and feedbacks during the writing phase of the thesis.

TABLE OF CONTENTS

TABLES

FIGURES

SYMBOLS AND ABBREVIATIONS

CZM : Cohesive Zone Method

DCB : Double Cantilever Beam

ENF : End Notch Flexure

MMB : Mixed Mode Bending

VCCT : Virtual Crack Closure Technique

VCE : Virtual Crack Extension

FE : Finite Element

FEM : Finite Element Method

XFEM : Extended Finite Element Method

CTOD : Crack Tip Opening Displacement

J : J-integral

2D : 2 dimensional

3D : 3 dimensional

LEFM : Linear Elastic Fracture Mechanics

σ : far field stress

a : major axis of the ellipse / crack length

b : minor axis of the ellipse

r : distance from crack tip

θ : angle with the horizontal axis

F : stress intensity geometry factor

K_I, K_{II}, K_{III} : stress intensity factors for Modes I, II and III

SSY : Small Scale Yielding

K_{IC}, K_{IIC}, K_{IIIC} : critical stress intensity factors for Modes I, II and III

EPFM : Elastic-Plastic Fracture Mechanics

E : young modulus

γ_s : surface energy

γ_p : plastic work

G_I, G_{II}, G_{III} : strain energy release rates for Modes I, II and III

G_{IC}, G_{IIC}, G_{IIIC} : critical energy release rates (fracture toughness) for Modes I, II and III

$K_I^{(total)}$: total Mode I fracture toughness

G_T : total energy release rate

FDM : Finite Difference Method

BEM : Boundary Element Method

σ_1 : longitudinal stress

σ_3 : interlaminar through thickness stress

τ_{23} : interlaminar shear stress

X_t : longitudinal tensile strength

Z_t : interlaminar tensile strength

S_{23} : interlaminar shear strength

F_{xi}, F_{yi} : nodal forces in x and y directions for node i

u_k, u_j, v_k, v_j : nodal displacements in x and y directions for nodes k and j

Π : potential energy

w : strain energy density

T : traction vector

u : displacement vector

Γ : integral path

A : area enclosed by Γ

σ_{ij} : stress component (i=1, 2, 3)

ε_{ij} : strain component (i=1, 2, 3)

u_i : displacement component (i=1, 2, 3)

n_j : normal vector (i=1, 2, 3)

Δs : incremental arc length

δ : crack tip opening displacement / interfacial displacement

σ_y : yield strength

pt : point

t_i^0 : interfacial strength

δ_i^0 : interfacial displacement for damage initiation

δ_i^C : critical interfacial displacement for fracture

δ_i^S : interfacial softening displacement for trapezoidal law

t_i : interfacial traction at an arbitrary point

δ_i : interfacial displacement at an arbitrary point

k_i^0 : penalty stiffness

t_i^0 : interface strength in the specified direction

α : parameter for interfacial stiffness calculation, power law coefficient

t : thickness

d, D : damage parameter

BK : Benzeggah and Kenane

η : BK coefficient

δ_m^0 : interfacial displacement for damage initiation in mixed-mode

δ_m^C : critical interfacial displacement for fracture in mixed-mode

δ_i : interfacial displacement at an arbitrary point in mixed-mode

β : mixed-mode ratio in terms of displacement

NR : Newton-Raphson

L : length

b : specimen width

h : thickness of sublaminate

a : initial delamination

E : young modulus

G : shear modulus

MPa : megapascal

GPa : gigapascal

G_c : mixed-mode fracture toughness

v : poisson's ratio

ASTM : American Society for Testing of Materials

MBT : Modified Beam Theory

δ : prescribed displacement

χ : crack length correction parameter in MBT

Γ : transverse modulus correction factor in MBT

C_I, C_{II} : Mode I and Mode II compliance

I : moment of inertia

CPE3 : 2 dimensional, triangular, linear, 3 node, plain strain elements

CPE4 : 2 dimensional, quadrilateral, linear, 4 node, plain strain elements

CPE4R : 2 dimensional, quadrilateral, linear, 4 node, reduced integration plain strain elements

CPE4I : 2 dimensional, quadrilateral, linear, 4 node, incompatible mode plain strain elements

COH2D4 : 2 dimensional, quadrilateral, linear, 4 node, cohesive elements.

BC : Boundary Condition

l_{CZ} : cohesive zone length

M : cohesive model parameter for cohesive length calculation

v : viscosity

P	: load
P_I, P_{II}	: Mode I and Mode II load for the MMB specimen
δ_I, δ_{II}	: Mode I and Mode II displacement for the MMB specimen
m	: mixed-mode ratio in terms of energy
c	: MMB specimen lever length
S_{22}	: normal stress
S_{12}	: shear stress
NCF	: non-crimped fabric
t	: thickness
L_s	: length of the skin
t_s	: total thickness of the skin
L_st	: distance between the stringer flange tips
t_st	: total thickness of one stringer leg
h_st	: height of the stringer
w	: width of the T-section
θ	: angle with the horizontal axis

CHAPTER 1

INTRODUCTION

1.1 Problem Definition

Stiffened panels, composed of a thin skin and stiffeners as shown in Figure 1.1, are the main design option for aircraft components including fuselage, wings and control surfaces. In the last decades, aircraft companies started to manufacture stiffened panels by using laminated composite materials for their advantageous characteristics.

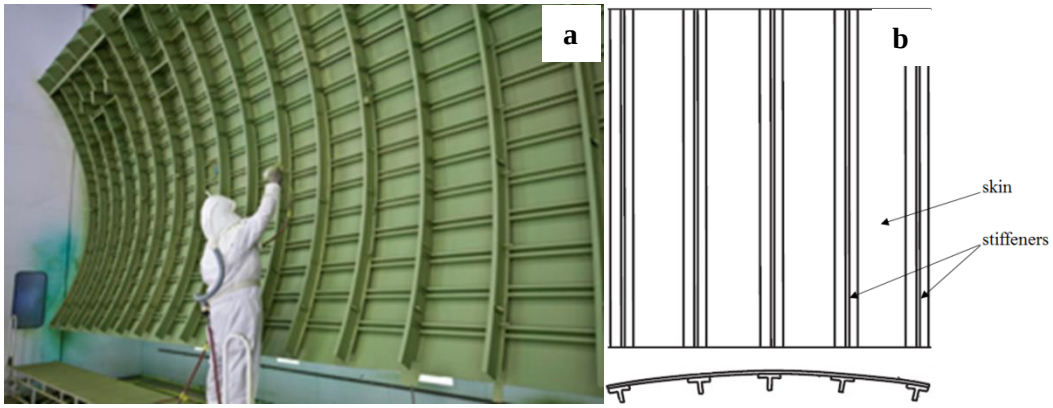

Figure 1.1- (a) aircraft fuselage section, (b) a T-stringer stiffened panel [6]

Laminated composite materials are manufactured by stacking individual plies on top of each other in different angles as seen in Figure 1.2. Laminated composites are mainly used for their high strength/stiffness to weight ratio which provides high performance and less fuel consumption for aero vehicles. Some other advantageous characteristics of composites are: superior fatigue behavior, corrosion resistance, reduced magnetic signature, manufacturing abilities, etc. [13, 28, 29]. Therefore, there is an increasing demand for composite materials especially in aerospace, wind turbine, marine and automobile industries. For instance, Boeing 787 is composed of 50% composite materials as seen in Figure 1.3, offering 20% less weight and less maintenance cost with a comparable product [29].

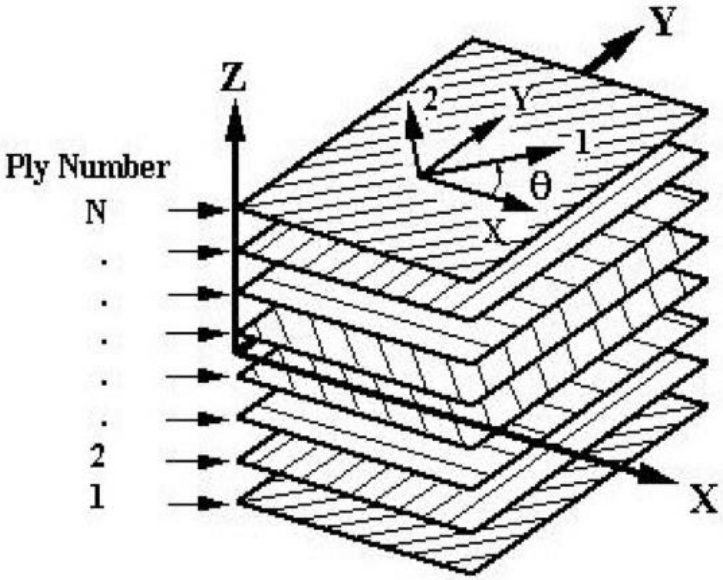

Figure 1.2- Composite laminate with unidirectional plies in different orientations

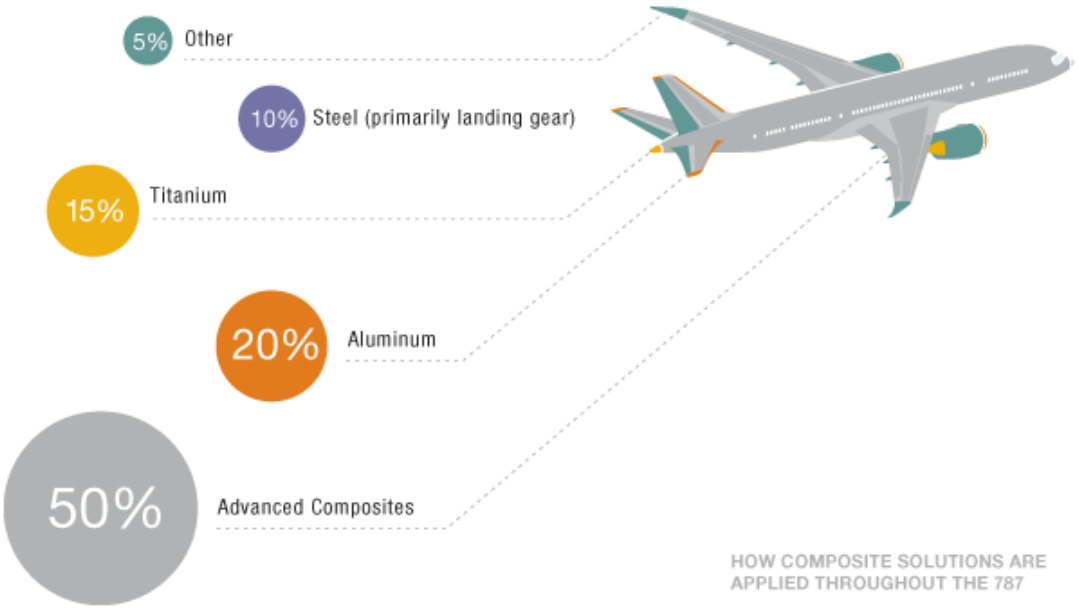

Figure 1.3- Composite material usage in Boeing 787 [29]

In aerospace industry, composite parts are generally attached to each other with fasteners which create stress concentration around the fastener holes. The stress concentration in metallic materials is handled to some degree with plastic deformation but it is an important problem for composite parts because of the brittle nature of the composite materials. Therefore, thicker sections are used in composite structures to prevent the failure around the fastener holes. This situation

brings extra weight to structures which reduces the weight advantage of the composites. Therefore, it is a good choice to bond the stiffeners to the skin especially for composite structures.

Despite their advantages, laminated composites also have some weak points. They are dominated by matrix properties in through thickness direction and in general, there is no other strengthening mechanism. This situation makes them relatively weak in through thickness direction. Therefore, plies separate from each other under loading which is known as delamination. Debond of the stiffeners from the skin in the stiffened panels can also be classified as delamination. Some material, design and manufacturing aspects are considered as critical for delamination/debond as seen in Figure 1.4: skin-stiffener section, curved laminates, ply drop-off, manufacturing defects, drilling, etc. [11, 27, 31]. Under various loading conditions (mechanical, buckling, cyclic, hydrothermal, low velocity impact, bird strike, underwater explosion, lightning, etc. [6, 11-15, 30, 31, 58]), interlaminar normal or shear stresses are generated between the plies in these critical regions which cause delaminations/debonds. Delamination/debond reduces the stiffness and strength of the structure as the delaminated area gets larger. Structural integrity of the structure is lost and sudden collapse of the structure is observed at a critical level of the delaminated area.

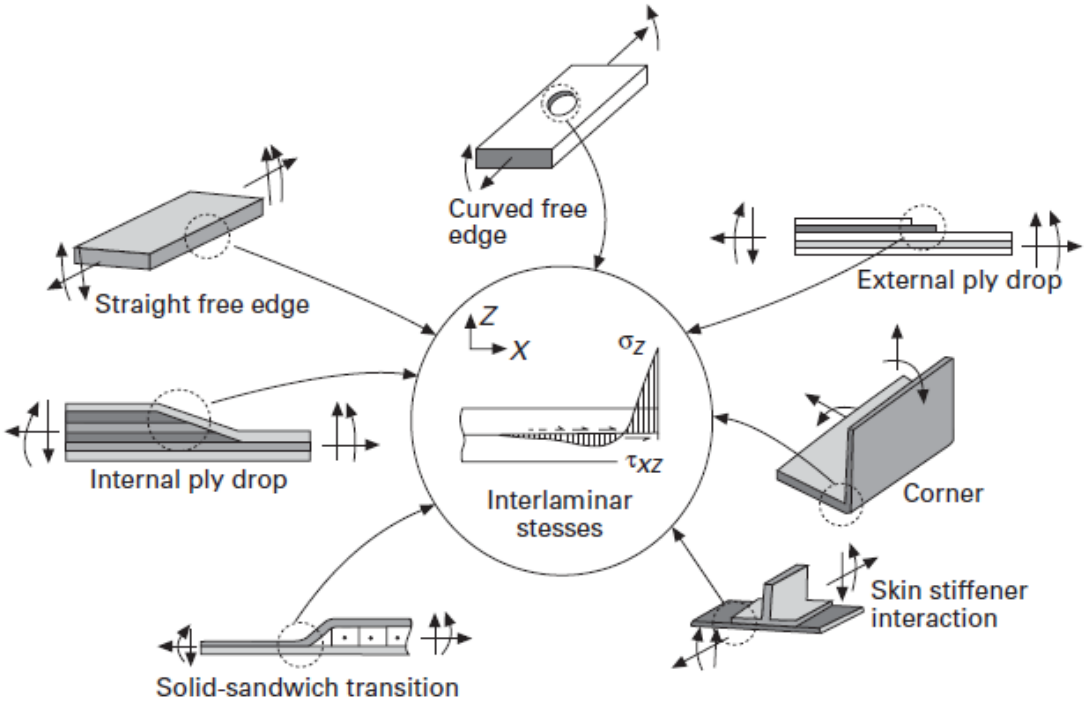

Figure 1.4- Sources of delaminations at geometric and material discontinuities [27]

T-joint (T-section, tee joint), as a typical example of composite stiffened panels, is prone to delamination/debond. T-joints are composed of a skin (panel or hull in marine industry) and stiffeners (stringer in aerospace, overlaminate in marine industry) co-cured or co-bonded together with a filler (noddle, deltoid or fillet region) between them as seen in Figure 1.5. In T-joints, because of the stiffness difference between the skin and the stiffeners, a complex 3D stress state is generated in the structure. This makes the T-joint a critical delamination/debond region. Delaminations can be seen between the skin or stiffener plies, debonds can be seen between the skin-stiffener-filler interfaces. Generally, the delamination/debond process results in a sudden collapse of the T-joint as seen in Figure 1.6.

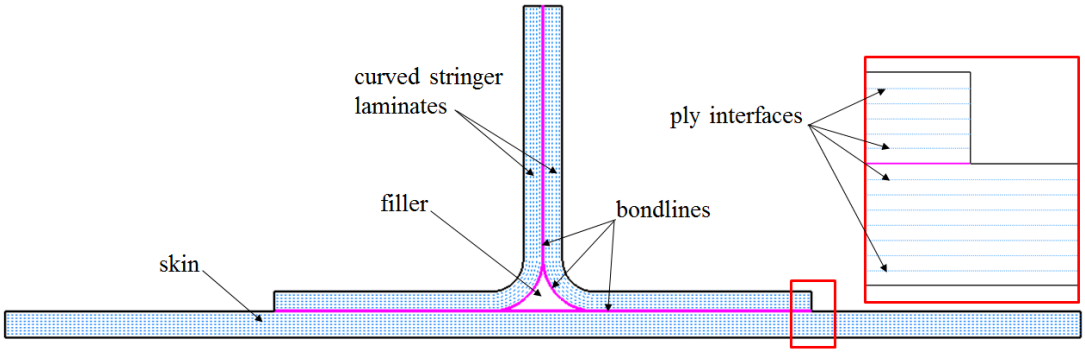

Figure 1.5- Geometry of a typical T-joint

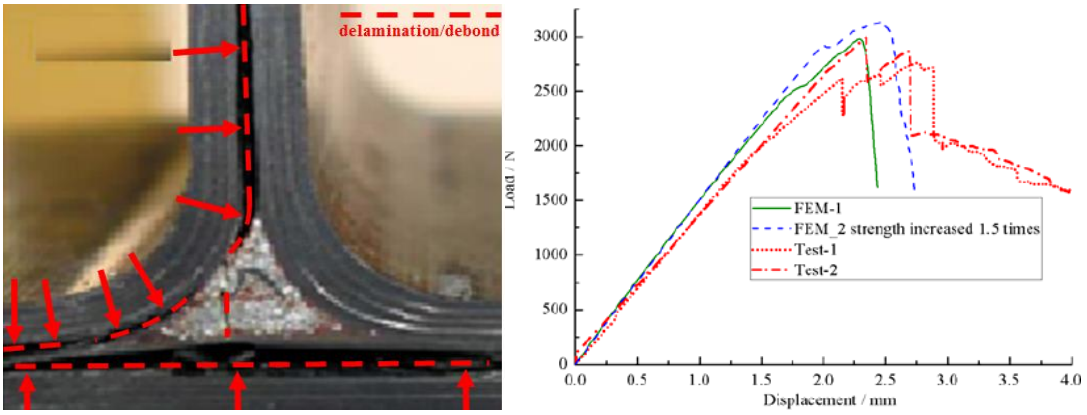

Figure 1.6- Delaminated T-joint (left), numerical and experimental load-displacement curves of the T-joint (right) [16]

In this study, delamination/debond behavior of a composite T-joint is investigated with Cohesive Zone Method (CZM) in 2D by using Abaqus

commercial finite element (FE) software. Quasi-static loads are applied and implicit nonlinear solutions are carried out in the numerical simulations. Load-displacement curves, failure initiation and propagation scenarios are investigated under 0°, 45° and 90° pull loads. In a detailed study for the 0° pull load, delamination/debond initiation mechanisms observed in the literature are captured with a parametric study in which geometry and material properties are changed. Additionally, benchmark tests are conducted for Double Cantilever Beam (DCB), End Notch Flexure (ENF) and Mixed Mode Bending (MMB) delamination tests for the validation of the Abaqus CZM.

1.2 Motivation

Even tough, composite T-joints offer many advantages, delamination/debond in the structure may reduce the effectiveness of these geometries. A detailed delamination/debond study of the T-joints under different loading conditions and in different design configurations is necessary to reveal the initiation and propagation scenarios, critical loads and critical locations of the structure. Such an investigation can help to build safer composite structures with high performance, less production and maintenance cost which are crucial in aerospace industry.

T-joint study can also be a base for more advanced composite T-joint investigations. Structural behavior can be investigated further under fatigue and dynamic loadings. Additionally, composite material fiber/matrix damages can be included for more realistic numerical applications including complete aircraft components in 3D.

1.3 Objective

The overall objective of this study is to investigate the failure of the T-joints due to delamination/debond mechanism by using FEM with CZM. More specifically, the objectives are:

- to observe the delamination/debond initiation and propagation mechanisms of the T-joint for 0°, 45° and 90° pull load conditions in a preliminary investigation.
- to observe the complete failure process until the collapse of the structure and capture the residual strength of the structure after delaminations/debonds.
- to further investigate the failure initiation and propagation for 0° pull load in detail with the stress fields captured during the failure initiation and propagation processes.
- to capture the 4 different failure initiation mechanisms of T-joints observed in the literature by changing parameters of the model such as: composite and adhesive material properties, ply sequence, stringer thickness, etc.
- to extract design recommendations for low weight and high performance of the T-joints.

Additionally, the intermediate objectives are:

- to validate the Abaqus CZM by DCB, ENF and MMB benchmark studies.
- to investigate the effects of the cohesive parameters on the numerical results of the DCB, ENF and MMB tests.

1.4 Outline

In Chapter 2, the literature survey of the delamination/debond studies of T-joints is presented. Brief summaries of the articles are provided from aerospace, marine and wind turbine industries.

In Chapter 3, basic concepts of the fracture mechanics are presented for a better understanding of delamination/debond mechanism. Some common numerical methods are introduced which are used for delamination initiation/propagation simulations. Strength based approach, Virtual Crack Closure Technique (VCCT), Virtual Crack Extension (VCE), stress and displacement correlations, crack tip opening displacement (CTOD), J-integral and Extneded

FEM (XFEM) methods are introduced briefly. A detailed description of the CZM is provided at the end of the chapter.

In Chapter 4, DCB, ENF and MMB test methods are introduced which are used for the delamination resistance of the composite materials for Mode I, Mode II and Mixed-Mode I-II, respectively. Benchmark studies of the tests are carried out for the validation of the Abaqus CZM. Analytical solutions and data from literature are compared with the numerical solutions of the Abaqus CZM. Sensitivity analyses are carried out to see the effects of different cohesive parameters on the results of the DCB, ENF and MMB simulations.

In Chapter 5, the T-joint investigation is presented. Delamination/debond initiation mechanisms observed in the literature are presented at the beginning of the chapter. T-joint specimen geometry and material properties are given next which are used for the numerical study. Delamination/debond behavior of the T-joint for 0°, 45° and 90° pull loads are then investigated and load-displacement curves are provided. The results of FE models with and without cohesive layers are compared to see the applicability of the cohesive model. Delamination/debond initiation mechanisms for the T-joints are captured for 0° pull load with a parametric study including geometry and material property changes. Load-displacement, stress fields, failure initiation and propagation behaviors are discussed.

In Chapter 6, summaries and conclusions of Chapters 4 and 5 are provided.

In Chapter 7, future works that are planned to be carried out for the T-joints are listed.

CHAPTER 2

LITERATURE REVIEW

Various studies are available in literature related with composite T-joints and delamination/debond process in laminated composites. In below paragraphs, articles from wind turbine, marine and aerospace industries are summarized.

Wind turbine industry

Mandell et al [11] investigated the delamination problem in wind turbine blades under static and fatigue loadings. They studied a T-joint under tensile pull load experimentally and also numerically with VCCT by placing an initial crack at the stress concentration region. In experiments, it was seen that crack grew in the bend region in upper and lower directions. They observed that tougher matrices showed higher load capacity for static loading and perform better under fatigue loading. In DCB and ENF experiments, they observed that as crack extended, emerging secondary cracks in matrix or adjacent plies or fiber bridging increased the fracture toughness. They stated that manufacturing problems such as porosity may cause delamination, environmental factors and fatigue loading can also cause delamination at low load levels.

Marine industry

Phillips and Shenoi [12] studied T-joints for marine applications under 45^{o} pull load (simulating tensile and side bending loads) and 3-point bending (simulating hydrostatic or dynamic loading). For pull loading test, they observed delamination in the bend region between the inner plies of the overlaminate. In 3-point bending test, a crack appeared in the fillet, delamination was seen then in the overlaminate. In 2D FE studies, they used strength and fracture mechanics based approaches for delamination investigation. In strength based approach, they compared the stresses in the structure with interlaminar and ultimate tensile strengths. In fracture mechanics based approach which utilized triangular crack tip elements; strain energy release rates (or J-integral) were calculated. Both strength

and energy approaches gave similar results in predicting crack growth. They observed that at the first stages of the loading, high through thickness stress cause delamination in the inner plies of the bend and for further loading through thickness stress decreased and in plane stresses increased at the outer plies. They stated that inconsistencies between experimental and numerical results in the fillet region were caused from the voids in the fillets acting as stress raisers. It was also stated that, interfaces of plies (especially with different materials) shows high stresses and damage was likely to occur in those regions.

Dharmawan et al. [13] studied geometry and damage effects on a composite marine T-joint for 3-point bending load with an alternative triangular shaped overlaminate. In their parametric FE study, they changed overlaminate angle, hull thickness and debond between filler and overlaminate. By changing the overlaminate angle and debond size, they observed a change in the strain distribution in the overlaminate. By changing the hull thickness, they observed that strains were reduced nearly for all regions, but the effect was less pronounced for further increase which showed that hull can be considered as rigid after some thickness. Strain gage measurements for simply supported and clamped conditions were taken and it was observed that numerical results fell between the results of the two boundary conditions considered.

Li et al. [14] also studied the fracture behavior of composite maritime T-joints for tensile pull load. They investigated the effects of initial debonds on delamination/debond process with VCCT. They observed different failure loads and propagation mechanisms by considering initial debonds between overlaminate-hull, overlaminate-filler, filler-hull, and overlaminate-bulkhead. They stated that propagation and failure loads decreased with increasing debond and small debonds gave approximately the same results with intact structure. They stated that skew loading present in the experiment affected the results and applying skew loading to FE models gave closer results to experiments.

Hawkins and Shenoi [15] studied the effect of geometry on T-joint performance with a parametric study under 0° and 90° pull loads simulating tensile and side loading. They used 3D FE models including filler plasticity. In comparative studies, fillet radius, overlaminate thickness and gap size between hull and filler were changed. As overlaminate thickness and fillet radius increased,

overall deflection, in-plane stress and fillet stress decreased. They observed that decreasing the fillet radius and increasing overlaminate thickness increased through-thickness stresses. They observed also that gap size had no effect on overall deflections or stresses in the overlaminate.

Aerospace industry

Orifice et al. [1-10] investigated the post buckling behavior of composite stiffened panels with numerical and experimental studies in a series of papers under a European Commission Project, COCOMAT (Improved MATerial Exploitation at Safe Design of COmposite Airframe Structures by Accurate Simulation of COllapse). They took the effects of material degradation and delamination/debond process into account in numerical simulations. Their studies ranged from a coupon specimen to a complete stiffened panel. At coupon level, Orifice et al [1, 2, 5] considered three loading types, asymmetric, symmetric pull and symmetric push which are caused from global buckling of the panel. Various parameters were investigated (T-section, L-section, stiffener flange drop-off, ply sequence, co-cured/co-bonded specimens and different ply materials) and it was seen that all these parameters affected the results. A classification of failure modes was done as in Figure 2.1. In local numerical models, they used a strength based failure criterion, Tsai-Hill for delamination/debond initiation prediction. Experimental scatter and difference between numerical analysis were considered mainly from the geometric and material property deviations; thickness and radius changes, resin flows at skin-stiffener intersections, transverse strength values differing 25% from different labs. They also stated that transversely isotropic assumption of laminates could affect the results also. In numerical analysis, friction and slippage were seen to affect the results much which were present in the experiments. At global fuselage level, Orifice et al. [3, 6, 7, 8, 9, 10] followed two approaches. In global-local approach, displacements obtained from global model applied as BCs for a local 3D analysis and Tsai-Hill criterion was used for delamination/debond initiation prediction. In degradation approach, global model with VCCT method was used for simulating the crack propagation. In their own VCCT code, they considered the effect of crack front shape on strain energy release rate. Both in these approaches, they took the ply damage into account with Hashin Criterion accounting fiber and matrix cracking, fiber-matrix shearing. They

tested intact and debonded panels in [6]. It was observed that experimental and numerical results agreed quite well in terms of stiffness, buckling initiation, collapse load, but the buckling patterns did not match for the intact panel. They observed voids in the bonding material and stated that bonding quality affected the results. Also 0^o ply interface fracture toughness was used in the study which was considered as conservative.

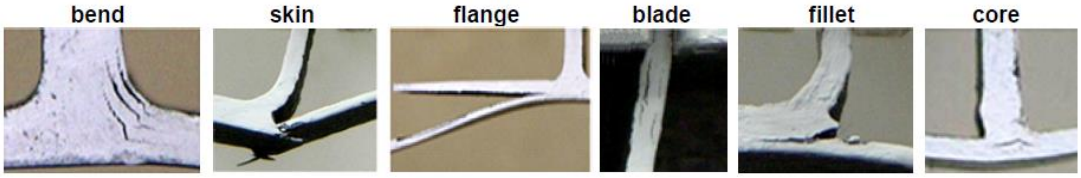

Figure 2.1- Failure mechanisms in composite panel sections [5]

Cui et al. [16] performed a series of 3D FE simulations with CZM to evaluate the influence of matrix, adhesive, filler and the radius on the strength of T-joint under tensile pull loading as seen in Figure 2.2. In their parametric study, they observed that increasing the radius increased the load capacity. Increasing the filler stiffness increased the structure stiffness to a certain extent but the carried load remained almost the same and the influence become negligible for very high and very low values. They also observed that reducing fracture toughness and strength of filler, adhesive or matrix, reduced load carrying capacity and changed delamination/debond behavior. They stated that fiber bridging and rupture complicates the delamination process at the later stages of the numerical simulations.

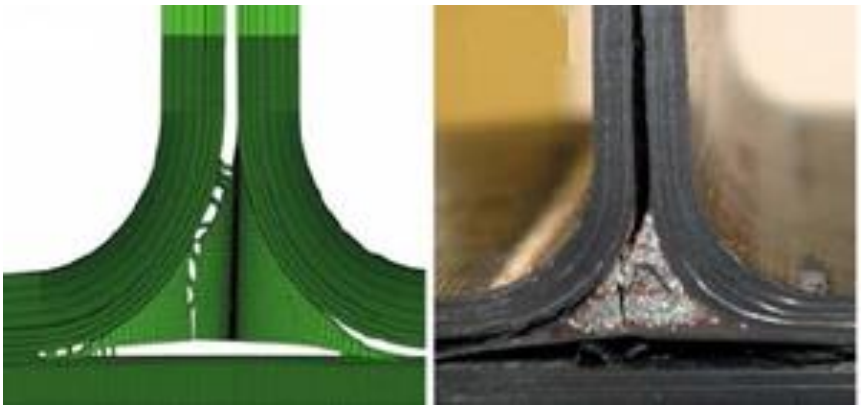

Figure 2.2- Fracture of T-joint captured with CZM (left) and experimental result (right) [16]

Bruyneel et al. [24] investigated a T-joint with 3D FE model with VCE and CZM. They observed that, in terms of propagation load and initial critical location, VCE and CZM gave similar results. They stated that after the first damage occurred between the noddle and the stiffener, CZM was able to predict the crack to propagate between the cap and the stiffener. It can be stated that VCE had the advantage of plotting strain energy release rates in detail at the crack fronts.

Davies and Ankersen [55] investigated a T-joint under tensile and shear loadings experimentally and numerically. They had a good agreement between numerical and experimental results. Delamination initiation was predicted at the noodle interfaces. Further growth was also simulated with the use of CZM. They stated that because of long computation time, they used Abaqus Explicit for some numerical simulations instead of Abaqus Standard [22].

Helenon et al. [18] investigated composite T-joints under pull loading experimentally and numerically. They take the residual thermal stress from the cure cycle into account in numerical simulations. In experiments, delaminations were observed between the stringer plies with a cross ply crack. In numerical analysis, they predicted the crack locations from the stress field of 2D and 3D FE models and then they inserted cohesive layers to the predicted crack locations in the 3D model. They observed that including the cross ply crack in the experiment in FE model decreased the initiation load a considerable amount and gave much closer result to the experiment.

Rao et al. [58] investigated composite wing T-joints experimentally and numerically for pull loading in hydrothermal environments. They also studied Z-stitching which is a method used to enhance delamination/debond strength.

Trask et al. [61] investigated the influence of manufacturing defects in the deltoid area on the failure of composite T-joints.

Conclusions from the literature survey

Based on the literature survey, some important points of the delamination/debond studies can be listed as below:

- Material discontinuities (ply drop-off), geometric discontinuities (skin-stiffener intersection, curved laminates, free edges), manufacturing defects (waviness, porosities, voids), manufacturing methods (drilling) are critical in terms of delamination/debond.
- High normal and shear stress components in through thickness direction are the causes of delamination/debond.
- DCB, ENF and MMB tests are the generally used tests for delamination/debond characterization in composite materials.
- Numerical and experimental delamination/debond studies are available for static, fatigue and dynamic loadings.
- In the past few decades, strength based methods were used generally for numerical delamination/debond simulations. In these days, VCCT and especially CZM are being increasingly used. J-integral and VCE methods are also used in some studies. There are some early use of XFEM for delamination/debond in composite laminates.
- In numerical and experimental delamination/debond investigations, angle pull/push loads (0^0, 45^0, 90^0) and 3-point bend load are the generally used load cases.
- 2D FE solutions are generally used in T-joint studies. Some 3D solutions are also present, even composite full scale component tests are simulated.
- In experiments, measurements are taken with load cells and strain gages. Microscopic investigations, ultrasonic measurements and digital image correlation techniques are also utilized in some experiments.
- Bend region (inner plies, filler-stringer interface) and stringer flange tips seem to be the critical locations of T-joints for delamination/debond initiation and propagation.
- Experimental scatter and difference from numerical analysis are considered mainly from the geometric and material property deviations; thickness and radius changes, manufacturing defects, resin flows at skin-stiffener intersections, different transverse strength values from different labs, friction/slippage/skew loading in the experiments, etc.

- At the beginning of a failure scenario, delamination/debond is the main source of load drop. As load is increased, fiber/matrix damages, fiber bridging and secondary cracks complicate the failure process and thus numerical results deviate from the experiments. Additionally, 0^0 laminate fracture toughness test values are used in numerical simulations which are conservative for angle ply laminates.
- Including fiber/matrix damages, filler plasticity and filler fracture in numerical simulations increase the correlations with the experiments.
- Some parametric studies are available in the literature investigating the bend radius, skin thickness, stringer thickness, debond between parts, material fracture toughness and strength etc. It seems that increasing debond decreases the load capacity. Increase in skin or stringer thickness decreases overall deflection and in plane stresses. Decreasing radius and increasing stringer thickness increase through thickness stresses and cause delamination/debond. Increasing the filler stiffness increases the structure stiffness to a certain extent. Decreasing the fracture toughness and strength of the filler, adhesive or matrix reduce load carrying capacity and change delamination/debond behavior.
- Z-stitching, Z-pins, tougher matrices, alternative joint configurations, stringer flange ply drop offs, ply sequence modification, ply material change are used for delamination/debond prevention.

CHAPTER 3

FRACTURE MECHANICS BACKGROUND AND NUMERICAL MODELING OF DELAMINATION

Delamination is a crack that forms between the adjacent plies of a composite laminate at the brittle polymer resin. Therefore, fracture mechanics is a natural choice for delamination investigation in composite materials and a brief introduction of linear elastic fracture mechanics (LEFM) is presented. After the introduction of LEFM, some widely used numerical methods for delamination modeling are presented in the following chapters.

3.1 Fracture Mechanics Background and Linear Elastic Fracture Mechanics-LEFM

Inglis [60] stated that stress at the boundary of a hole is greater than the applied stress on the structure. Stress at the boundary of a hole in an infinite plate with linear elastic isotropic material properties, subjected to axial tensile stress, can be calculated as:

$$\sigma_A = \sigma\left(1+\frac{2a}{b}\right) \qquad (3.1)$$

where, "σ" is the far field stress, "a" is the major axis and "b" is the minor axis of the ellipse as shown in Figure 3.1. From the above formula, it can be observed that when a=b, the hole is circular and the stress at point A is 3 times the remote stress. As b approaches zero, ellipse becomes a sharp crack and stress tends to infinity at the crack tip A, for all stress values. But, it is not possible that the stress to be infinite in nature and the issue of infinite stress is handled by fracture mechanics.

Cracks are present in all materials and act as stress raisers in the material. They amplify the remotely applied stress and as a consequence, lower the strength of the material from the predicted theoretical value. LEFM is used to predict the material resistance to fracture (fracture toughness) for linear elastic materials.

In LEFM, two approaches are used: The Stress Intensity Approach and The Energy Release Rate Approach.

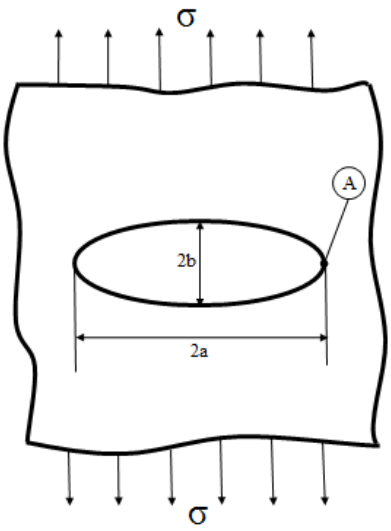

Figure 3.1- Elliptical crack in an infinite plate [32]

Stress Intensity approach:

In fracture mechanics there are three modes of fracture, Mode I, Mode II and Mode III, for three different loading types as shown in Figure 3.2. Mode I quantifies the crack face opening displacement which is normal to crack plane; Mode II quantifies the in-plane shear (sliding shear) which is parallel to the crack plane and normal to the crack front; Mode III quantifies the out of plane shear (tearing shear) which is parallel to the crack plane and parallel to the crack front.

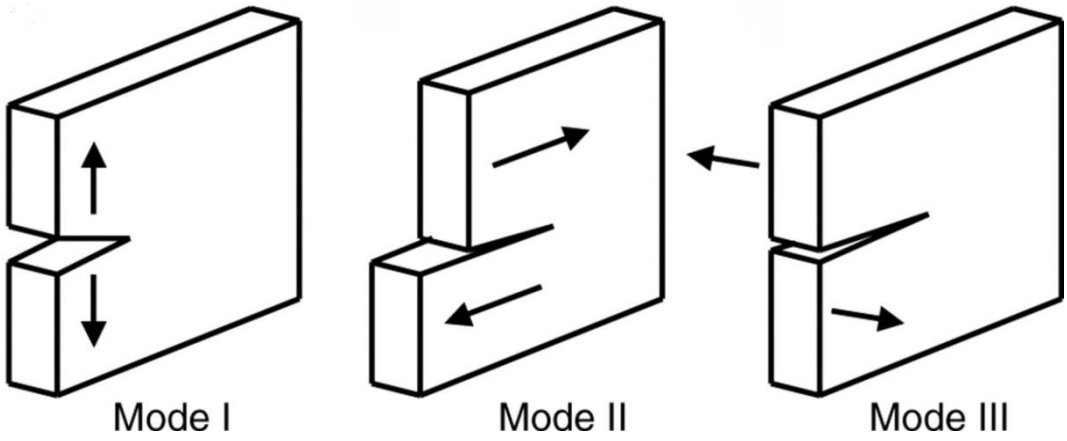

Figure 3.2- Fracture Modes

Stress state at a point around the crack tip in a linear elastic isotropic material is shown in Figure 3.3 and analytical solutions of the stress fields are provided in Table 3.1 for Mode I, II and III loading conditions; where, "σ" is the stress, "r" is the distance from crack tip and "θ" is the angle with the horizontal axis, "x". As seen from the equations in Table 3.1, stress fields around the crack tip can be characterized by the factors K_I, K_{II} and K_{III} where I, II and III stand for the three modes of fracture. These factors are known as the stress intensity factors and measures of the magnitude of the stresses around the crack tip. K_I is the Mode I intensity factor and can be calculated as:

$$K_I=F\sigma\sqrt{\pi a} \qquad (3.2)$$

where, "σ" is the far field stress and "a" is the crack length. F is a factor which signifies the dependence of the stress intensity factor on the specimen and crack geometry, i.e. F = 1 for infinite plate with a center crack.

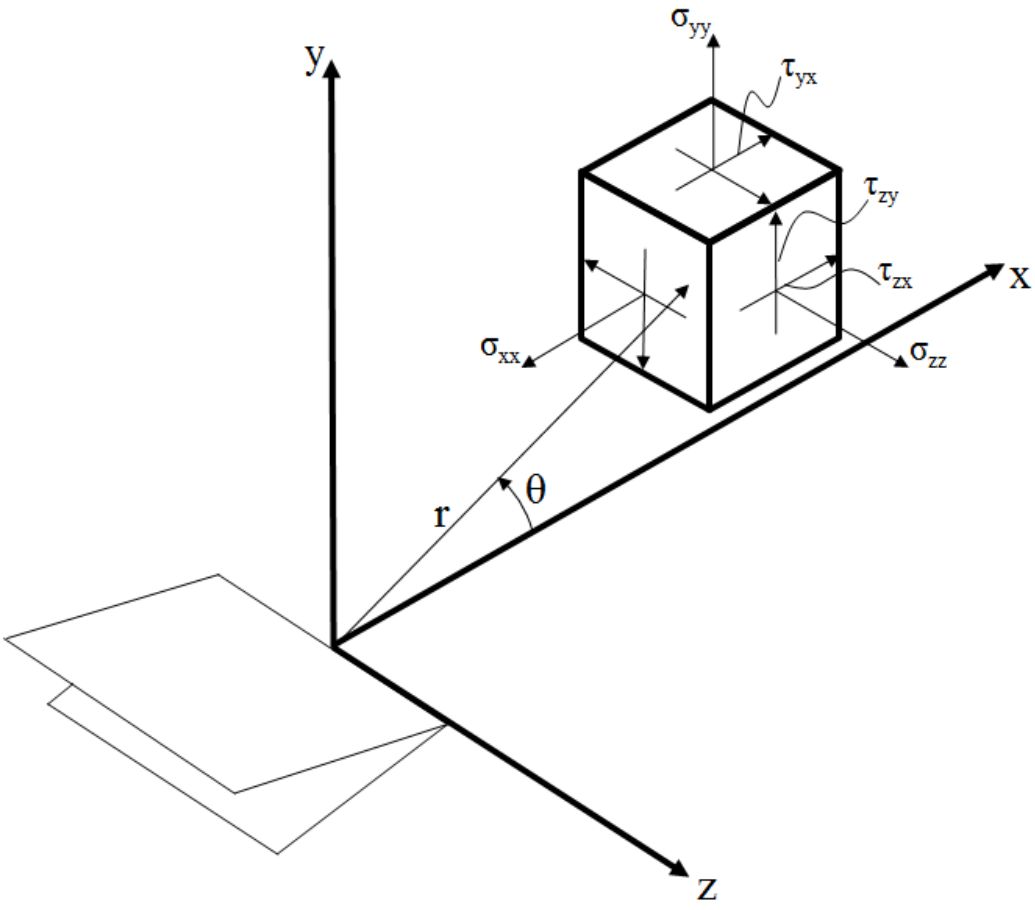

Figure 3.3- Crack tip stress field

Table 3.1- Mode I, II and III stress components around the crack tip [27, 32]

	Mode I	Mode II	Mode III
σ_{xx}	$\frac{K_I}{\sqrt{2\pi r}}\cos\left(\frac{\theta}{2}\right)\left[1-\sin\left(\frac{\theta}{2}\right)\sin\left(\frac{3\theta}{2}\right)\right]$	$-\frac{K_{II}}{\sqrt{2\pi r}}\sin\left(\frac{\theta}{2}\right)\left[2+\cos\left(\frac{\theta}{2}\right)\cos\left(\frac{3\theta}{2}\right)\right]$	0
σ_{yy}	$\frac{K_I}{\sqrt{2\pi r}}\cos\left(\frac{\theta}{2}\right)\left[1+\sin\left(\frac{\theta}{2}\right)\sin\left(\frac{3\theta}{2}\right)\right]$	$\frac{K_{II}}{\sqrt{2\pi r}}\sin\left(\frac{\theta}{2}\right)\cos\left(\frac{\theta}{2}\right)\cos\left(\frac{3\theta}{2}\right)$	0
σ_{zz}	0 for plane stress $\nu(\sigma_{xx}+\sigma_{yy})$ for plane strain	0 for plane stress $\nu(\sigma_{xx}+\sigma_{yy})$ for plane strain	0
τ_{xy}	$\frac{K_I}{\sqrt{2\pi r}}\cos\left(\frac{\theta}{2}\right)\sin\left(\frac{\theta}{2}\right)\cos\left(\frac{3\theta}{2}\right)$	$\frac{K_{II}}{\sqrt{2\pi r}}\cos\left(\frac{\theta}{2}\right)\left[1-\sin\left(\frac{\theta}{2}\right)\sin\left(\frac{3\theta}{2}\right)\right]$	0
τ_{xz}	0	0	$-\frac{K_{III}}{\sqrt{2\pi r}}\sin\left(\frac{\theta}{2}\right)$
τ_{yz}	0	0	$\frac{K_{III}}{\sqrt{2\pi r}}\cos\left(\frac{\theta}{2}\right)$

There are some assumptions that LEFM can be applicable to a problem. First, crack length has to be small compared to dimensions of the considered geometry thus stress field is not affected by boundary conditions. Second, material should be reasonably brittle that the yielded zone around the crack tip has to be small compared to the crack length and the specimen dimensions; this assumption is known as Small Scale Yielding (SSY) assumption. Then, there is a stress field around the crack tip which is characterized by stress intensity factors, K_I, K_{II} and K_{III}, as shown in Figure 3.4.

Crack growth is assumed to happen when stress intensity factor, K_I (K_{II}, K_{III}), reaches the critical stress intensity factor, K_{IC} (K_{IIC}, K_{IIIC}). K_{IC} is a material property that shows the material resistance to cracking and dependent on temperature, environment, microstructure, geometry, strain rate, etc. K_{IC} value increases with the increase in plastic region at the crack tip. In plane stress state, plastic region is larger than the plane strain case and K_{IC} is higher. Therefore, K_{IC} value is measured in plane strain state to be conservative and known as plane strain fracture toughness. In the case of large plastic zones, Elastic-Plastic Fracture Mechanics (EPFM) and related concepts should be used to evaluate the crack resistance; J-integral and CTOD are the two methods of the EPFM.

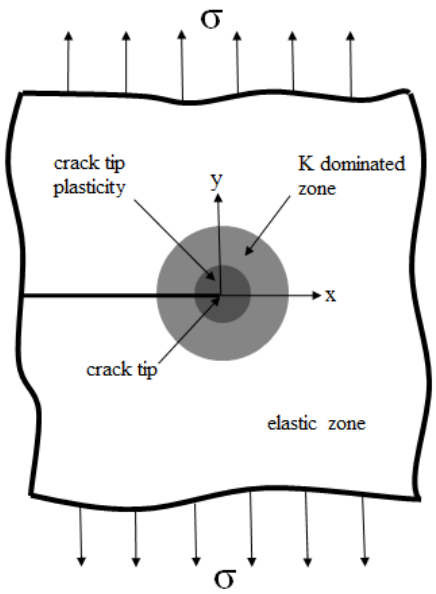

Figure 3.4- Crack tip zones

Strain Energy Release Rate approach:

Griffith [33] stated that energy required to create a crack surface has to be equal to the released strain energy during crack growth. This assumption can be formulated for a perfectly brittle material as:

$$\sigma = \left(\frac{2E\gamma_s}{\pi a}\right)^{1/2} \tag{3.3}$$

where "σ" is the remote stress, "a" is the crack length, "E" is the young modulus, "γ_s" is the surface energy.

Griffith's model is for the brittle materials that show no plastic deformation and strain energy released is consumed to create new crack surfaces. Irwin [34, 46] modified the Griffith's model to take the plasticity into account which is present in the fracture of metallic materials. By assuming the energy associated with the plastic deformation is much higher than the surface energy, fracture stress can be calculated as [46]:

$$\sigma = \left[\frac{2E(\gamma_s+\gamma_p)}{\pi a}\right]^{1/2} \approx \left[\frac{E\gamma_p}{a}\right]^{1/2} \tag{3.4}$$

where, "γ_p" is the plastic work to extend the crack. γ_p is a hard to measure quantity, therefore Irwin [34] proposed the energy release rate concept, G. For a linear

elastic infinite plate under axial tensile load with a center crack, G can be calculated as [27, 32, 46]:

$$G = \frac{\sigma^2 \pi a}{E} \tag{3.5}$$

As in the stress intensity approach, there are three strain energy release rates, G_I, G_{II}, G_{III}, associated with each fracture mode. Crack growth is assumed to happen when energy release rate values reach their critical values G_{IC}, G_{IIC} or G_{IIIC} which are defined as the fracture toughness of the material.

For linear elastic materials, by combining Equations (3.2) and (3.5), strain energy release rate and stress intensity factor for Mode I can be related as [27]:

$$G_I = \frac{K_I^2}{E'} \tag{3.6}$$

where, E'=E for plane stress, $E'=E/(1-\nu^2)$ for plane strain.

Mixed-Mode Loading

In case, there is only one type of load acting on the structure, individual mode stress intensity factors (K_I, K_{II}, K_{III}) or energy release rates (G_I, G_{II}, G_{III}) can be used for fracture predictions. Individual mode stress intensity factors of each load can be added:

$$K_I^{(total)} = K_I^{(1)} + K_I^{(2)} + \dots K_I^{(n)} \tag{3.7}$$

In the case of a mixed-mode loading, strain energy release rate components for Mode I, II and III fracture modes can be added to find the total energy released [27]:

$$G_T = G_I + G_{II} + G_{III} = \frac{K_I^2}{E'} + \frac{K_{II}^2}{E'} + (1+\nu)\frac{K_{III}^2}{E} \tag{3.8}$$

For linear elastic isotropic materials, fracture direction can be found by various methods [45]: Maximum Tangential Stress Criterion, Maximum Energy Release Rate Criterion or Minimum Strain Energy Density Criterion. In composite

materials, delamination is restricted to grow between the adjacent plies which dictates a mixed-mode delamination behavior.

3.2 Numerical Modeling of Delamination

In fracture mechanics, there are closed form solutions for stress intensity or energy release rate calculations for simple problems: infinite plate with center crack, semi-infinite plate with edge crack, penny shaped crack in an infinite solid etc. But, it is hard to calculate stress intensity factors or energy release rates analytically for complex structures especially for composite ones. Thus, numerical methods are necessary for crack simulations in composite materials.

Numerical simulations is crucial in today's world in every step of the life of a product including the initial design phase, stress analysis, fatigue and damage tolerance analysis, manufacturing, testing, maintenance etc. for cost effective product development. Finite Element Method (FEM), Finite Difference Method (FDM), Boundary Element Method (BEM) are commonly used numerical methods in engineering [38]. Because FEM is the generally used and available tool for solid mechanics, FE methods are introduced below that are used in crack modeling.

3.2.1 Continuum Approach

In this approach, delamination initiation is predicted with the strength based approaches. Stress components are compared with the allowable strength values of the material. Some interaction equations are used between the tensile/shear stress and strength components in in-plane and through thickness directions [1, 6, 12]. Orifici et al. [1] predicted the delamination initiation location in a composite T-joint by using Tsai Criterion which is given as:

$$\left(\frac{\sigma_1}{X_t}\right)^2+\left(\frac{\sigma_3}{Z_t}\right)^2+\left(\frac{\tau_{23}}{S_{23}}\right)^2\geq 1 \qquad (3.9)$$

where, "σ_1" is the longitudinal stress, "σ_3" is the interlaminar through thickness stress, "τ_{23}" is the interlaminar shear stress, "X_t" is the longitudinal tensile strength, "Z_t" is the interlaminar tensile strength, "S_{23}" is the interlaminar shear strength.

The red regions in Figure 3.5 show the failed locations on the considered structure according to the above criterion.

Orifici et al. provides a comprehensive review of strength based delamination initiation criterions in reference [43].

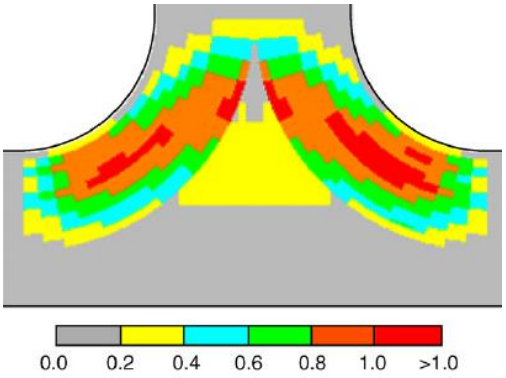

Figure 3.5- Delamination initiation failure index

3.2.2 Fracture Mechanics Based Approaches

3.2.2.1 Virtual Crack Closure Technique (VCCT)

The VCCT approach is based on the assumptions that the energy released in crack growth is equal to the work required to close the crack to its original length [27, 44].

In VCCT, a pre-crack is inserted manually in the structure as shown in the Figure 3.6. The strain energy release rates, G_I, G_{II}, G_{III}, are then calculated at the crack front by using nodal force and displacement values. For a 2D model shown in the Figure 3.6, energy release rates can be calculated as [27]:

$$G_I = \frac{1}{2\Delta a} F_{yi}(v_k - v_j) \tag{3.10}$$

$$G_{II} = \frac{1}{2\Delta a} F_{xi}(u_k - u_j) \tag{3.11}$$

where, "$2\Delta a$" is crack surface per unit length, "F_{xi}" and "F_{yi}" are the nodal forces in "x" and "y" directions for node "i", "u_k", "u_j", "v_k" and "v_j" are nodal displacements in x and y directions for nodes "k" and "j".

For valid predictions with VCCT, crack growth should not significantly alter the state at the crack tip (self-similarity state), therefore one can use force and displacement values in sequential steps.

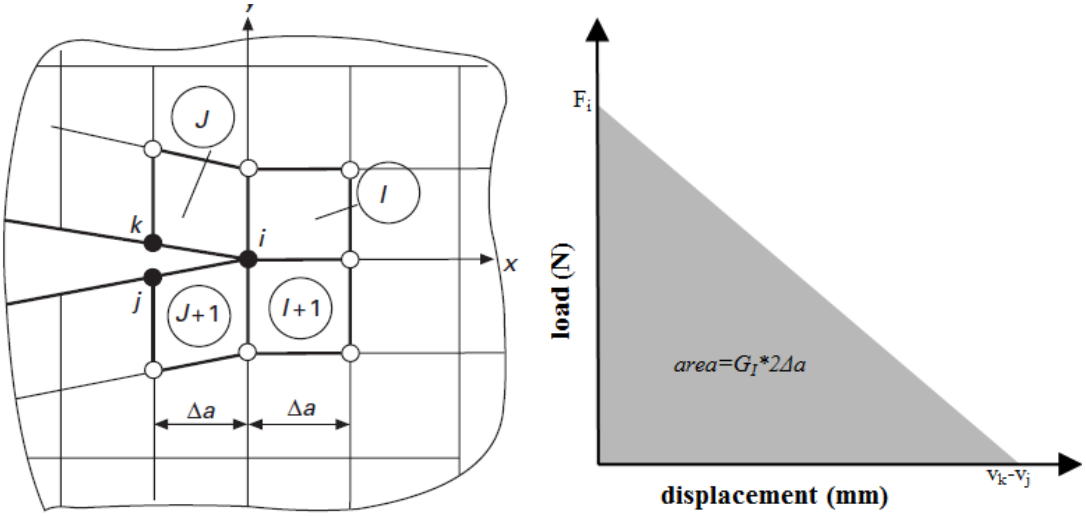

Figure 3.6- VCCT for 2D quadrilateral elements [27]

Primary advantage of VCCT is; each strain energy release rate component can be calculated at each node of the crack front which allows a detailed investigation. But the requirement of pre-crack makes the modeling difficult especially in complex structures and initial crack location has to be known beforehand. For reliable predictions, VCCT requires also a fine mesh in crack front [44].

Comprehensive information about VCCT is given by Krueger in reference [44]: equations in 2D and 3D, use of linear/quadratic elements, geometric nonlinear analysis, bi-material interfaces, sharp crack fronts, element length variations and mesh size.

3.2.2.2 Virtual Crack Extension (VCE)

In VCE, crack tip is advanced virtually by modifying the nodes at the crack front for a prescribed crack growth length as shown in Figure 3.7. Only elements at the crack tips are modified during the crack extension and an additional stiffness matrix calculation is made for the modified elements [44]. Strain energy release rate is then computed based on the potential energy difference of the structure for

the two crack lengths [24, 45]. Hellen [69] stated that care must be taken when selecting the prescribed crack length growth because of the adverse effects of the high virtual crack lengths.

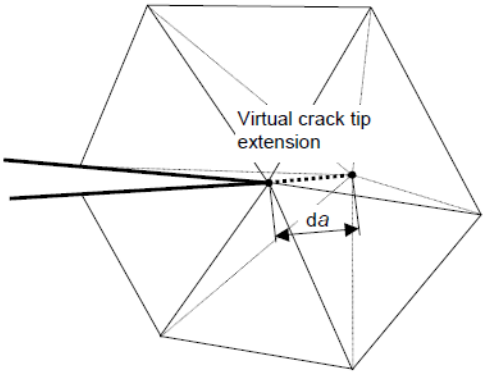

Figure 3.7- Crack tip modification in VCE [45]

3.2.2.3 J-integral

Potential energy of a system can be represented as the sum of elastic energy stored in the body and the energy from the applied load (work done). The potential energy of the system per unit thickness can be given as:

$$\Pi = \int_A w dA - \int_\Gamma T_i u_i d\Gamma \tag{3.12}$$

$$w = \int_0^{\varepsilon_{ij}} \sigma_{ij} d\varepsilon_{ij} \tag{3.13}$$

$$T_i = \sigma_{ij} n_j \tag{3.14}$$

where, "Π" is the potential energy, "w" is the strain energy density, "T" is the traction vector, "u" is the displacement, "Γ" is the integral path taken along an arbitrary contour, "A" is the area enclosed by Γ [32, 62] as shown in Figure 3.8.

By taking the derivative of the potential energy with respect to crack length and using divergence theorem, energy released during crack growth can be calculated as:

$$J = -\frac{\partial \Pi}{\partial a} \tag{3.15}$$

$$J = \int_\Gamma \left(w n_1 + T_i \frac{\partial u_i}{\partial x}\right) ds \tag{3.16}$$

Equation (3.15) represents the rate of change in potential energy with respect to crack advance as the strain energy release rate. J integral is a path independent line integral provided that the integral path starts and ends on the crack surfaces and crack surfaces are traction free and straight. Although, J-integral was developed for non-linear elastic material energy release rate calculations by Rice [40], it is also applicable for linear elastic materials. J = G for linear elastic materials.

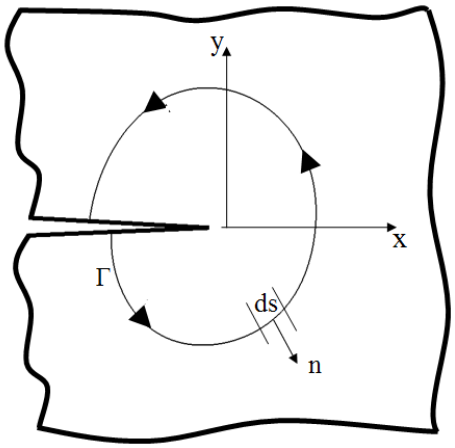

Figure 3.8- J-integral contour [62]

3.2.2.4 Other Methods

Stress and Displacement Correlation

The analytical stress (Section 3.1) or displacement fields can be correlated with the FE stress or displacement fields to find the stress intensity factors [45].

CTOD

For ductile materials, as load is applied on the structure, crack tip is blunted before crack advances. The displacement behind the crack tip (Figure 3.9), crack tip opening displacement, CTOD, can be used to investigate fracture in the materials. Fracture is assumed to happen when CTOD reaches a critical value. Although CTOD mainly used for nonlinear materials, this method can also be used for the stress intensity factor calculations in linear elastic materials. By considering the strip yield model [47], CTOD can be calculated as [26, 32, 62]:

$$\delta = \frac{K_I^2}{E\sigma_y} \qquad (3.17)$$

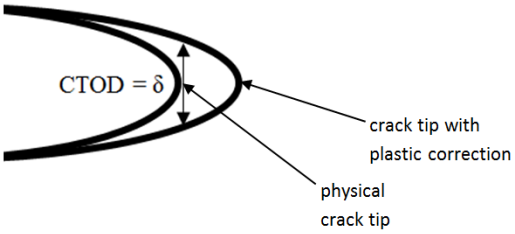

Figure 3.9- CTOD definition

Crak tip elements

Conventional finite elements near the crack tip even with small sizes would not result in correct stress and displacement fields, because of the singularity at the crack tip. Use of special crack tip elements improves the results and solution time with a coarser mesh [32, 64]. Figure 3.10 shows a modification of a 2D quadrilateral quadratic element to a triangular crack tip element. In these elements, nodes at one side collapsed on to the crack tip and mid nodes at the neighboring sides near to the crack tip are moved to quarter point. If the three nodes (1, 4, 8 in Figure 3.10) at the crack tip are constrained to move together, element shows the $1/r^{1/2}$ crack tip singularity which is present in elastic materials. If the nodes are moved independently, element shows the r^{-1} singularity which is present in the crack tip plasticity [32, 64].

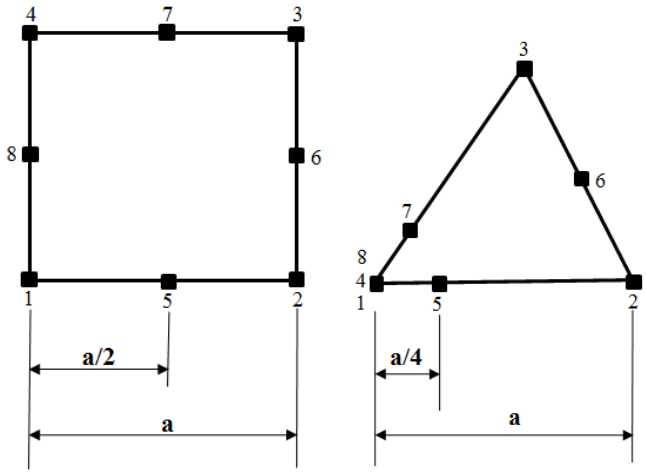

Figure 3.10- Conventional quadrilateral element collapsed into a triangular element

3.2.3 Extended Finite Element Method (XFEM)

Numerical simulation of a structure with discontinuities (crack, delamination) has some extra requirements with respect to plain structures: fine mesh at the crack front, use of special elements, structured mesh, defining crack path, adaptive meshing, etc. XFEM can be used to overcome these difficulties for crack modeling. In their review, Belytschko et al. [68] states that XFEM utilizes the partition of unity concept and enrichment functions for modeling discontinuities in the structure. In XFEM, a predefined path is not required and crack can move in any arbitrary direction in 3D complex geometries. Crack can move through the elements eliminating fine mesh requirement and adaptive meshing as seen in Figure 3.11.

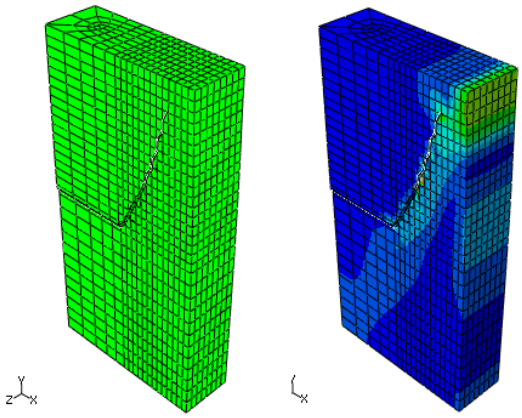

Figure 3.11- Crack growth simulation with Abaqus XFEM [22]

3.2.4 Damage Mechanics Approach - Cohesive Zone Method (CZM)

Laminated composite materials are composed of plies which are connected to each other with almost zero thickness matrix or adhesive materials. Delamination/debond initiates and propagates between these ply interfaces. In CZM, a zero thickness cohesive layer is modeled between the ply interfaces to simulate delamination/debond. The origin of the cohesive model goes back to Dugdale [47], Barenblatt [48] and Hillerborg et al. [49] who assumed that cracks grow in a thin strip of a plastic zone.

In CZM, there is no need to place a crack manually in the numerical model. Cracks can initiate anywhere in the structure which allows multiple crack

initiations and propagations. This is especially important for complex structures that the residual strength of the structure should be evaluated. Because of these advantageous characteristics, CZM is being increasingly used in delamination/debond modeling in laminated composites.

In CZM, cohesive elements are placed between the composite plies as seen in Figure 3.12. A cohesive element can be considered as 2 separate faces. Initially, these faces are in contact and the element is at the zero stress state. As the load is applied, element faces separate from each other in Mode I and Mode II directions for a 2D case. Cohesive layer is then assumed to be damaged according to a considered cohesive law which relates interface tractions to interface displacements. Some of the generally used cohesive laws are bilinear [19, 20, 25, 54], exponential [50] and trapezoidal [51, 52] laws which are shown in Figure 3.13,

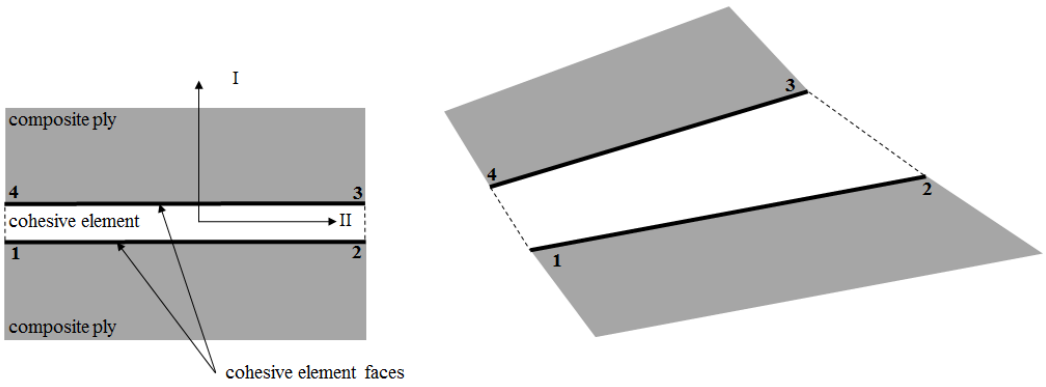

Figure 3.12- A 2D cohesive element undeformed and deformed state

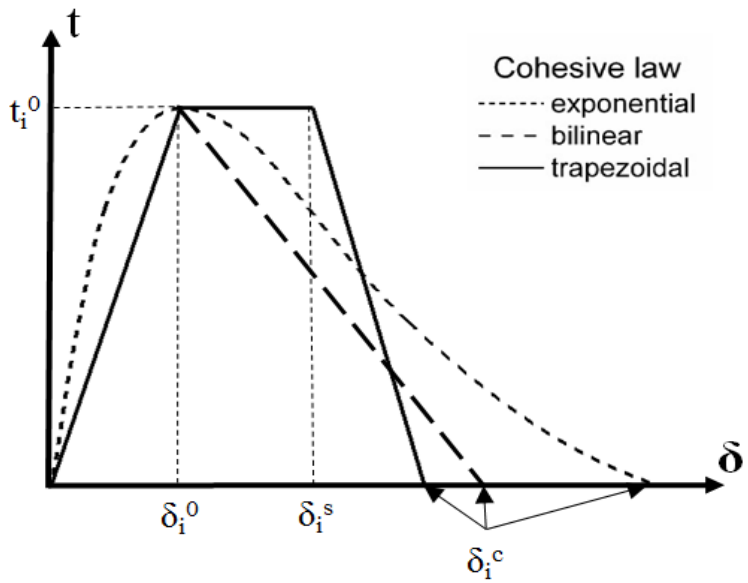

Figure 3.13- Exponential, bilinear and trapezoidal cohesive laws

where, "t_i^0" is the interfacial strength and "δ_i^0" is interfacial displacement for damage initiation, "δ_i^C" is the critical displacement for fracture and "δ_i^S" is the softening displacement for trapezoidal law; i=I, II, III stands for Mode I, II and III. Bilinear cohesive law is used in this study and CZM is investigated further within the scope of this cohesive law.

Single Mode Delamination

Figure 3.14 gives a general scheme of the delamination process for bilinear cohesive law for individual fracture modes. The numbers on the loaded specimens are also located on the traction-displacement curves for ease of interpretation. Damage of the cohesive elements is assumed to start after damage initiation displacement δ_i^0 (i= I, II and III) or damage initiation tractions t_i^0 (pt2). Up to damage initiation point, material behavior is assumed to be linear. In this linear region (pt0-pt1-pt2), the ratio of the traction to displacement gives the stiffness of the interface:

$$k_i^0 = \frac{t_i^0}{\delta_i^0} \tag{3.18}$$

This stiffness is called the penalty stiffness. In numerical applications, the penalty stiffness is chosen to be high enough to maintain the correct load transfer between the layers and prevent the interpenetration of the crack surfaces and low enough to get rid of numerical instabilities. Although, stiffness values around 1e6 N/mm^3 are generally used in the literature [19, 20, 25, 56], Turon et al. [56] proposed an equation to calculate Mode I penalty stiffness:

$$k_I^0 = \alpha \frac{E_3}{t} \tag{3.19}$$

where, "α" is the parameter much larger than 1 (chosen as 50 in [20, 56]), "E_3" is the young modulus of the laminate in the direction normal to crack plane, "t" is the adjacent laminate thickness. The stiffness values in other directions are generally taken as equal to k_I^0.

After damage initiation, a scalar damage parameter, "d", is used to track the damage evolution in the loading history. d is evolved from 0 at the initiation point

(pt2) to 1 at the final point at which the crack is assumed to grow (pt4). The traction on the cohesive element decreases through the damage propagation according to d. After pt4, cohesive element does not carry further load (pt5). This constitutive behavior can be defined as [19, 22]:

$$\left.\begin{array}{ll} k_i^0 \delta_i & \delta_i \le \delta_i^0 \\ (1-d) k_i^0 \delta_i & \delta_i^0 < \delta_i < \delta_i^c \\ 0 & \delta_i \ge \delta_i^c \end{array}\right\} = t_i \qquad (3.20)$$

$$d = \frac{\delta_i^c (\delta_i - \delta_i^0)}{\delta_i (\delta_i^c - \delta_i^0)} \qquad (3.21)$$

where, "δ_i" is the displacement at an arbitrary point.

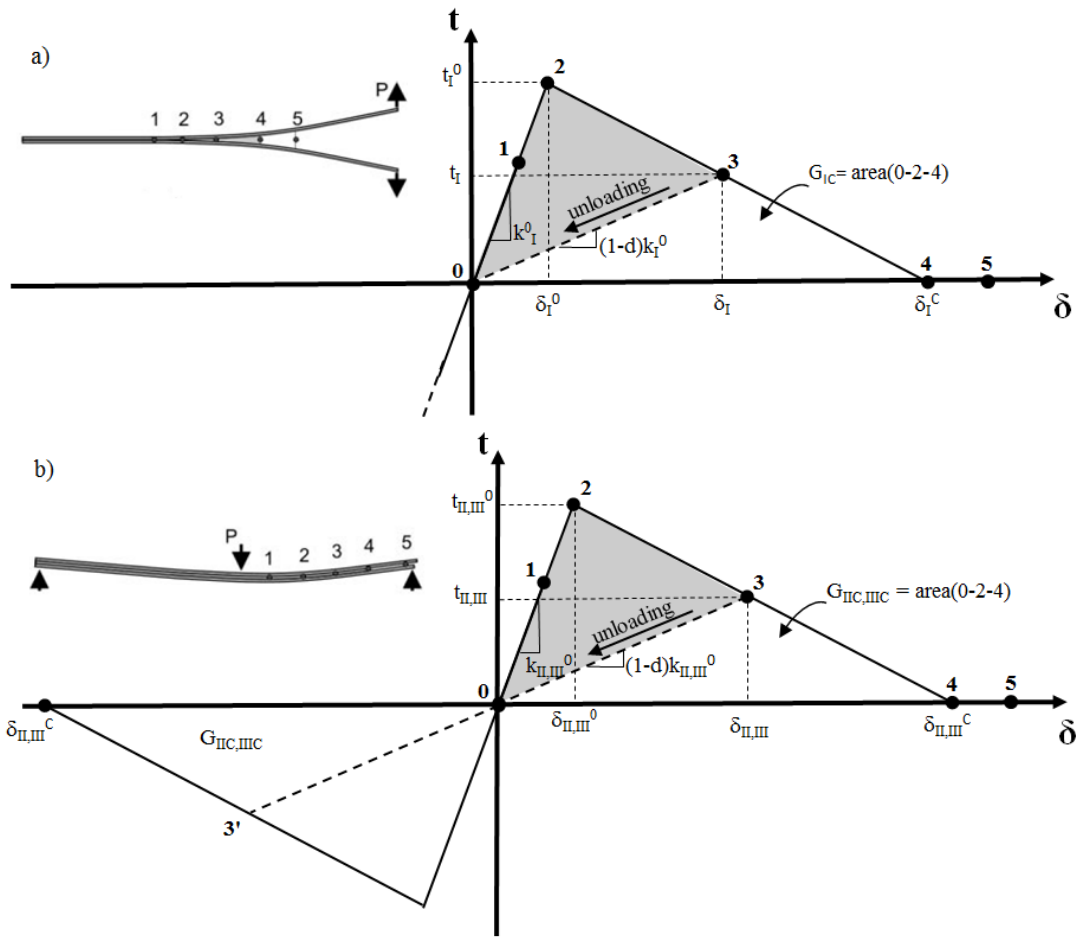

Figure 3.14- Bilinear cohesive law (a) Mode I, (b) Mode II or Mode III [57]

In the loading history, if unloading takes place from any point, pt1, between pt0 and pt2, curve follows the path with stiffness k_i^0. If unloading takes place from any point, pt3, between pt2 and pt4, curve follows the path from pt3 to pt0 with the reduced stiffness. By further compressive load, laminates will be intact after pt0. From this point on, the Mode I penalty stiffness is assumed to be equal to the initial k_I^0 to prevent the penetration. But, for Modes II and III, damage of the elements is taken into account with the same unloading stiffness.

The area under traction-displacement curve (pt0- pt2 – pt4) is equal to fracture toughness, G_{ic}, of the material and can be calculated as:

$$G_{ic}=\frac{t_i^0\delta_i^c}{2}=\frac{k_i^0\delta_i^0\delta_i^c}{2} \tag{3.22}$$

Therefore, other than the t_i^0 and δ_i^0, G_{ic} or δ_i^c has to be specified to define the traction- displacement curve.

Mixed-Mode Delamination

Delamination in composite materials is generally in a combination of Mode I, Mode II and Mode III. Therefore, explanation of CZM in mixed-mode is necessary.

In single mode delamination, initiation is satisfied with allowable tractions (t_i^0) or displacements (δ_i^0) of the interface. But for the mixed-mode, delaminations can take place before any single mode allowable. Therefore, interactions of tractions or displacements are used in mixed-mode conditions for delamination initiation. A generally used initiation criterion is the power law interaction of single mode tractions as shown below:

$$\left(\frac{\langle t_I\rangle}{t_I^0}\right)^{\alpha}+\left(\frac{t_{II}}{t_{II}^0}\right)^{\alpha}+\left(\frac{t_{III}}{t_{III}^0}\right)^{\alpha}\geq 1 \tag{3.23}$$

where, "t_i" is the stress at an arbitrary point, "< >" is the Macaulay's bracket that equates the negative values to zero, "α" is the power coefficient; α = 2 is used in this study. If the left part of the equation is bigger than 1, damage in the cohesive element is assumed to start. Different criteria for the initiation are provided in Orifici et al. [43].

Displacement at any arbitrary point for the mixed-mode can be calculated as [19, 22]:

$$\delta_m=\sqrt{\langle\delta_I\rangle^2+\delta_{II}{}^2+\delta_{III}{}^2}=\sqrt{\langle\delta_I\rangle^2+\delta_{shear}{}^2} \tag{3.24}$$

where,

$$\delta_{shear}=\sqrt{\delta_{II}{}^2+\delta_{III}{}^2} \tag{3.25}$$

In case, power law interaction is used, damage initiation displacement for the mixed-mode can be calculated as [19]:

$$\left.\begin{array}{ll}\delta_I{}^0\delta_{II}{}^0\sqrt{\frac{1+\beta^2}{(\delta_{II}{}^0)^2+(\beta\delta_I{}^0)^2}} & \delta_I>0\\ \delta_{shear}{}^0 & \delta_I<0\end{array}\right\}=\delta_m{}^0 \tag{3.26}$$

by defining the displacement mixed-mode ratio, β, as [19]:

$$\beta=\frac{\delta_{shear}}{\delta_I} \tag{3.27}$$

Similar to single mode damage parameter, mixed-mode damage parameter can be calculated as [19, 22]:

$$d=\frac{\delta_m^c(\delta_m-\delta_m^0)}{\delta_m(\delta_m^c-\delta_m^0)} \tag{3.28}$$

where, "$\delta_m{}^c$" is the crack propagation displacement for mixed-mode, "δ_m" is the crack propagation displacement for mixed-mode at any arbitrary point. $\delta_m{}^c$ is calculated based on the chosen delamination propagation criterion. Orifici et al. [43] gives a number of evolution criteria. Between them Benzeggagh-Kenane Law [19, 22, 57, 59] is one of the most used propagation laws and is given as:

$$G_C \geq G_{IC} + (G_{IIC} - G_{IC})\left(\frac{G_{shear}}{G_T}\right)^{\eta} \tag{3.29}$$

G_{shear} and G_T are given as:

$$G_{shear} = G_{II}+ G_{III} \tag{3.30}$$

$$G_T = G_I + G_{II} + G_{III} \tag{3.31}$$

where, "G_c" is the fracture toughness for a specified mixed-mode ratio, "η" is the BK law exponent extracted from experimental results by curve fitting. By using BK law, critical displacement for mixed-mode can be calculated as [19, 57]:

$$\left.\begin{array}{ll} \frac{2}{k_i^0 \delta_m^0}\left[G_{IC} + (G_{IIC} - G_{IC})\left(\frac{\beta^2}{1+\beta^2}\right)^{\eta}\right] & \delta_I > 0 \\ \sqrt{(\delta_{II}{}^c)^2 + (\delta_{III}{}^c)^2} & \delta_I < 0 \end{array}\right\} = \delta_m^C \tag{3.32}$$

A graphical representation of the mixed-mode CZM can be seen in Figure 3.15. Triangles on the vertical planes show normal and shear mode behaviors. Any triangle between these two planes shows a mixed-mode behavior for a specified mode ratio.

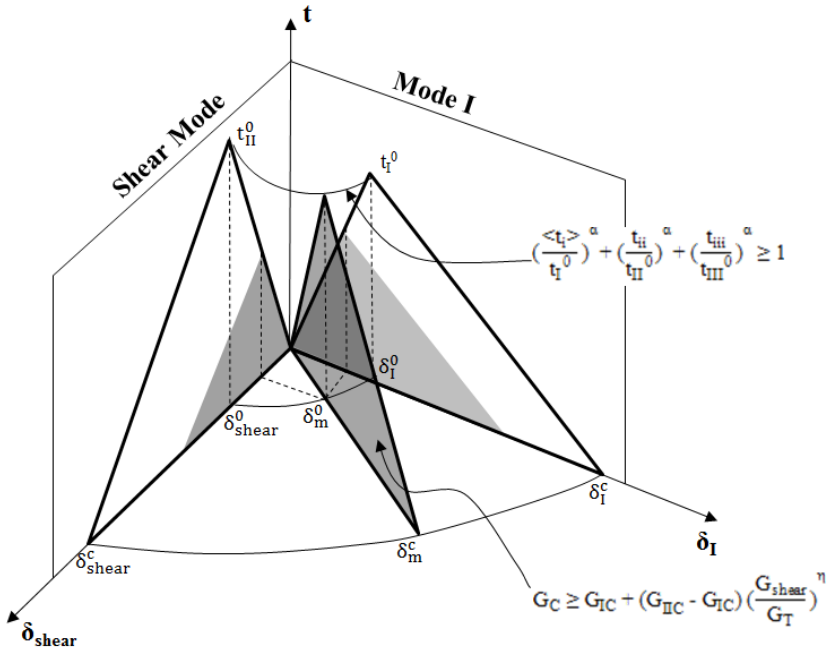

Figure 3.15- Mixed-mode bilinear cohesive law [22]

Nonlinear Solution Procedure

In CZM, because of material softening, a nonlinear behavior is present in the load-displacement curve with oscillatory behavior of snap-throughs and snap-

backs. Figure 3.16 shows nonlinear load-displacement examples of a structure with snap throughs, snap backs, bifurcations or combinations of these [63].

In general, classical implicit Newton-Raphson (NR) method is used in FE studies. For turning points on the load-displacement response, stiffness matrix becomes singular and classical NR performs poorly as seen in Figure 3.17 (a). Therefore, advanced numerical solution schemes are required. Arc length method is the generally used solution scheme for CZM applications. In arc length methods, the step size of the load and displacement are controlled and iterations are done for a prescribed arc length as shown in Figure 3.17 (b).

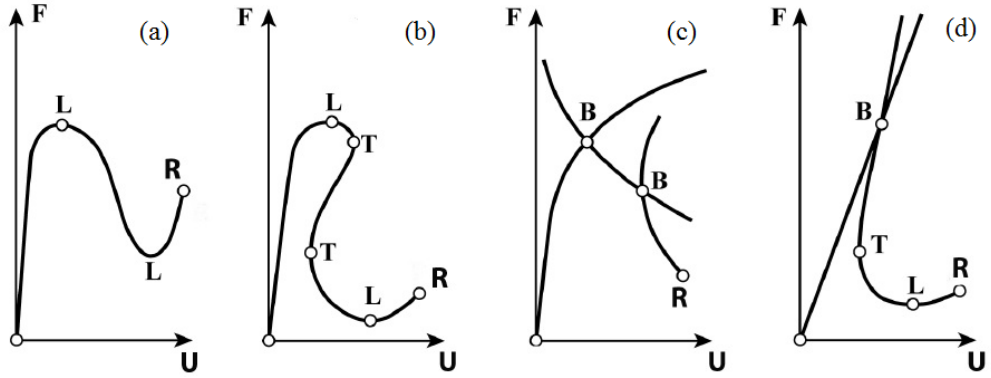

Figure 3.16- Nonlinear load-displacement response (a) snap-through (b) snap-back (c) bifurcation (d) bifurcation combined with limit points and snap-back [63]

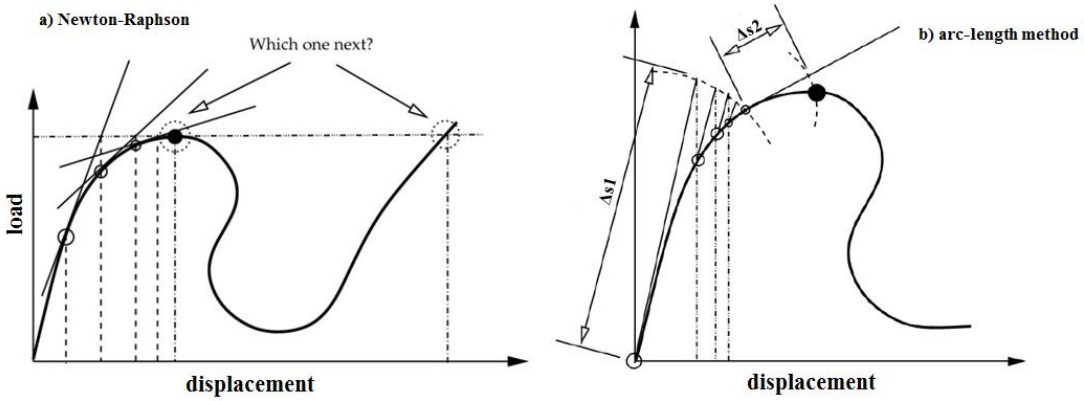

Figure 3.17- Newton-Raphson vs Arc Length Method [63]

CHAPTER 4

DCB, ENF AND MMB INVESTIGATIONS

Laminated composite fracture toughness values are evaluated with the delamination tests for the individual or combination of Mode I, II and III. In this chapter, widely used delamination tests, Double Cantilever Beam (DCB), End Notched Flexure (ENF) and Mixed Mode Bending (MMB) tests are studied for delamination initiation and propagation simulation for Mode I, Mode II and Mixed-Mode I and II, respectively, with 2D FE models. Abaqus CZM is validated by comparing the numerical results of the tests with the analytical solutions and with the additional data from Albiol [21] which involve experimental and numerical results. Additionally, element type, element size, viscosity ratio, interlaminar stiffness, interlaminar strength and fracture toughness values are further investigated to see the sensitivity of the numerical solutions to these parameters.

In numerical simulations, bilinear cohesive law is used with quadratic stress interaction for delamination initiation and BK law for delamination propagation. Nonlinear implicit solutions are carried out with prescribed displacements.

In Section 4.1, specimen geometry and material properties are presented. Detailed studies of DCB, ENF and MMB tests are presented in sections 4.2, 4.3 and 4.4, respectively.

4.1 Specimen Geometry

Test specimen is composed of two uniform thickness sublaminates with 0 degree, UD, AS4/3501-6 composite material plies. A thin non-adhesive patch is inserted between the sublaminates for initial delamination. Specimen geometry is presented in Figure 4.1 and the related values are provided in Table 4.1 [21], where “2L” is the specimen length, “b” is the specimen width, “h” is the thickness of each sublaminate and “a” is the initial delamination length. Specimen fiber direction is

in the x direction and transverse direction is in the y direction of the coordinate system given in the figure. Test specimen is same for each test except from the initial delamination lengths which are provided in Table 4.2 with corresponding fracture toughness values for different mixed-mode ratios. Elastic material properties are provided in Table 4.3 and interface material properties are provided in Table 4.4 for the AS4/3501-6 composite material.

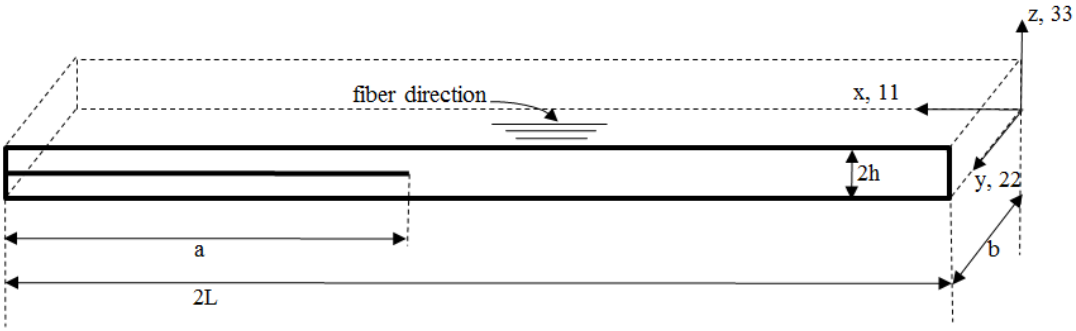

Figure 4.1- Test specimen geometry

Table 4.1- Test specimen dimensions and lay-up [21]

2L[mm]	b[mm]	2h [mm]	layup
102.0	25.4	3.12	24 x (0° UD)

Table 4.2- Initial delamination lengths and fracture toughness values of DCB, ENF and MMB specimens [21]

G_{II}/G_T	0% (DCB)	0.2 (MMB)	100% (ENF)
G_C [N/mm]	0.969	1.03	1.719
a [mm]	32.9	33.7	39.3

Table 4.3- Elastic properties of the AS4/3501-6 material [21]

E_{11} [GPa]	E_{22} [GPa]	E_{33} [GPa]	G_{12} [GPa]	G_{13} [GPa]	G_{23} [GPa]	ν_{12}	ν_{13}	ν_{23}
122.7	10.1	10.1	5.5	5.5	3.7	0.25	0.25	0.45

Table 4.4- Interface properties of the AS4/3501-6 material [21]

k_I^0 [MPa/mm]	k_{II}^0 [MPa/mm]	k_{III}^0 [MPa/mm]	t_I^0 [MPa]	t_{II}^0 [MPa]	t_{III}^0 [MPa]	G_{IC} [N/mm]	G_{IIC} [N/mm]	G_{IIIC} [N/mm]	η
1e6	1e6	1e6	80	100	100	0.969	1.719	1.719	2.284

4.2 DCB Investigation

DCB test is the generally used test for Mode I fracture toughness evaluations and standardized by American Society for Testing of Materials (ASTM-5528) [35]. In DCB test, opening displacements are applied at the end of the delaminated sublaminates of the specimen as seen in Figure 4.2. During the test, load-displacement behavior is recorded and G_{IC} curve is generated with test data reduction schemes.

Analytical solutions are also present to evaluate the load-displacement behavior of the DCB specimen. In this study, load-displacement curve of the DCB specimen is evaluated with the Modified Beam Theory (MBT) [21, 23, 24, 35, 37]. The results are compared with the Abaqus numerical solution and with the additional data from Albiol [21].

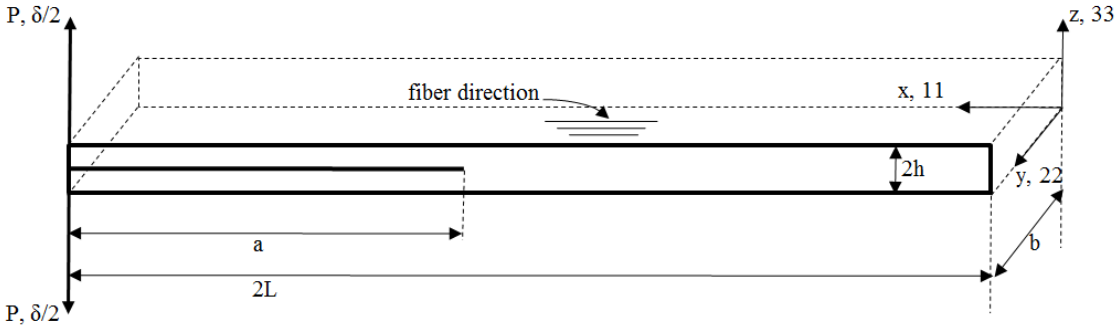

Figure 4.2- DCB test, loading and BCs

4.2.1 Comparison of Analytical and Numerical Results

Analytical solution:

Assuming that a sublaminate of the specimen is a cantilever beam with length "a", deflection at the end of the sublaminate under concentrated load can be calculated with the classical beam theory. The beam theory assumes perfect clamping and neglects rotation and shear deformations at the crack tip [37].

Therefore, to take rotation and deformation at the crack tip into account, crack length "a" is modified by the parameter "χ" in MBT. The deflection of the specimen sublaminates can then be calculated as:

$$\delta=\frac{2P(a+\chi h)^3}{3E_{11}I} \tag{4.1}$$

where, "χ" is the crack length correction parameter, "Γ" is the transverse modulus correction factor [37]:

$$\chi=\sqrt{\frac{E_{11}}{11G_{13}}[3-2\left(\frac{\Gamma}{1+\Gamma}\right)^2]} \tag{4.2}$$

$$\Gamma=1.18\frac{\sqrt{E_{11}E_{22}}}{G_{13}} \tag{4.3}$$

In LEFM, Mode I compliance (C_I) and energy release rate (G_I) can be calculated as:

$$C_I=\frac{\delta}{P}=\frac{2(a+\chi h)^3}{3E_{11}I} \tag{4.4}$$

$$G_I=\frac{P^2}{2b}\frac{dC}{da}=\frac{P^2(a+\chi h)^2}{bE_{11}I} \tag{4.5}$$

$$I=\frac{bh^3}{12} \tag{4.6}$$

where, "I" is the moment of inertia. Classical beam theory solution can be evaluated by setting $\chi=0$.

After initiation of the delamination, carried load by the specimen starts to decrease with the propation. Displacement for the propagation region can be calculated as [21, 24]:

$$\delta=\frac{2(G_{IC}bE_{11}I)^{3/2}}{3E_{11}IP^2} \tag{4.7}$$

Analytical solution of the DCB test is shown in Figure 4.3. The linear part of the curve is evaluated by equation (4.1) and non-linear part by equation (4.7). The intersection of the two curves corresponds to the delamination initiation point.

Numerical Model:

An FE model is created with plane strain assumption for DCB test simulation in Abaqus with the below specifications:

- A cohesive layer is inserted between the two sublaminates with a thickness of 0.001 mm.
- 0.30 mm element size is used both for composite and cohesive sections.
- 3400 CPE4 (2D, 4-node, bilinear, plane strain, quadrilateral) elements for composite section, 230 COH2D4 (2D, 4-node, cohesive) elements for cohesive section are used. A total number of 4092 nodes are present in the model.
- A viscosity parameter with a value of 1e-5 is used to help the convergence.
- 3.5 mm prescribed opening displacements are applied from the lower and upper sublaminate ends in the 3rd direction and same ends are constrained in the 1st direction.

Numerical solution is shown in Figure 4.3. The MBT and the numerical solutions agree quite well as seen from the figure. The slight nonlinearity in the numerical curve until the initiation is caused by the accumulation of the damage in the cohesive elements. After delamination initiation, load starts to decrease with increasing displacement. In the second part of the numerical curve, an oscillatory behavior is observed. This is due to the failing cohesive elements which soften the structure and cause convergence difficulties. The oscillatory behavior in the softening region is also observed in references [20, 54, 56]. Although, a few increments are enough for the linear region, much more increments are required to get the delamination response in the softening region of the numerical curve because of the oscillatory behavior. Experimental and numerical results from [21] are provided in Figure 4.4. The results also agree quite well with numerical solution carried with Abaqus CZM (Figure 4.3). Therefore, it can be considered that Abaqus CZM gives reliable results for delamination simulation of the DCB test.

A 3D FE model is also created in Abaqus to check the validity of the 2D plane strain assumption. There are 47670 elements (42840 linear hexahedral elements of type C3D8I, 4830 linear hexahedral cohesive elements of type COH3D8, corresponding to 0.60 mm element length) and 58824 nodes in the 3D model. Compared with the 2D model (0.60 mm element length and CPE4I element type), results are very close to each other. Stiffness values are almost the same and there is only a 0.48% drop at the maximum load.

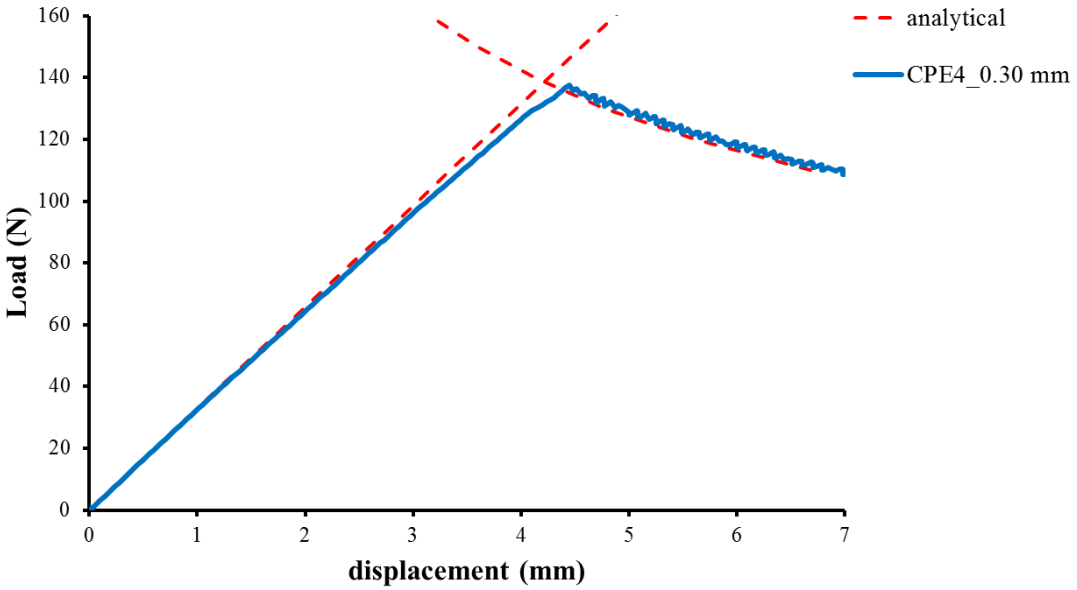

Figure 4.3- Analytical and numerical solutions for the DCB test

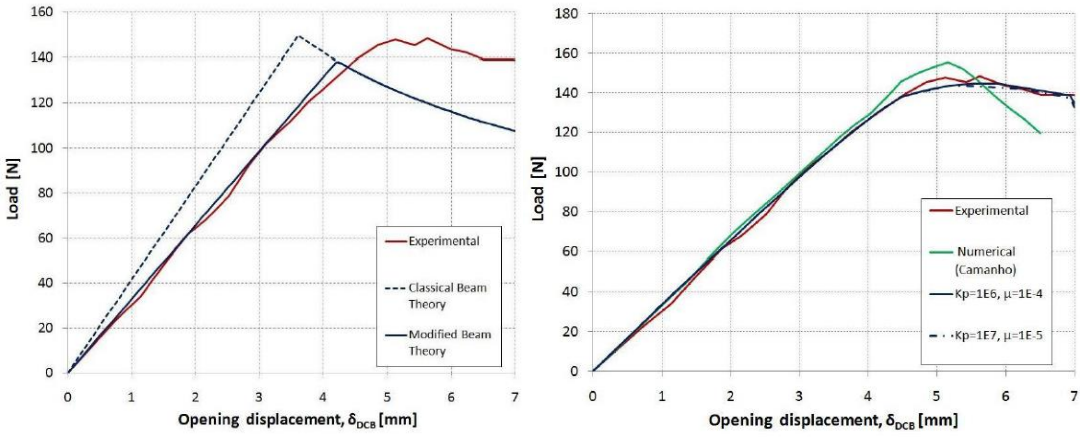

Figure 4.4- DCB analytical, numerical and experimental solutions from the reference [21]

4.2.2 Numerical Sensitivity Study

In this chapter, some FE and cohesive parameters are investigated in a sensitivity study to see their effects on the DCB results.

Effect of the Element Type

In highly bended structures, fully integrated elements, CPE4, suffer from "shear locking" and can give parasitic shear and extra stiffness to the structure [22]. To overcome this problem, reduced integration element, CPE4R, with only one integration point can be used which needs also less computing time. Although, CPE4R elements suffer from "hourglass effect" which may give zero stress at the integration point, one can utilize hourglass stiffness to eliminate such problems. An additional element type, CPE4I (incompatible mode element), make use of enhancing element's deformation gradient to overcome shear locking in CPE4 elements [22]. To see the effect of the element type, CPE4, CPE4R and CPE4I elements are used in FE simulations by keeping the other parameters constant.

Figure 4.5 shows that, results are close to each other for models with CPE4, CPE4R and CPE4I element types and 0.30 mm element size. In the linear region of the numerical solutions, CPE4I and CPE4R models give closer results to analytical solution, but for the propagation region, CPE4 model result is closer to the analytical solution. All models show an oscillatory behavior indicating the convergence difficulty.

To pronounce the effect of the element type on the results, results of the coarser mesh models with 0.60 mm element size are given in Figure 4.6. CPE4I and CPE4R models still give closer results to analytical one. CPE4 model stiffness is decreased in the linear part of the curve, additionally result diverges from the analytical solution in the propagation region, and oscillatory behavior gets worse. The use of CPE4I and CPE4R elements seem to be safer for coarse mesh models. Alfano and Crisfield [54] reported also the importance of enhanced strains in the elements to get closer results to the analytical solution.

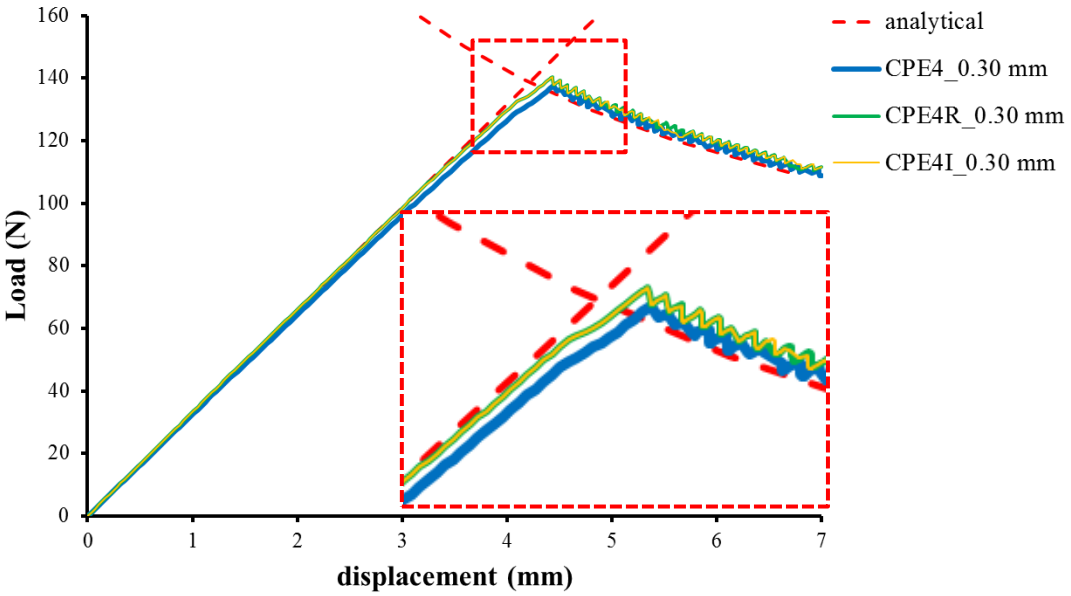

Figure 4.5- Effect of the element type on the DCB load-displacement behavior (element size = 0.30 mm)

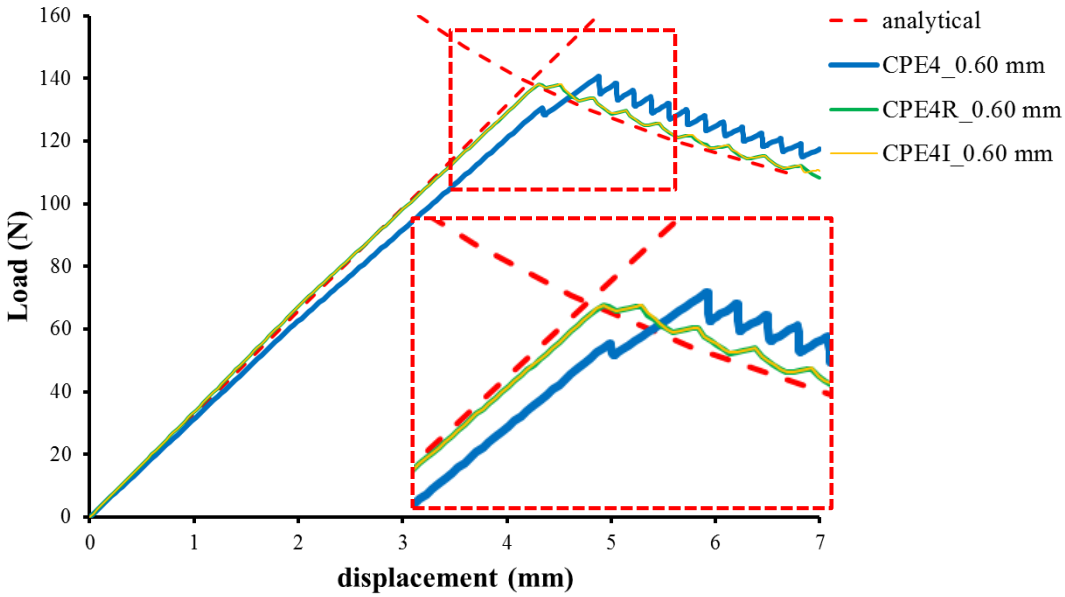

Figure 4.6- Effect of the element type on the DCB load-displacement behavior (element size = 0.60 mm)

Effect of the Element Size

In numerical simulations, element size affects the load-displacement, delamination initiation and propagation and also the convergence behaviors. For initial estimations, it is recommended that at least 3-5 elements should be used in

the cohesive zone [20, 50, 56]. The cohesive zone length is the distance between the crack tip and the maximum traction as shown in Figure 4.7 and can be calculated for Mode I as [56]:

$$l_{CZI}=ME_{22}\frac{G_{IC}}{(t_I^0)^2} \quad (4.8)$$

For Mode II and III, similar equations can be used:

$$l_{CZII}=ME_{22}\frac{G_{IIC}}{(t_{II}^0)^2} \quad (4.9)$$

$$l_{CZIII}=ME_{22}\frac{G_{IIIC}}{(t_{III}^0)^2} \quad (4.10)$$

where, "M" is a parameter that depends on the cohesive model, Dugdale and Barenblatt used M=0.4, Rice used M = 0.88 and Hillerborg used with M = 1 [56]. In this study, according to above equations with M=1, cohesive lengths for Mode I, II and III are 1.53 mm, 1.74 mm, 1.74 mm, respectively.

Figure 4.8 shows that for CPE4 element model, as element length gets smaller from 0.60 mm to 0.30 mm then 0.15 mm, numerical results converge to the analytical solution; initial stiffness increases and oscillatory behavior disappears in the softening region. This situation agrees with the results in [20]. Another point to mention is the increment number, because finest mesh with 0.15 mm element length shows no oscillatory behavior, 286 increments are enough for convergence whereas 341 and 360 increments are required for 0.30 mm and 0.60 mm element length models, respectively.

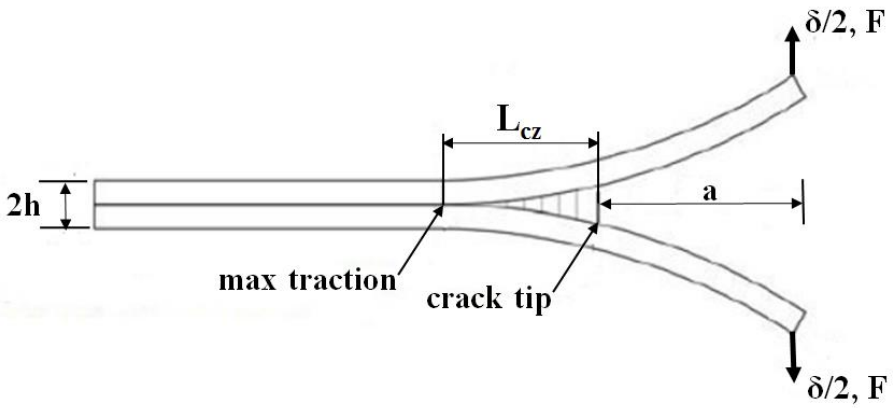

Figure 4.7- Cohesive zone length in the DCB

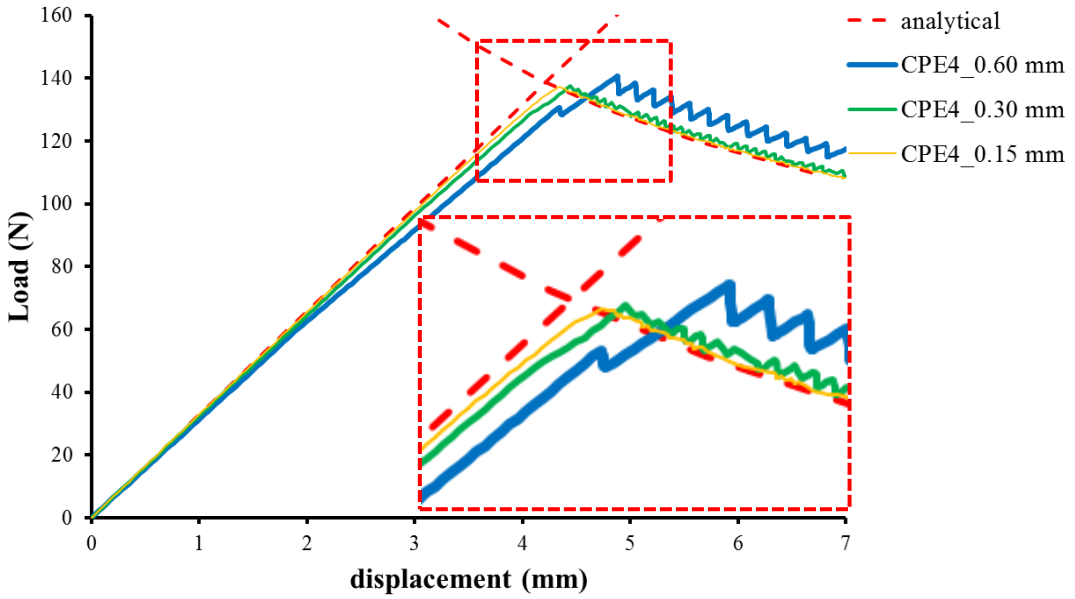

Figure 4.8- Effect of the element size on the DCB load-displacement behavior

In the following numerical studies with DCB test, further investigations of cohesive parameters are done with CPE4I element type with 0.15 mm element size to eliminate the element type and size effects on the results. By keeping the other parameters constant, only one parameter is changed in each step.

Effect of the Viscosity (v)

The oscillatory behavior present in the coarse mesh models can be prevented by increasing the viscosity parameter. Viscosity causes the tangent stiffness matrix to be positive in small time intervals [22, 42].

Figure 4.9 shows that linear parts of the numerical solutions remain same with the change in viscosity values. Differences are seen in the softening regions. Increasing the viscosity value to 1e-4 increases the area under the load-displacement curve. Decreasing the viscosity value to 1e-6 causes an oscillatory behavior and requires 897 incremental steps for simulation which is more than twice the base model increments. Further decrease in the viscosity causes convergence problems. The area under load-displacement curve for 1e-6 viscosity remains almost the same with the base model which shows that 1e-5 value is an optimal choice for the viscosity by keeping the other parameters constant.

From the results of different viscosity values in Figure 4.9, it can be stated that increase in the viscosity value eliminates the oscillatory behavior and requirement of finer mesh. However, use of higher values may cause unconservative results with an increase in viscous dissipation energy; therefore care should be taken when using high viscosity values.

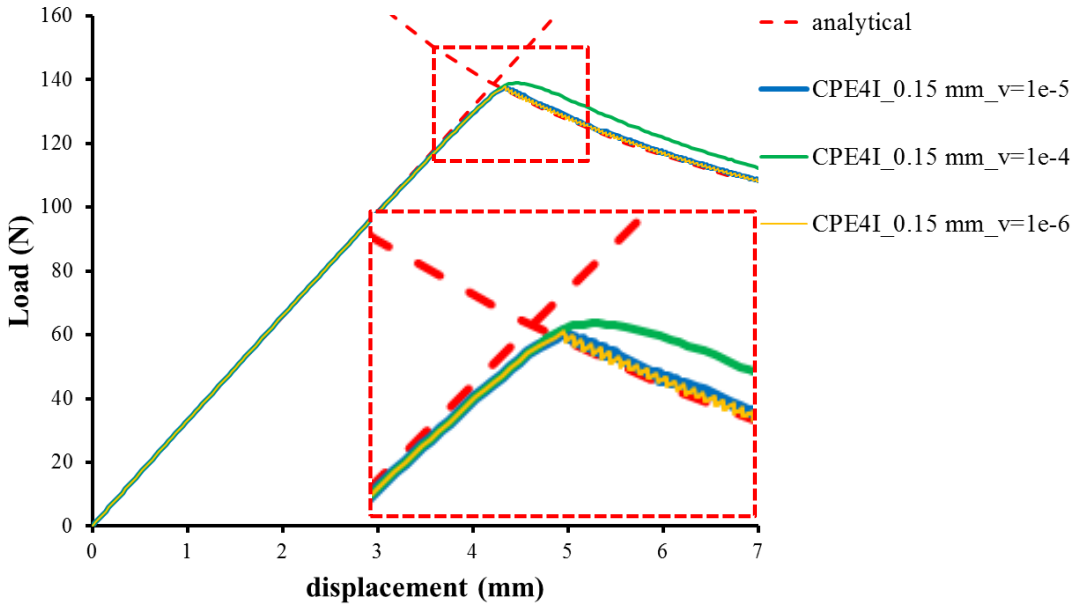

Figure 4.9- Effect of the viscosity on the DCB load-displacement behavior

Effect of the Penalty Stiffness

As shown in Figure 4.10, FE model with very low penalty stiffness, 1e2, shows a decreased elastic stiffness and no delamination occurs for the same displacement applied to the base model. FE models with very high stiffness values have the same initial elastic behavior with the base model, even for very high stiffness value of 1e11. However, the area under load-displacement curve increases and the solution diverges from the analytical solution. In addition, result shows oscillatory behavior for high penalty stiffness compared to the results for lower stiffness. The results agree with the results in reference [56]. Alfano et al. [50] also stated that extremely stiff elements cause numerical instabilities.

One interesting result of the increased penalty stiffness is the increase in the stress values around the crack tip. From Figure 4.11, it can be seen that as penalty

stiffness increases, stress values around the crack tip increase to a value higher than the interface strength value of 80 MPa. Maximum S22 values are around 80 MPa, 96 Mpa and 171 MPa for k=1e6 N/mm^3, k=1e8 N/mm^3 and k=1e11 N/mm^3, respectively. Final crack length of the model with high stiffness is also smaller than the base model, which are 6.58 mm and 9.58 mm, respectively.

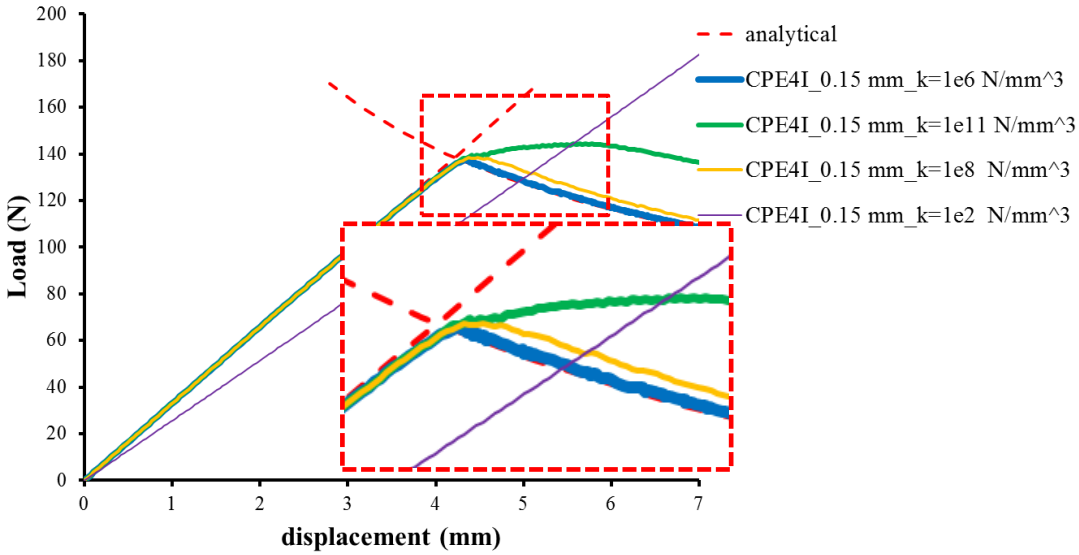

Figure 4.10- Effect of the penalty stiffness on the DCB load-displacement behavior

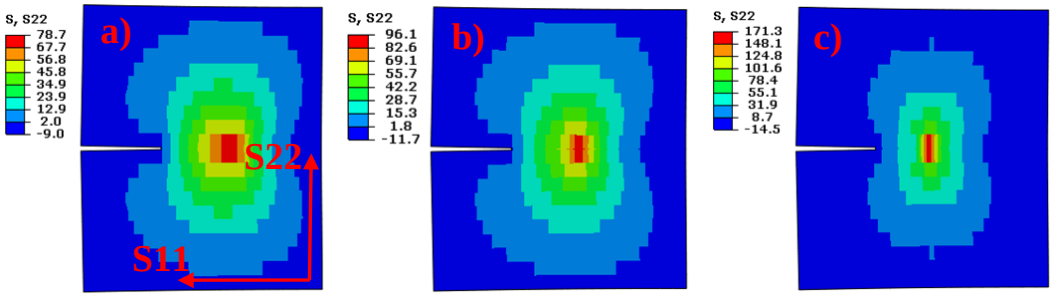

Figure 4.11- S22 Stress field for a) k=1e6 N/mm^3, b) k=1e8 N/mm^3 and c) k=1e11 N/mm^3

According to Equation (3.21), for α=50, penalty stiffness value, k, is equal to 3.23x10^5 N/mm^3 for the DCB specimen. The calculated k value is close to assumed k value of 1e6 N/mm^3 which give reliable results compared with the other penalty stiffness values investigated.

Effect of the Interface Strength

Decreasing the Mode I interface strength value to 40 MPa from 80 MPa decreases the initial stiffness near the delamination point and the maximum traction as shown in Figure 4.12 (t_I in the figure stands for t_I^0). The area under load-displacement curve remains almost the same. Numerical solution gets closer to analytical result as interface strength increases to 120 MPa. Therefore, main effect of the strength value on the results is on the maximum traction which agrees with the results in reference [50]. The advantage of decreasing the strength value is the increased cohesive zone length, therefore coarser mesh can be used which eliminates the convergence difficulties.

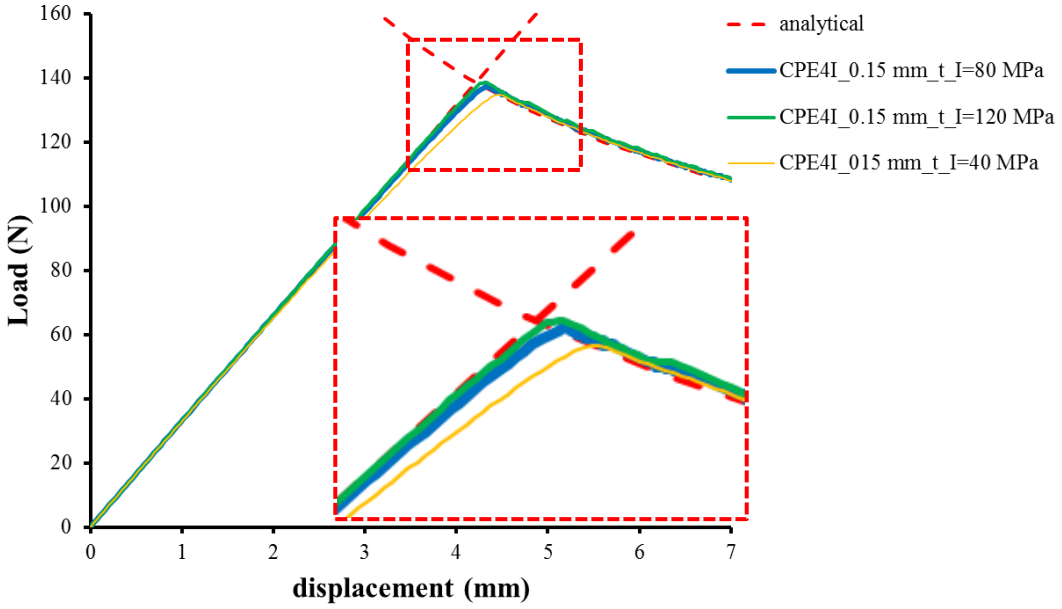

Figure 4.12- Effect of the interface strength on the DCB load-displacement behavior

Effect of the Fracture Toughness

Increasing the fracture toughness means increase in the absorbed energy by the cohesive elements; therefore the area under the load-displacement curve increases by increasing Mode I fracture toughness to 1.2 N/mm from 0.969 N/mm as shown in Figure 4.13 (G_IC in the figure stands for G_{IC}). Decreasing fracture toughness to 0.8 N/mm decreases the area under the load-displacement curve. Initial stiffness of the structure is not affected by fracture toughness change

whereas maximum traction increases with increasing fracture toughness. The results agree with the results in reference [50].

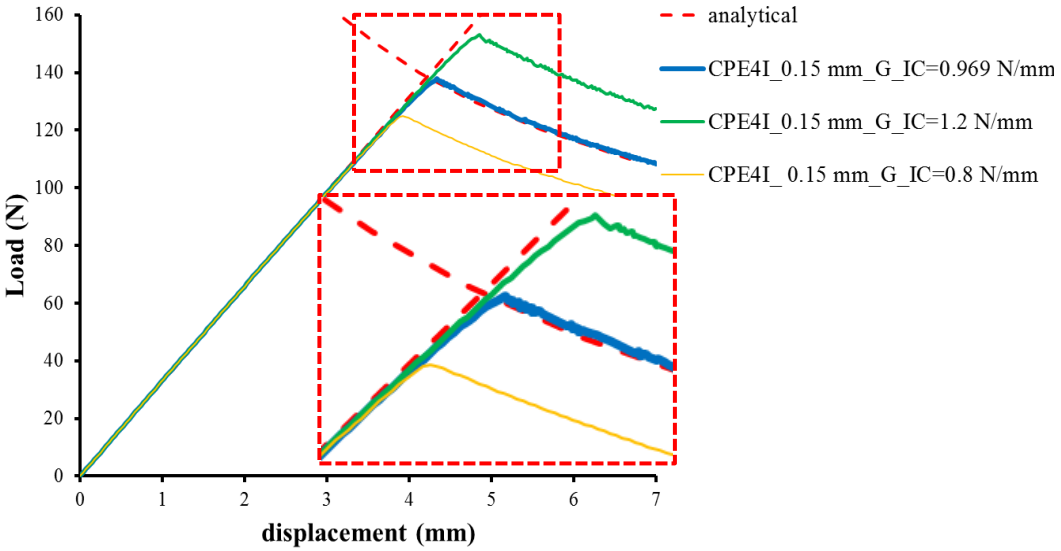

Figure 4.13- Effect of the fracture toughness on the DCB load-displacement behavior

Crack growth and cohesive zone lengths in DCB sensitivity study

Table 4.5 shows the crack growth and cohesive zone lengths for the models considered in the DCB sensitivity study. Crack growth length is the final length of the phsical crack. Cohesive zone length is the distance between the crack tip and the maximum traction point as shown in Figure 4.7.

Crack length and cohesive zone length are slightly changed for the considered viscosity range. High penalty stiffness values, 1e11 N/mm^3, decrease both crack length and cohesive zone length. A decrease in the interface strength value decreases the crack length and increases the cohesive length much whereas, increase in the interface strength has the opposite effects of decreasing. A decrease in the Mode I fracture toughness increases the crack length much but the cohesive zone length remains the same. Increasing the Mode I fracture toughness decreases the crack length but increases the cohesive zone length.

Table 4.5- Crack growth and cohesive zone lengths in DCB sensitivity study

FE model	Crack Growth Length [mm]	Cohesive Zone Length [mm]
CPE4I_0.15 mm (v = 1e-5, k = 1e6 [N/mm^3], t_I^0 = 80 [MPa], G_{IC} = 0.969 [N/mm])	9.87	0.75
CPE4I_0.15 mm_v = 1e-6	9.87	0.90
CPE4I_0.15 mm_v = 1e-4	9.27	0.82
CPE4I_0.15 mm_k = 1e2 [N/mm^3]	0.00	0.00
CPE4I_0.15 mm_k = 1e8 [N/mm^3]	9.42	0.75
CPE4I_0.15 mm_k = 1e11 [N/mm^3]	6.58	0.60
CPE4I_0.15 mm_t_I^0 = 40 [MPa]	9.12	1.87
CPE4I_0.15 mm_t_I^0 = 120 [MPa]	10.02	0.45
CPE4I_0.15 mm_G_{IC} = 0.8 [N/mm]	12.12	0.75
CPE4I_0.15 mm_G_{IC} = 1.2 [N/mm]	7.33	1.05

4.3 ENF Investigation

ENF test is the generally used test method for Mode II fracture toughness evaluations and under development by ASTM-WK22949 [36]. In ENF test, specimen is supported at both ends in vertical directions and load is applied at the mid of the specimen which creates a Mode II sliding shear between the sublaminates as shown in Figure 4.14. During the test, load-displacement behavior is recorded and G_{IIC} curve is generated with test data reduction schemes.

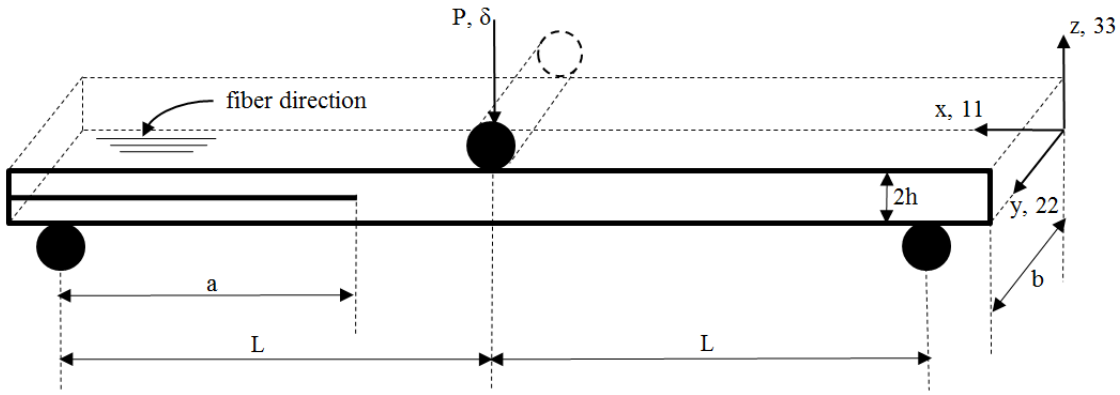

Figure 4.14- ENF test, loading and BCs

In this study, load-displacement curve of the ENF test is also evaluated with the MBT as in DCB test [21, 23, 37]. The results are compared with the Abaqus numerical solution and with the additional data from Albiol [21].

4.3.1 Comparison of Analytical and Numerical Results

Analytical solution:

As in DCB test, to take the rotation and shear deformations at the crack tip into account, crack length "a" is modified by a factor $0.42\chi h$. Load point displacement can then be calculated as:

$$\delta = \frac{3(a+0.42\chi h)^3+2L^3}{96E_{11}I}P \qquad (4.11)$$

"χ" and "Γ" factors are calculated by Equations (4.2) and (4.3) in DCB section. In LEFM, Mode II compliance (C_{II}) and energy release rate (G_{II}) can be calculated as:

$$C_{II} = \frac{\delta}{P} = \frac{3(a+0.42\chi h)^3+2L^3}{96E_{11}I} \quad (4.12)$$

$$G_{II} = \frac{P^2}{2b}\frac{dC}{da} = \frac{3P^2(a+0.42\chi h)^2}{64bE_{11}I} \quad (4.13)$$

Classical beam theory solution can be evaluated by setting χ=0. After initial delamination, load carried by the specimen starts to decrease with increasing displacement. Displacement for the propagation region can be calculated by assuming $G_{II}=G_{IIC}$ and extracting "a" from Equation (4.13) then inserting the result in Equation (4.11).

Analytical solution of the ENF test is shown in Figure 4.15. The intersection of the linear and non-linear curves corresponds to the delamination initiation.

Numerical model:

An FE model is created with plane strain assumption for ENF test simulation in Abaqus with the below specifications:

- A cohesive layer is inserted between the two sublaminates with a thickness of 0.001 mm.
- 0.30 mm element size is used for both composite and cohesive sections.
- 3400 CPE4 elements for composite section, 209 COH2D4 elements for cohesive section are used. A total number of 4092 nodes are present in the model. In ENF model, contact is simulated between the crack surfaces to prevent the penetration of the surfaces into each other. Friction is neglected on the contact surfaces.
- A viscosity parameter with a value of 1e-5 is used to help the convergence.
- 5mm prescribed displacement is applied at the mid-point of the specimen. Lower right edge of the specimen is constraint in the vertical (1^{st}) and through thickness (3^{rd}) directions. Lower left edge of the specimen is constraint in the through thickness (3^{rd}) direction.

Numerical solution is shown in Figure 4.15. The MBT and the numerical solutions agree quite well as seen from the figure. The slight nonlinearity in the numerical curve until the initiation is caused by the accumulation of the damage in the cohesive elements as in DCB case. After delamination initiation, load starts to decrease with increasing displacement. The oscillatory behavior in the DCB result is not present in the ENF result, because cohesive zone length is larger and element size is less restrictive for the ENF model. The increase in stiffness at the end of the numerical curve is caused by the stabilization of the delamination. Experimental and numerical results from [21] are provided in Figure 4.16. The results agree quite well also with numerical solution carried by Abaqus CZM (Figure 4.15). Therefore, it can be considered that Abaqus CZM gives reliable results for delamination simulation for the ENF test.

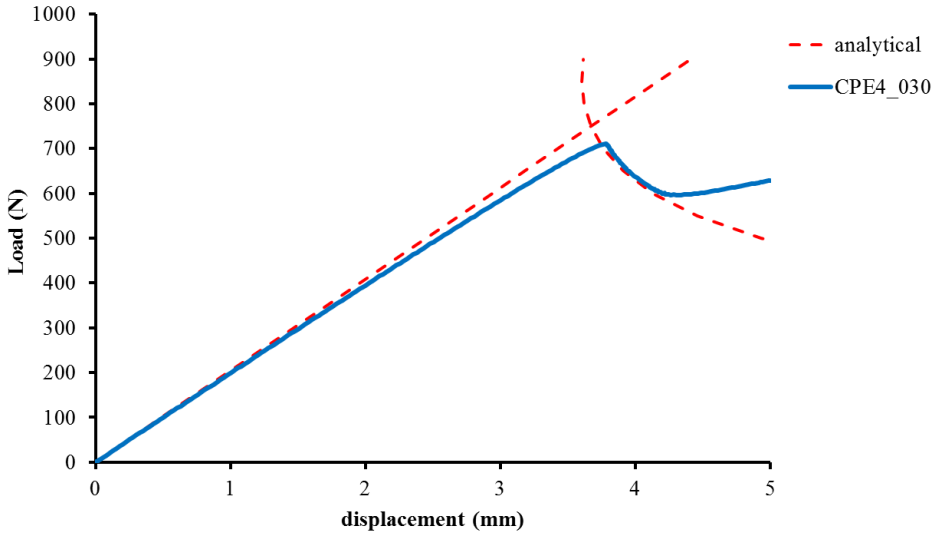

Figure 4.15- Analytical and numerical solutions for the ENF test

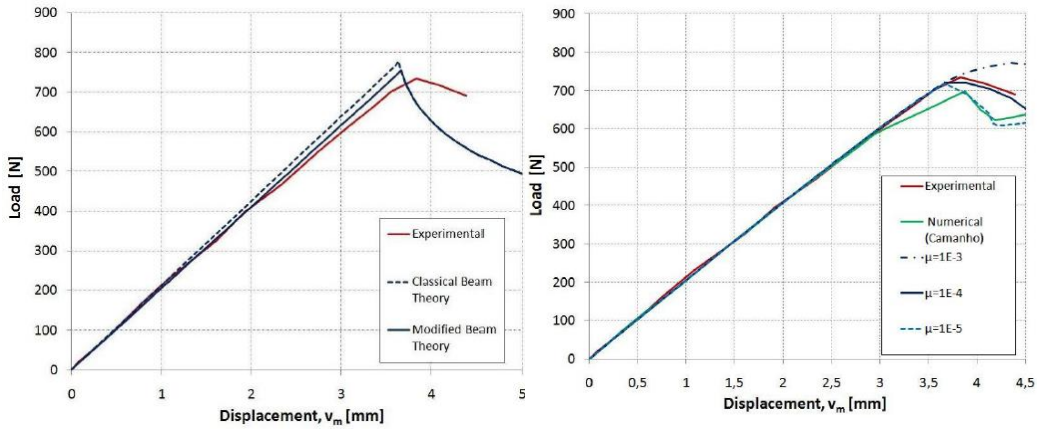

Figure 4.16- ENF analytical, numerical and experimental solutions from the reference [21]

4.3.2 Numerical Sensitivity Study

In this chapter, some FE and cohesive parameters are investigated in a sensitivity study to see their effects on the ENF numerical results.

Effect of the Element Type

Figure 4.17 shows that, results are close to each other for models with CPE4, CPE4R and CPE4I element types and 0.30 mm element size. In the linear region of the numerical solutions, CPE4I and CPE4R models give closer results to analytical solution, but for the propagation region, CPE4 model result is closer to the analytical solution. Oscillatory behavior is not seen in the softening region for ENF simulation.

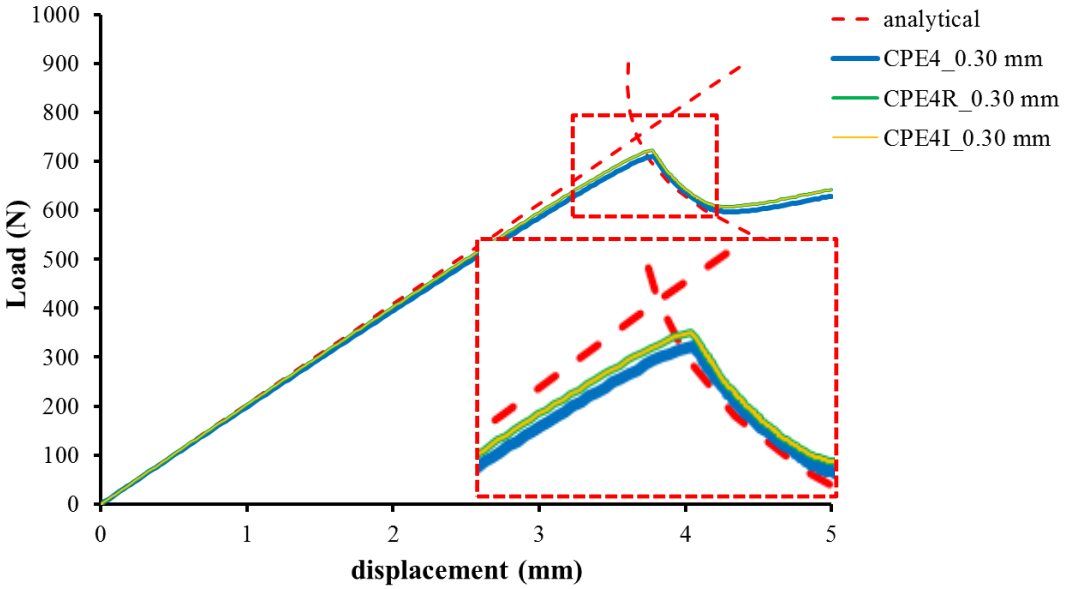

Figure 4.17- Effect of the element type on the ENF load-displacement behavior (element size = 0.30 mm)

Effect of the Element Size

Figure 4.18 shows that for CPE4 model, as element length gets smaller from 0.60 mm to 0.30 mm then 0.15 mm, numerical results converge to the analytical solution, initial stiffness increases and oscillatory behavior disappears for softening region. Another point to mention is the increment number, because finest mesh shows no oscillatory behavior, 231 increments are enough for convergence whereas 310 and 319 increments are required for 0.30 mm and 0.60

mm mesh models, respectively. The results presented in Figures 4.18 shows that ENF is less sensitive to element size with less oscillatory behavior compared to DCB, because of the larger cohesive zone length.

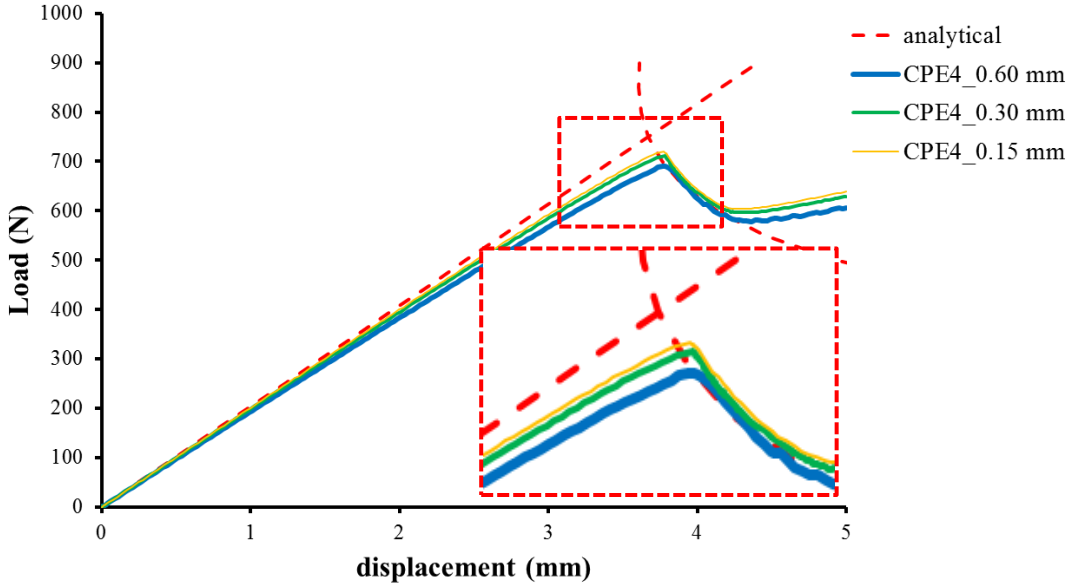

Figure 4.18- Effect of the element size on the ENF load-displacement behavior

In the following chapters, further investigations of cohesive parameters are done with CPE4I model with 0.30 mm element size to eliminate the element type and size effects. By keeping the other parameters constant, only one parameter is changed in each step.

Effect of the Viscosity (v)

Figure 4.19 shows that linear parts of the solutions remain same with the change in viscosity values. Difference is mainly seen in the softening regions. Increasing the viscosity value to 1e-4 increases the area under the load-displacement curve and gives a smoother load-displacement curve rather than the sudden load drop at the delamination initiation. Decreasing viscosity value to 1e-6 causes the oscillatory behavior and requires 463 incremental steps which is more than the base model increments. Further decrease in viscosity causes convergence problems. The area under load-displacement curve remains almost the same for 1e-6 value which shows that 1e-5 value is an optimal choice for viscosity by keeping the other parameters constant.

From the results of different viscosity ratios in Figure 4.19, it can be stated that increase in the viscosity value eliminates the oscillatory behavior and requirement of finer mesh. However, use of higher values may cause unconservative results with an increase in viscous dissipation energy; therefore care should be taken when using high viscosity values.

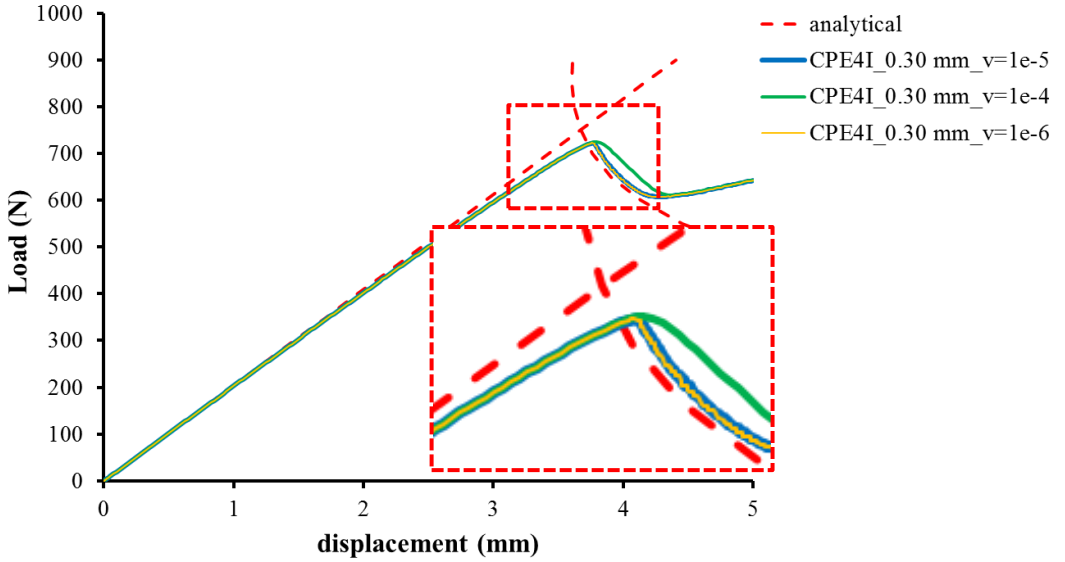

Figure 4.19- Effect of the viscosity on the ENF load-displacement behavior

Effect of the Penalty Stiffness

As shown in Figure 4.20, FE models with very low penalty stiffness, 1e2 N/mm^3, show a decreased elastic stiffness and no delamination occurs with the same displacement applied to the base model. FE model with very high penalty stiffness, even for very high values of 1e11 N/mm^3, has almost the same load-displacement curve with the base model. However, solution is achieved for only 4.84 mm of the prescribed 5mm displacement and 5001 increments are required for the complete solution while 310 increments are enough for the base model. This situation shows the convergence difficulty for the increased penalty stiffness. In reference [65], stress oscillations are reported at the crack tip for high stiffness values as seen in Figure 4.21.

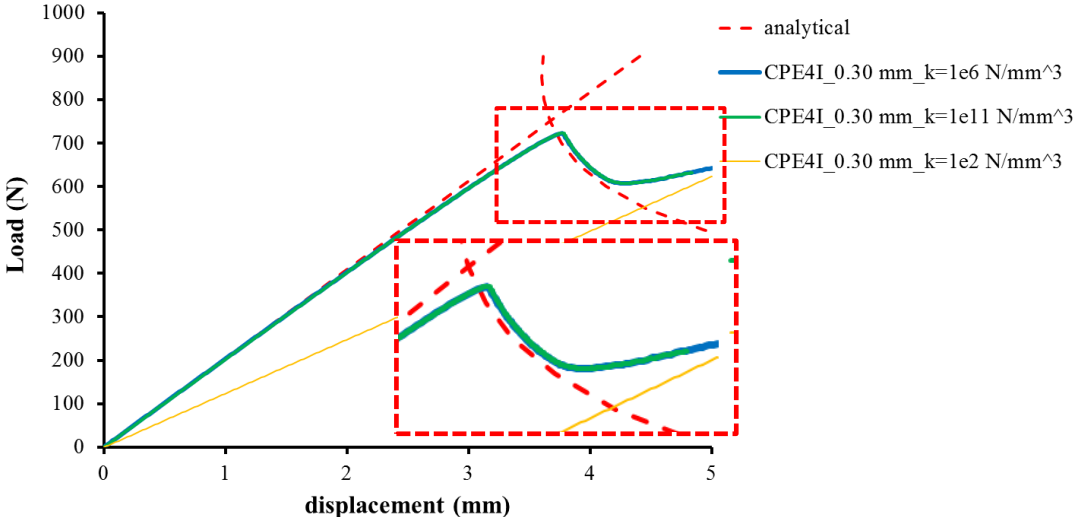

Figure 4.20- Effect of the penalty stiffness on the ENF load-displacement behavior

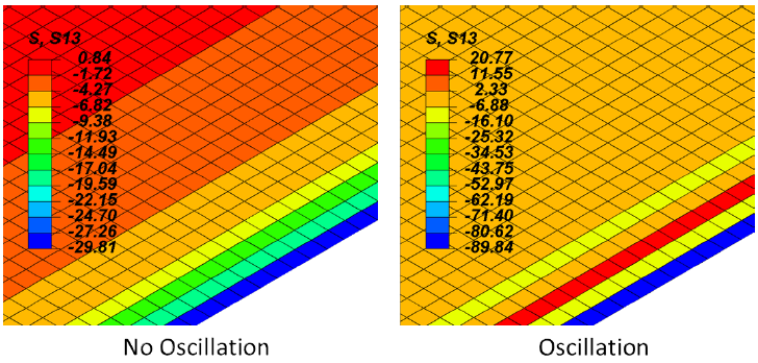

Figure 4.21- Example of stress oscillation at the crack tip in the cohesive layer of an ENF model [65]

Effect of the Interface Strength

Decreasing the Mode II interface strength value to 50 MPa from 100 MPa decreases the initial stiffness near the delamination point and the maximum traction as shown in Figure 4.22 (t_II in the figure stands for t_{II}^0). The area under load-displacement curve almost remains the same. Numerical solution gets closer to analytical result as interface strength increases to 150 MPa. Therefore, main effect of the strength value on the results is on the maximum traction similar to DCB. Decreasing the strength value increases the cohesive zone length, therefore coarser mesh can be used for numerical simulations.

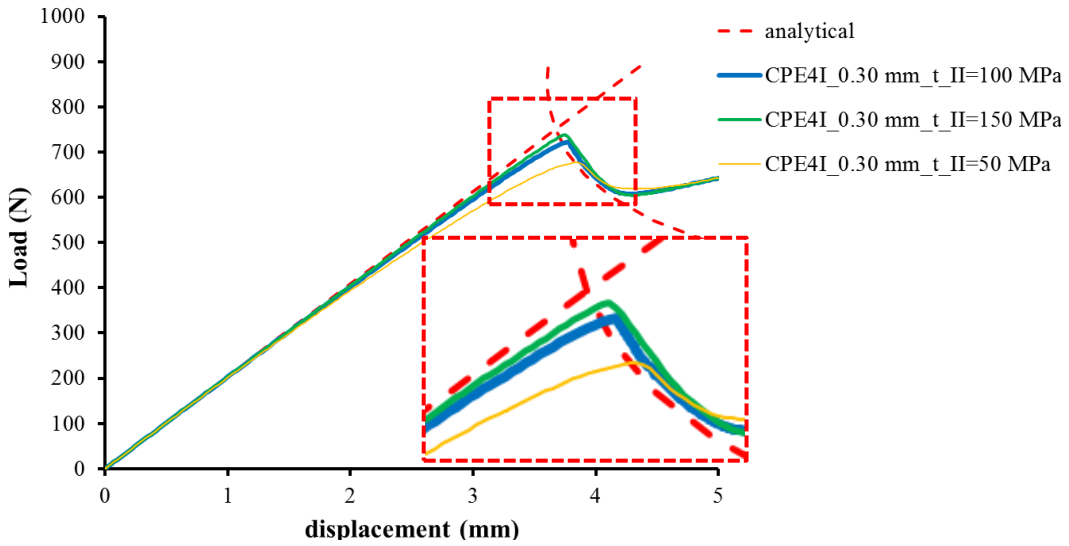

Figure 4.22- Effect of the interface strength on the ENF load-displacement behavior

Effect of the Fracture Toughness

Increasing the fracture toughness means increase in the absorbed energy by the cohesive elements; therefore the area under the load-displacement curve increases by increasing Mode II fracture toughness to 2.0 N/mm from 1.719 N/mm as shown in Figure 4.23 (G_IIC in the figure stands for G_{IIC}). Decreasing fracture toughness to 1.5 N/mm decreases the area under load-displacement curve. Initial stiffness of the structure is not affected by fracture toughness change whereas the maximum traction increases by increasing the fracture toughness.

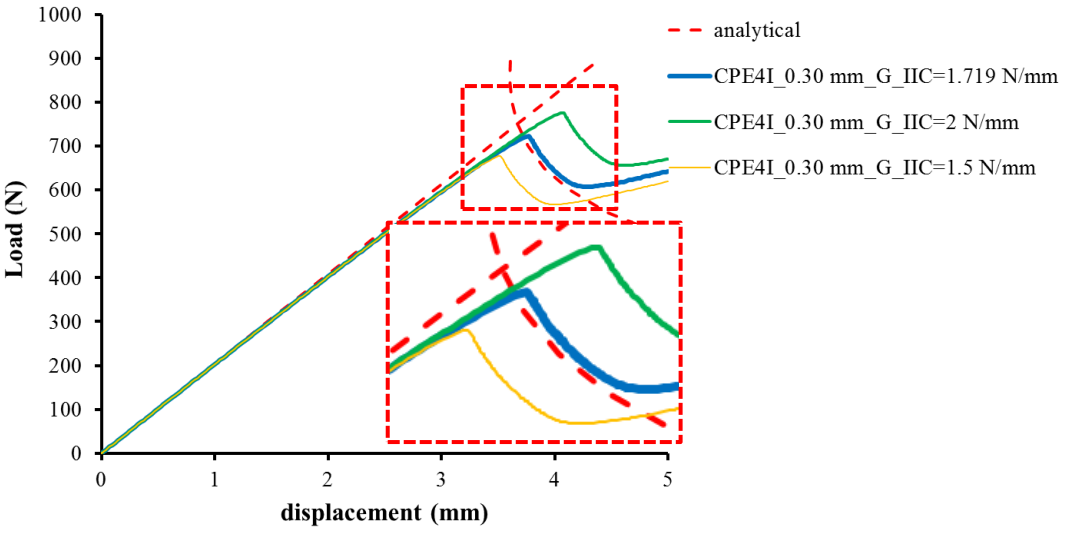

Figure 4.23- Effect of the fracture toughness on the ENF load-displacement behavior

4.4 MMB Investigation

MMB test is the generally used test method for Mixed Mode I and II fracture toughness evaluations and is standardized by ASTM (D6671) [37]. In MMB test, specimen is supported at both ends in vertical direction and loads are applied at the end of the specimen and at the mid of the specimen at the same time with a specially designed fixture as seen in Figure 4.24. Primary advantage of the MMB test is that by changing the lever length, c, different mixed-mode ratios can be obtained corresponding to different mixed-mode fracture toughness. During the test, load-displacement behavior is recorded and G_C curve is generated with test data reduction schemes.

MMB can be considered as a combination of the DCB and ENF tests. Therefore, MBT solutions of the DCB and ENF tests can be combined for MMB analytical solution [21, 23, 37, 70, 41]. In this study, analytical solution of the load-displacement curve of the MMB test is created with the MBT. The results are compared with the Abaqus numerical solution and with the additional data from Albiol [21].

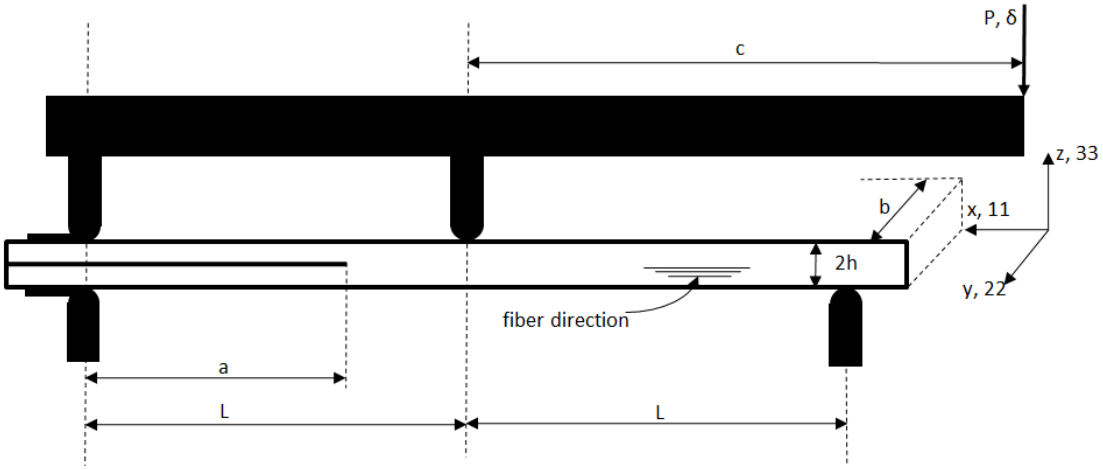

Figure 4.24- MMB test, loading and BCs

Analytical solution:

Figure 4.25 shows that load on the MMB specimen can be decomposed into Mode I and Mode II load components. Mode I (P_I), and Mode II load (P_{II}) components can be calculated as [70]:

$$P_I = \frac{3c-L}{4L} P \tag{4.14}$$

$$P_{II} = \frac{c+L}{L} P \tag{4.15}$$

Lever displacement can be calculated as [23]:

$$\delta_{lever} = \frac{3c-L}{4L} \delta_I + \frac{c+L}{L} \delta_{II} \tag{4.16}$$

δ_I and δ_{II} are calculated by using Equations (4.1) and (4.11). The compliance and the energy release rates can be obtained as [23, 37]:

$$C = C_I + C_{II} = \frac{\delta_I}{P_I} + \frac{\delta_I}{P_{II}} = \frac{2(a+\chi h)^3}{3E_{11}I} + \frac{3(a+0.42\chi h)^3+2L^3}{96E_{11}I} \tag{4.17}$$

$$G_I = \frac{(a+\chi h)^2}{bE_{11}I} P_I^2 = \frac{(a+\chi h)^2}{bE_{11}I} \left(\frac{3c-L}{4L}\right)^2 P^2 \tag{4.18}$$

$$G_{II} = \frac{3(a+0.42\chi h)^2}{64bE_{11}I} P_{II}^2 = \frac{3(a+0.42\chi h)^2}{64bE_{11}I} \left(\frac{c+L}{L}\right)^2 P^2 \tag{4.19}$$

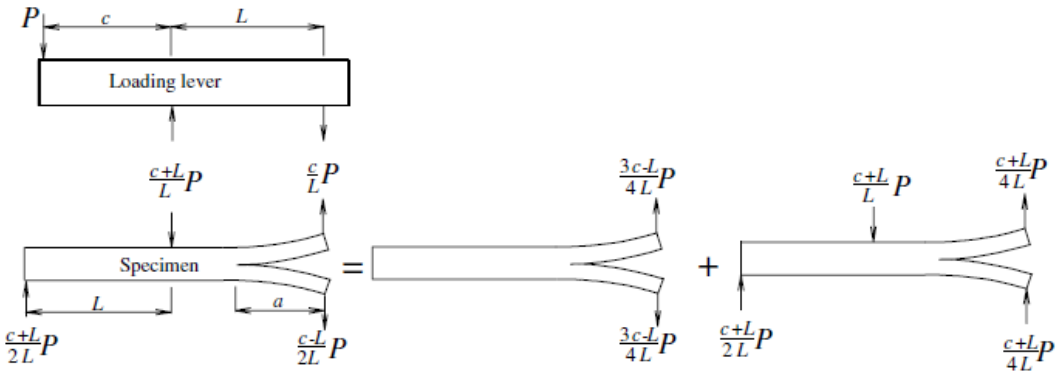

Figure 4.25- MMB load decomposition [70]

Total energy release rate can then be evaluated as:

$$G_T = G_I + G_{II} \tag{4.20}$$

By neglecting the crack the tip rotations and the shear deformations, it can be seen that G_I/G_{II} is independent of the crack length and the applied load. Lever length, c, is the only parameter affecting G_I/G_{II} ratio:

$$\frac{G_I}{G_{II}} = \frac{4}{3}\left(\frac{3c-L}{c+L}\right)^2 \quad (4.21)$$

Therefore, mode ratio is evaluated as constant during the propagation by the classical beam theory. Additionally, Reeder and Crews [23] provided MMB test results which show that the G_I/G_{II} ratio is almost constant during propagation.

For mixed-mode ratio, m, lever length, c, in the above equations can be calculated as [37]:

$$c=\frac{\beta^2+3\alpha+8\beta\sqrt{\alpha}}{36\beta^2-3\alpha}L \quad (4.22)$$

$$\alpha=\frac{1-m}{m} \quad (4.23)$$

$$\beta=\frac{\alpha+\chi h}{\alpha+0.42\chi h} \quad (4.24)$$

$$m=G_{II}/G_T \quad (4.25)$$

Analytical solution of the MMB test is shown in Figure 4.26. The non-linear part of the curve can be evaluated similar to the single mode tests.

Numerical model:

From DCB and ENF numerical studies, it can be observed that the investigated FE model and interface parameters have the same effect on the results. Therefore, only one numerical simulation is provided for the MMB test with the optimized parameters according to the DCB and ENF numerical studies. MMB FE model is created with the following properties:

- 0.2 mode ratio (m) is chosen for MMB study and "c" value is calculated as 101.15 mm from Equation (4.22).
- Loading fixture is modeled with steel isotropic material properties with 210 GPa elasticity modulus and 0.30 poissons ratio.
- A cohesive layer is inserted between the two sublaminates with a thickness of 0.001 mm.
- 0.30 mm element size is used both for composite and cohesive sections.

- 3730 CPE4I elements for composite section, 261 COH2D4 elements for cohesive section, 1336 CPE4I and 4CPE3 elements for loading fixture are used. A total number of 6053 nodes are present in the model.
- A viscosity parameter with a value of 1e-5 is used to help the convergence.
- A 12 mm prescribed displacements are applied from the lever end. Lower left edge of the specimen is constraint in 1st direction as in DCB case. Other end of the specimen is supported with a steel cylinder in contact conditions.

Numerical solution for the MMB test is shown in Figure 4.26. The MBT and the numerical solutions agree quite well as seen from the figure. The slight nonlinearity in the numerical curve until the initiation is caused by the accumulation of the damage in the cohesive elements as in the DCB and ENF cases. The difference between the analytical and numerical results in the softening region is due to the change in the mixed-mode ratio during the delamination propagation [20]. The oscillatory behavior in the softening region can be eliminated with a finer mesh, higher viscosity value or low interface strength. Experimental and numerical results from [21] are provided in Figure 4.27. The results agree quite well also with numerical solution carried with Abaqus CZM (Figure 4.26). Therefore, it can be considered that Abaqus CZM gives reliable results for delamination simulation of the MMB test.

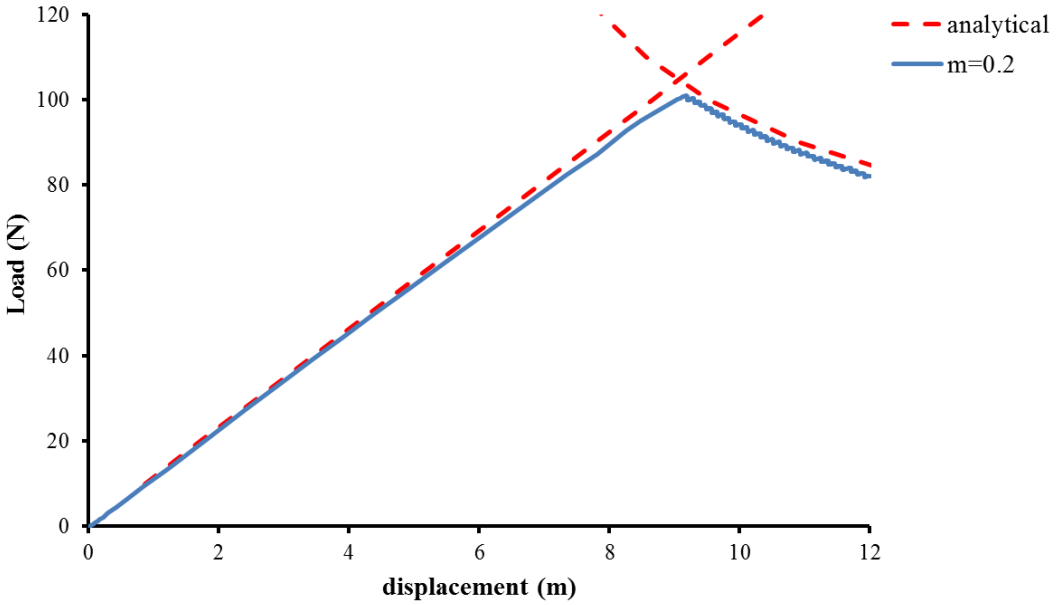

Figure 4.26- Analytical and numerical solutions for the MMB test

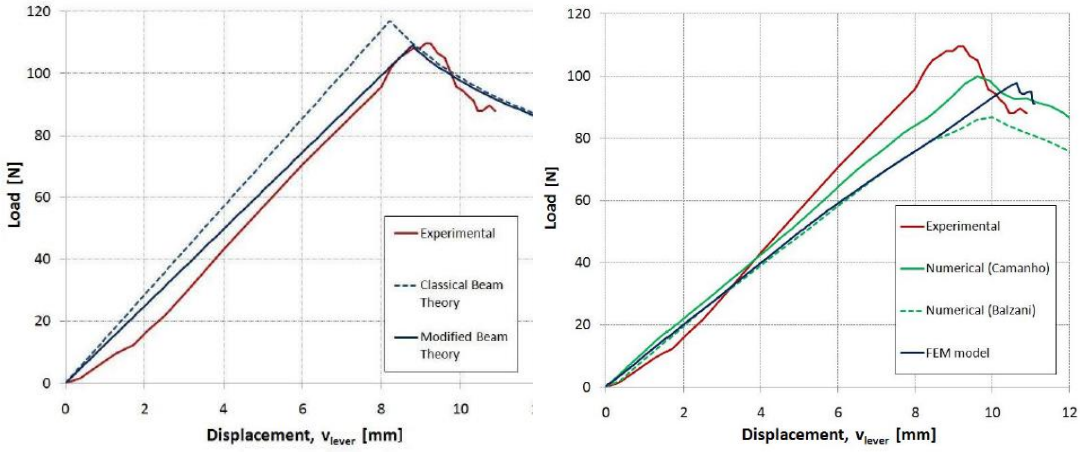

Figure 4.27- MMB analytical, numerical and experimental solutions from the reference [21]

From DCB and ENF sensitivity studies, it is shown that numerical results depend on various FE model and cohesive parameters. Depending on the requirements, an optimal solution with less computation time can be achieved by modifying the parameters. In addition to load-displacement curve comparisons, stress field, crack length and cohesive zone length comparisons are useful to determine the correct set of the parameters.

CHAPTER 5

MIXED MODE MODELING OF DAMAGE IN COMPOSITE T-JOINTS

5.1 Critical Regions in T-joints for Delamination/Debond

Delamination/debond failure is caused by the interlaminar normal and shear stresses between different constituents of structure. Failure mechanism and exact location may differ depending on the design parameters; radius, thickness, layup, filler stiffness, etc. The literature survey of T-joints shows that filler region (intersection region of the parts/ center region/ noodle area) and flange tips are the critical locations for delamination/debond initiation. The major failure mechanisms observed in the literature survey can be summarized into 4 cases as described below.

1) The first failure mechanism is the debond of the filler/stringer interface [24, 55, 66, 67] as shown in Figure 5.1. Davies and Ankerson [55] investigated a bonded skin-stringer joint under 0° pull load. They found that stress concentration around the filler region is critical in terms of delamination initiation. Debond propagations were further seen in stringer/stringer interface and skin/stringer interface after the first filler/stringer interface failure.

2) The second failure mechanism is the delamination of plies in the stringer laminate at the curved region [1, 2, 11, 12, 18, 58, 61] as shown in Figure 5.2. Helenon et al. [18] investigated a composite T-joint with cross ply laminates (skin layup $(60/0/-60/0)_{3S}$, stringer layup $(\pm 45_2/0_7/90_4/0_3)$, deltoid filled with 90° UD, ply thickness 0.127mm) under 0° pull load. They observed a delamination initiation between the stringer ply interfaces in the radius. They also observed a ply crack and growth of the delamination to neighboring interface.

3) The third failure mechanism is the debond of the stringer flange tips from the skin [1, 2, 39] as shown in Figure 5.3. Meeks et al. [39] considered the flange tip as critical failure location especially in buckled stiffened panels.

4) The fourth failure mechanism is the failure initiation by debonding of filler/stringers intersection in the vertical direction [16, 53] as shown in Figure 5.4. Zimmermann et al. [53] investigated a thick (stringer laminates with 30mm thickness) landing gear composite T-joint with non-crimped fabric (NCF) cross ply laminates. They observed a vertical delamination starting from the corner of the converging radius under 0° pull load.

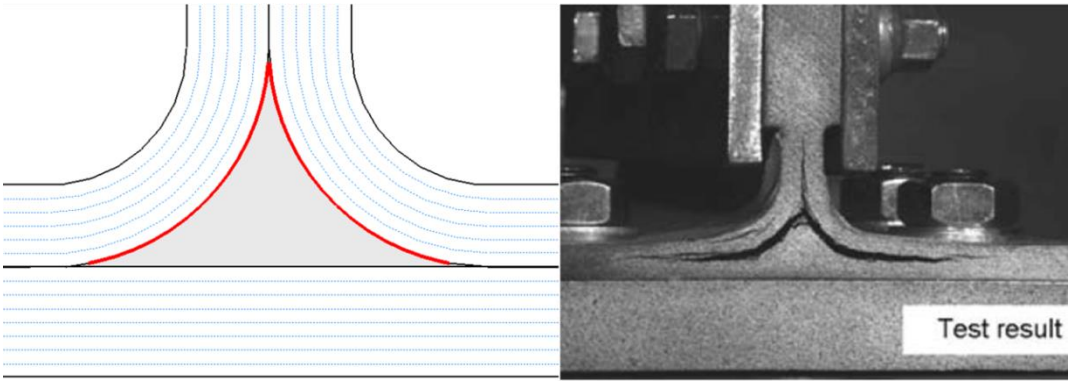

Figure 5.1- Debond between filler/stringer interfaces [55]

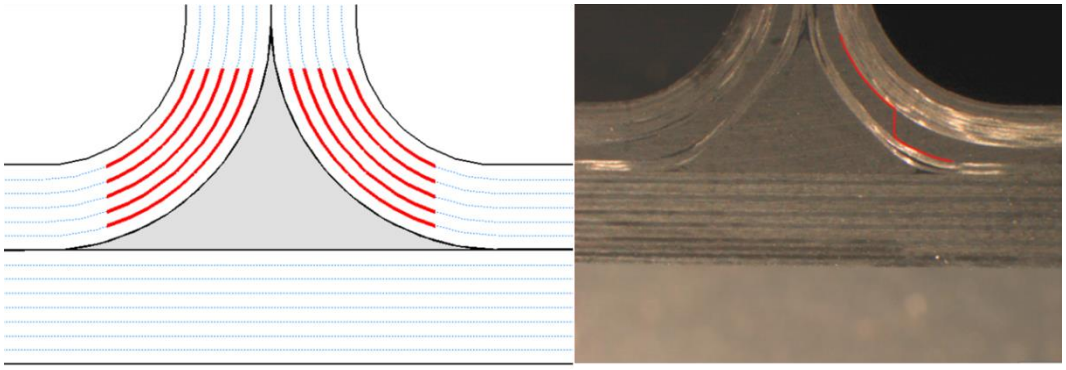

Figure 5.2- Delamination between stringer plies [18]

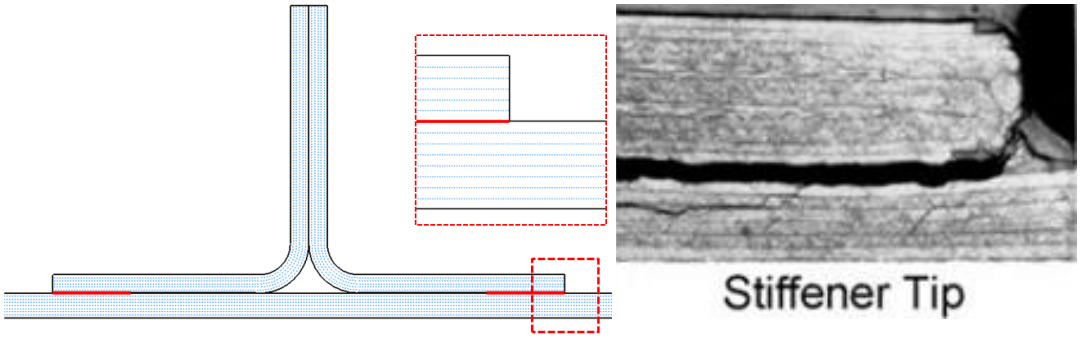

Figure 5.3- Debond of stringer flange tip from skin [39]

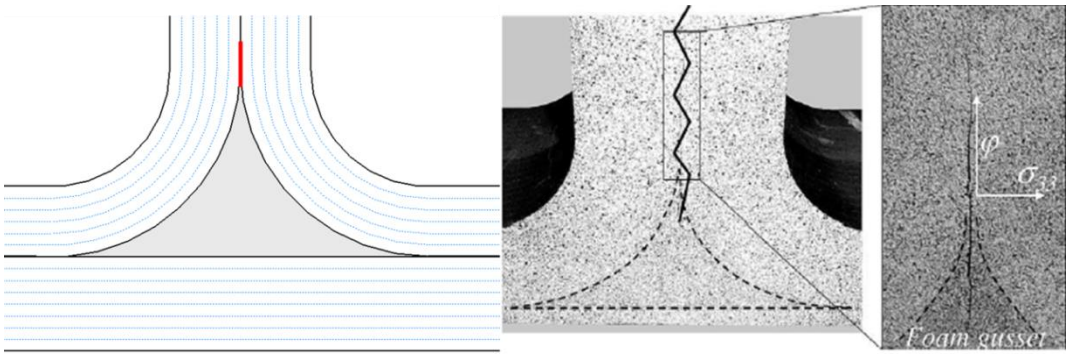

Figure 5.4- Debond at the filler/stringers intersection [53]

Apart from the above mentioned mechanisms, delamination/debond can initiate anywhere in the structure because of manufacturing induced defects; inclusion of foreign objects, resin rich areas, waviness of the plies, voids, matrix cracking because of thermal shrinkage, etc. In the literature, there are parametric studies dealing with these defects. Li et al. [14] investigated the debonds between different parts and Trask et al. [61] investigated the manufacturing defects around the filler region. Chen et al. [66, 67] investigated T-joints under 0° and 90° pull loads in which there were initial delaminations at the upper filler corner due to thermal shrinkage as seen in Figure 5.5.

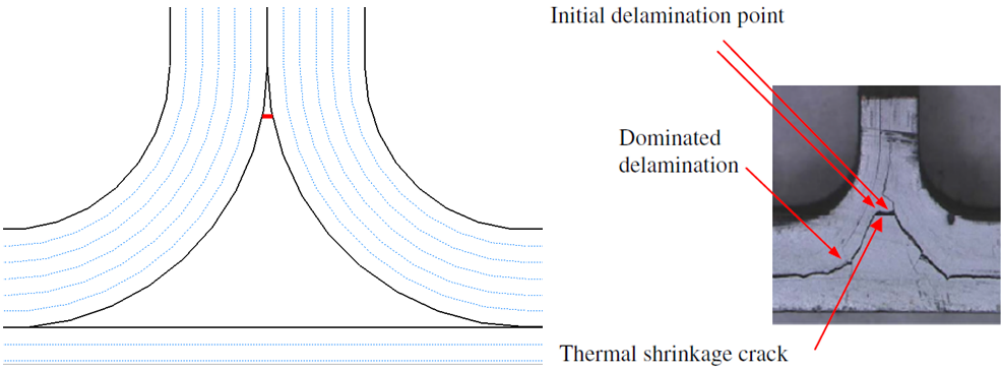

Figure 5.5- Matrix crack due to thermal shrinkage [66]

After the first failure, other mechanisms can be activated in the structure. In addition to the above mentioned failure mechanisms, matrix cracks and skin delaminations are observed in the literature. Bruyneel et al. [24] conducted a 3D numerical study (with VCE and CZM) of a composite T-joint with cross ply laminates (composed of stringer laminates, skin laminate, filler and a doubler laminate between stingers and skin) under 0° pull load as seen in Figure 5.6. Even

though, they observed a first damage in the filler/stringer interface, structure failed by the debonds between the filler/skin and stringer/skin interfaces.

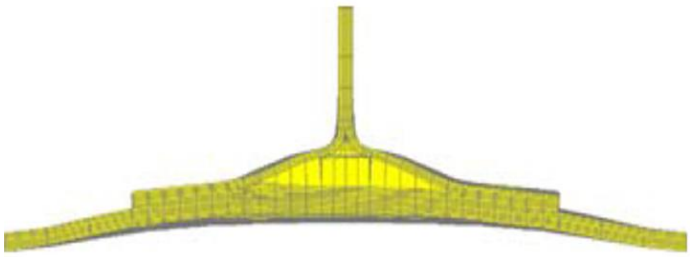

Figure 5.6- Debonds between the filler/skin and stringer/skin interfaces [24]

5.2 T-joint Study

After the geometrical and material properties of the T-joint are given in Section 5.2.1, numerical investigations of the T-joint are conducted in Section 5.2.2:

5.2.1 T-joint Geometry and FE Model

A T-joint can be divided into four main parts: 1) left stringer leg, 2) right stringer leg, 3) skin and 4) filler, where four parts are connected to each other with bonding lines as shown in Figure 5.7. In this study, T-joint geometry is taken from the reference [6] which is tested in a series of composite stiffened panel buckling experiments to investigate delamination/debond and material degradation effects on post-buckling performance. Figure 5.7 and Table 5.1 present the detailed geometry of the T-joint where t_ply, t_st, t_s are the thicknesses of the single ply,

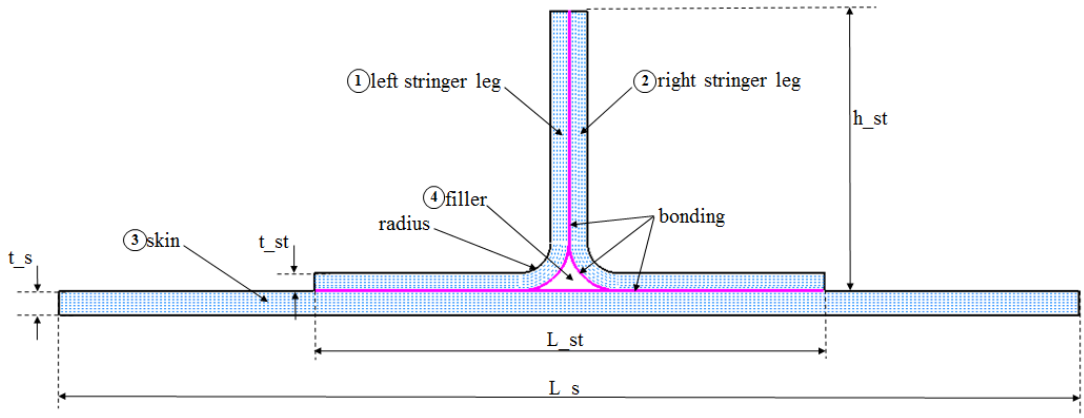

Figure 5.7- T-joint geometry and dimensions

stringer and skin, respectively, L_st and L_s are the length of the stringer and the skin, respectively, h_st is the height of the stringer.

Table 5.1– T-joint dimensions and lay-up [6]

t_ply [mm]	h_st [mm]	t_st [mm]	L_st [mm]	radius [mm]	t_s [mm]	L_s [mm]	stiffener layup	skin layup
0.15	28.0	0.90	56.0	3.0	1.20	156.0	$[45_2/0_2/90_2]$	$[45_2/0/90]s$

IM7/8552 composite material elastic and interface properties for skin and stringer legs and FM300 adhesive material elastic and interface properties for filler and bonding lines are used which are presented in Table2 and Table3 which are taken from the references [6, 71]. By using the classical lamination theory and the transformation rule, anisotropic material properties are determined for composite material according to ply direction. 0 degree is defined to be in the direction of the stringer, namely out of plane direction in this case. Ply stacking sequence is presented in Figure 5.8. Skin has a symmetric layup and composed of 8 plies. Stringer laminate stacking sequence starts from the inner radius and is composed of 6 plies starting with a 45° ply.

Table 5.2– Elastic properties of the IM7/8552 composite and FM300 adhesive materials

	E_{11} [GPa]	E_{22} [GPa]	E_{33} [GPa]	G_{12} [GPa]	G_{13} [GPa]	G_{23} [GPa]	ν_{12}	ν_{13}	ν_{23}
IM7/8552	147	11.8	11.8	6.0	6.0	4.0	0.30	0.30	0.475
FM300 (isotropic)	2.38	-	-	0.68	-	-	-	-	-

Table 5.3– Interface properties of the IM7/8552 composite and FM300 adhesive materials

	k_I^0 [MPa/mm]	k_{II}^0 [MPa/mm]	k_{III}^0 [MPa/mm]	t_I^0 [MPa]	t_{II}^0 [MPa]	t_{III}^0 [MPa]	G_{IC} [N/mm]	G_{IIC} [N/mm]	G_{IIIC} [N/mm]	η
IM7/8552	1e6	1e6	1e6	50	100	100	0.9	2.5	2.5	8
FM300	1e6	1e6	1e6	60	90	90	0.243	0.514	0.514	4.6

An FE model is constructed with Abaqus in 2D as shown in Figure 5.8 with plane strain assumption. The stringer legs and the skin are modeled with CPE4I elements with anisotropic properties whereas the filler is modeled as an isotropic material with CPE4I/CPE3 elements. For stringer and skin, 2 elements for each ply are used with 0.2 mm element length and for the filler 0.2 mm element length is used. Cohesive layers are modeled with COH2D4 elements between each layer of the stringer and the skin laminates and bonding lines. For the cohesive layers between the composite plies 0.2 mm element length is used and the cohesive layer thickness is set to be 0.001mm. For bonding lines 0.2 mm element length is used but because of modeling constraints the cohesive layer thickness changes between 0.0005 mm and 0.0015 mm. In total, there are 19260 CPE4I, 7 CPE3, 8669 COH2D4 elements and 28906 nodes in the FE model. In numerical simulations, a viscosity parameter, with a value of 1e-5, is used to ease the convergence. The quadratic stress interaction for delamination initiation and BK criterion for delamination propagation are used. Prescribed displacements are applied from the stringer upper region in a quasi-static manner and implicit non-linear solutions with line search method are carried out [22].

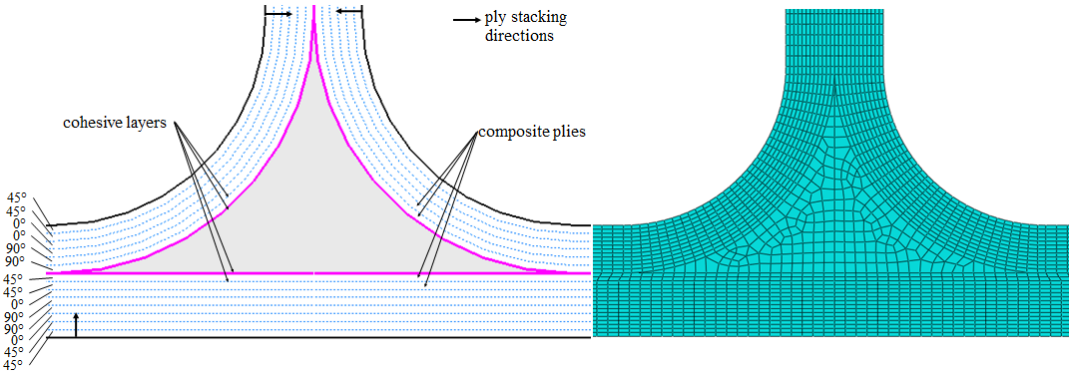

Figure 5.8- T-joint FE model

Material directions for composite and filler materials are presented in Figure 5.9 in Abaqus designation. For the composite sections, 1st direction is the fiber direction and the 2nd direction is the through the thickness direction. Cylindrical coordinate systems are applied on both sides of the filler section to get a similar stress distribution with the stringers at the curved region. The mesh stacking direction of the cohesive elements represents the Mode I opening direction

that should be in the 2nd direction of the composite sections. Material directions designate also the stress component directions which are used in the post process of the results. In Figure 5.9, a coordinate system is also shown at the midpoint of the skin which is used to locate crack positions in the post process.

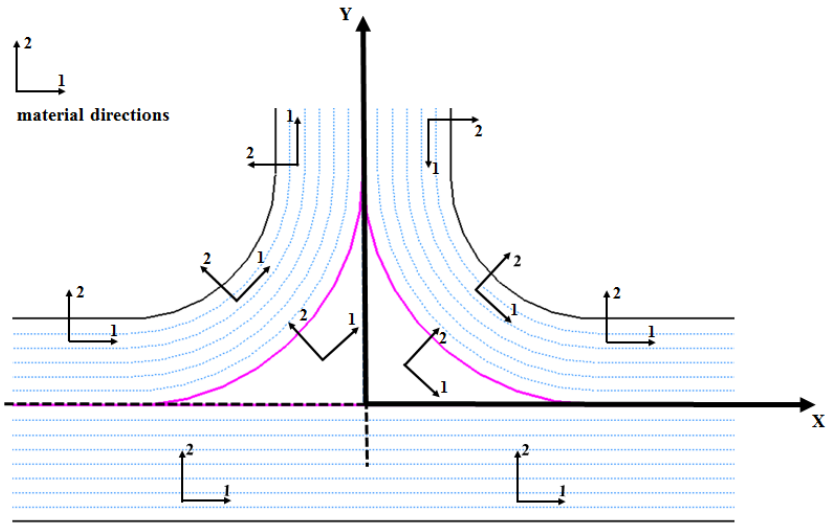

Figure 5.9- T-joint FE model material and stress component directions

5.2.2 Numerical Study of the T-joint

Numerical investigations of the T-joint are conducted in three parts:

- In the first part, delamination/debond process is investigated under 0^0, 45^0 and 90^0 pull loads to see the T-joint behavior under various loading conditions.
- In the second part, two FE models with and without cohesive layers are compared for 0^0 pull load. The load-displacement curve, stress fileds and delamination/debond behavior of the T-joint with cohesive layers are then investigated in detail for 0^0 pull load.
- In the third part, we concentrate on the 4 major delamination/debond initiation mechanisms mentioned in Section 5.1. We try to capture the initial failure modes by changing geometrical and material parameters of the T-joint and observe the delamination/debond behavior. A summary table is provided at the at the of the chapter for ease of following.

5.2.2.1 Angle Pull Loads

Angle pull loads at 0^o, 45^o and 90^o are used to characterize the delamination/debond behaviour of the T-joint. Figure 5.10 shows the loading and boundary conditions for angle pull loads. The skin panel is clamped at both ends and the load is applied at the top edge of the stringer in desired angle with respect to the vertical direction.

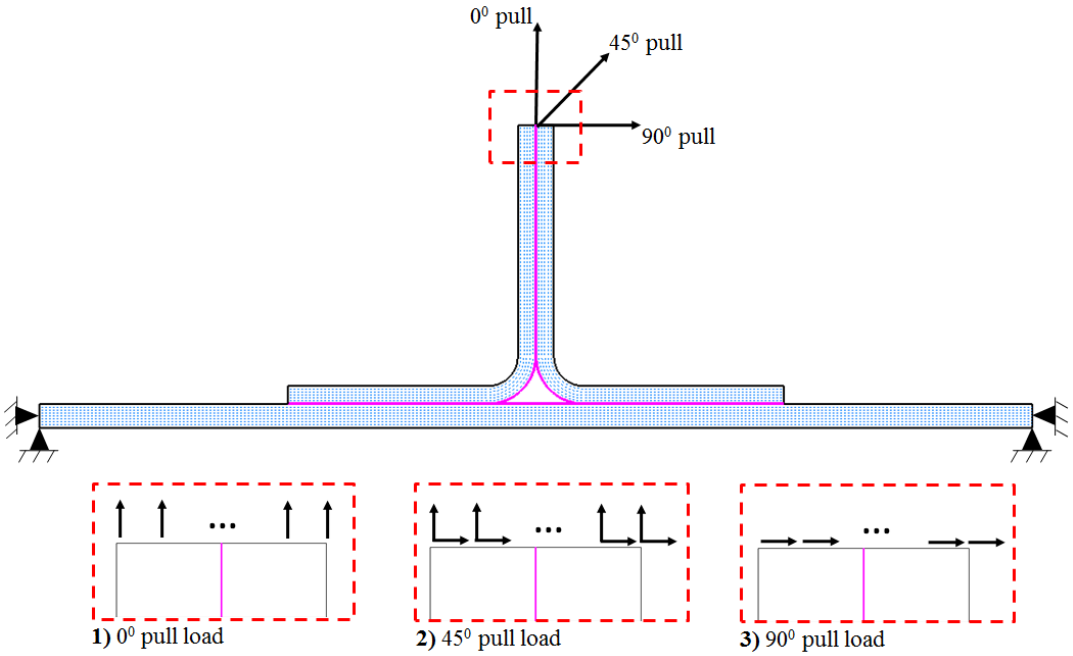

Figure 5.10- T-joint boundary conditions for 1) 0^o pull load, 2) 45^o pull load, 3) 90^0 pull load

Load-displacement curves for 0^o, 45^o and 90^o pull loads can be seen in Figure 5.11. The corresponding delamination/debond initiation and propagation scenarios are shown in Figures 5.12, 5.13 and 5.14.

For 0^o pull load case, a debond starts at the filler/right stringer leg interface at 6.91 mm displacement with an initial load drop. The debond then grows in upper and lower directions as shown in Figure 5.12. Lower crack front stops at the right filler corner, but the upper crack grows through the interface of stringers in a stabilized manner. At some point, a secondary debond is formed at the filler/left stringer interface at 8.08 mm displacement near the maximum load point. Both debonds grow in upper and lower directions suddenly and as the stringers starts to separate from the skin, delaminations are seen at the 7^{th} and 8^{th} skin ply interface at

both sides of the filler corners. As displacement increase further, delaminations and debonds grow through the stringer flange tips. These delaminations stabilize the load drop until the complete stringer-skin separation takes place. Detailed explanations of the delamination/debond initiation and propagation scenarios for the 0^o load case are given in the next section.

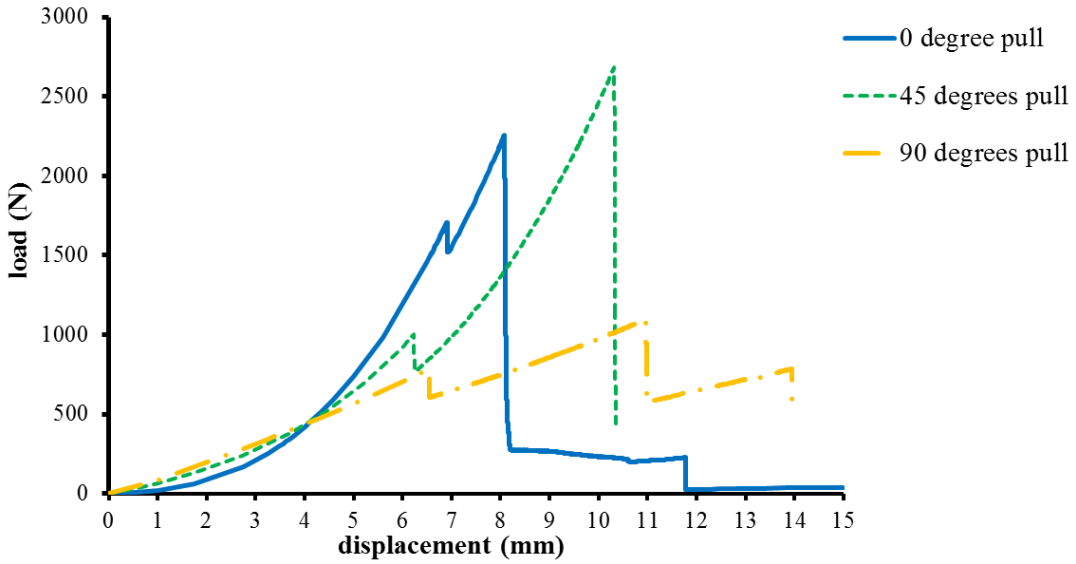

Figure 5.11- load-displacement curves for 0°, 45° and 90° pull loads

For 45^o pull load case, an initial debond appears in the filler/left stringer interface at 6.23 mm just after the initial drop in the load-displacement curve as shown in Figure 5.13. The debond stops growing after the initial sudden growth leading an increase in the carried load until 2685.6 N maximum load at 10.32 mm displacement. After the maximum load drop, a series of debonds and delaminations lead to a sudden collapse of the structure. After the initiation of a debond at the filler/right stringer interface and complete debond of the filler from the right stringer, delamination between the 5^{th} and 6^{th} right stringer plies, delamination between the 7^{th} and 8^{th} skin plies near the right filler corner, delamination between the 5^{th} and 6^{th} right stringer plies near the vertical midpoint of the right stringer, delamination between the 6^{th} and 7^{th} skin plies near the right filler corner and a delamination between the 7^{th} and 8^{th} skin plies at the left hand side near the flange end are seen, respectively.

For 90^o pull load case, a first debond appears at the filler/left stringer leg interface at 6.53 mm displacement and after a short time a delamination appears

between the 5^{th} and 6^{th} left stringer plies at 6.54 mm as shown in Figure 5.14. Then this delamination/debond pair grow together in lower and upper directions slowly leading a load increase up to maximum 1096.1 N at 10.96 mm displacement. Near this point, other debonds appear at the filler/right stringer leg interface and stringer/skin/filler intersection, leading a higher load drop in the load-displacement curve. After the sudden load drop, the load-displacement curve again stabilizes showing a stable crack growth with an increase in load. Final failure is observed at 13.93 mm displacement which is the complete debond of the skin form the left stringer leg.

Numerical results for the 0°, 45° and 90° pull loads show that failure initiation and propagation scenarios are different for each load case. Additionally, multiple cohesive layers should be inserted in the structure to get the multiple delamination/debond behavior.

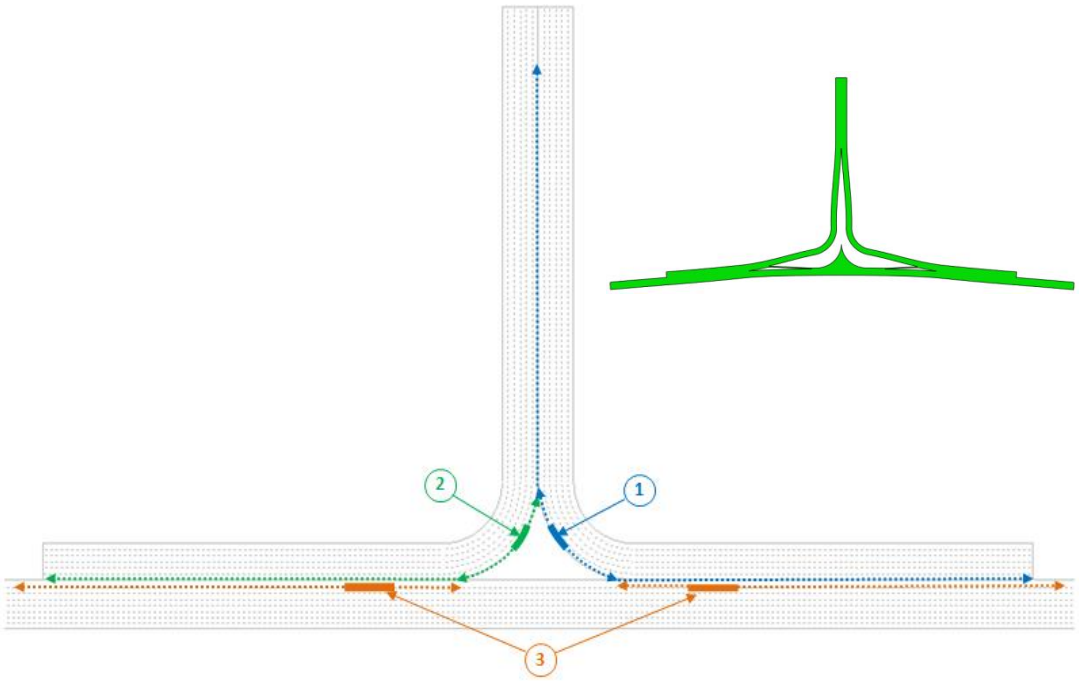

Figure 5.12- Delamination/debond initiation and propagation for 0° pull load

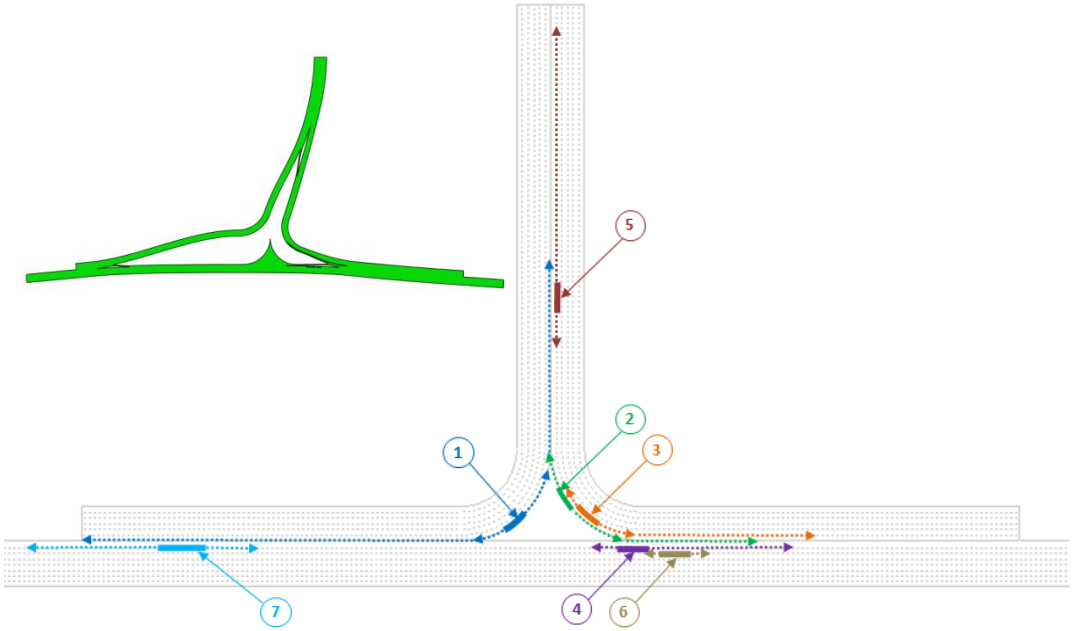

Figure 5.13- Delamination/debond initiation and propagation for 45° pull load

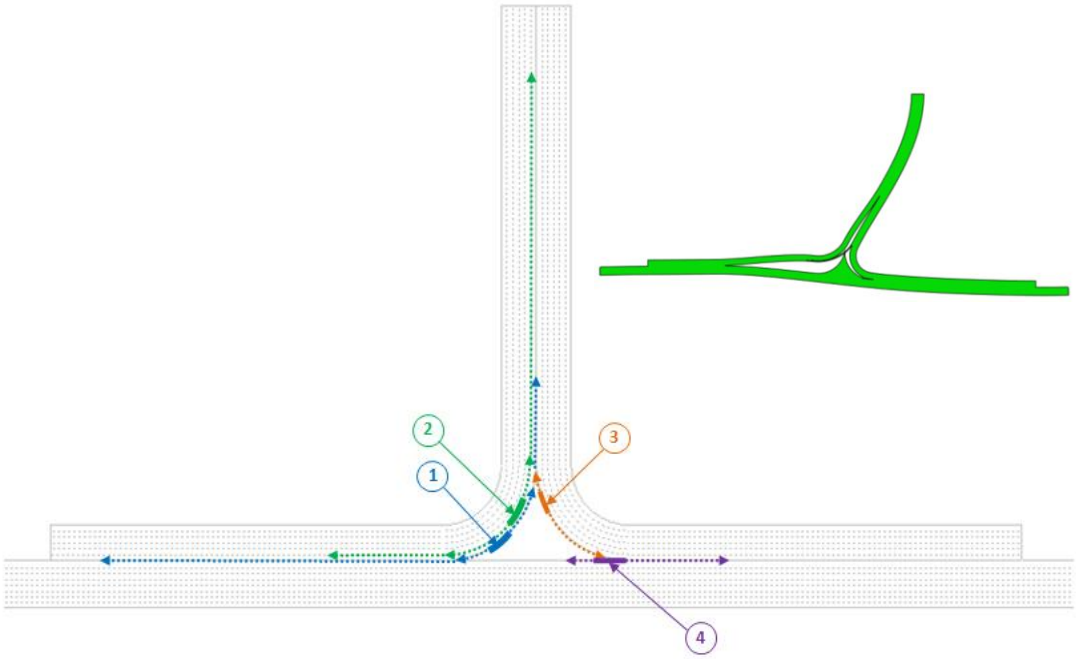

Figure 5.14- Delamination/debond initiation and propagation for 90° pull load

5.2.2.2 Cohesive vs Non-Cohesive Model For 0^0 Pull Load

The load–displacement curves for models with and without cohesive layers are shown in Figure 5.15 for the 0^0 pull load. The dashed line shows the elastic behavior with no cohesive layers. The solid line, with cohesive layers, follows the elastic curve until the initial failure at a displacement of 6.91 mm. It can be seen that the elastic stiffness of the two models are almost the same until the crack initiates. This shows that the inclusion of the cohesive elements does not influence the elastic behavior of the structure before the initiation. However, a slight difference in the load-displacement curve is observed which is caused by the damage accumulation in the cohesive elements. The S22 and S12 stress fields are shown in Figure 5.16 (a) for non-cohesive model and Figure 5.16 (b) for cohesive model before failure (at pt1 in Figure 5.15) which are almost identical for the two models (1^{st} and 2^{nd} stress component directions are shown in Figure 5.9). The good agreements of the load-displacement curve and the stress contours before the failure initiation shows that the multiple cohesive layers are successfully implemented and do not affect the elastic behavior.

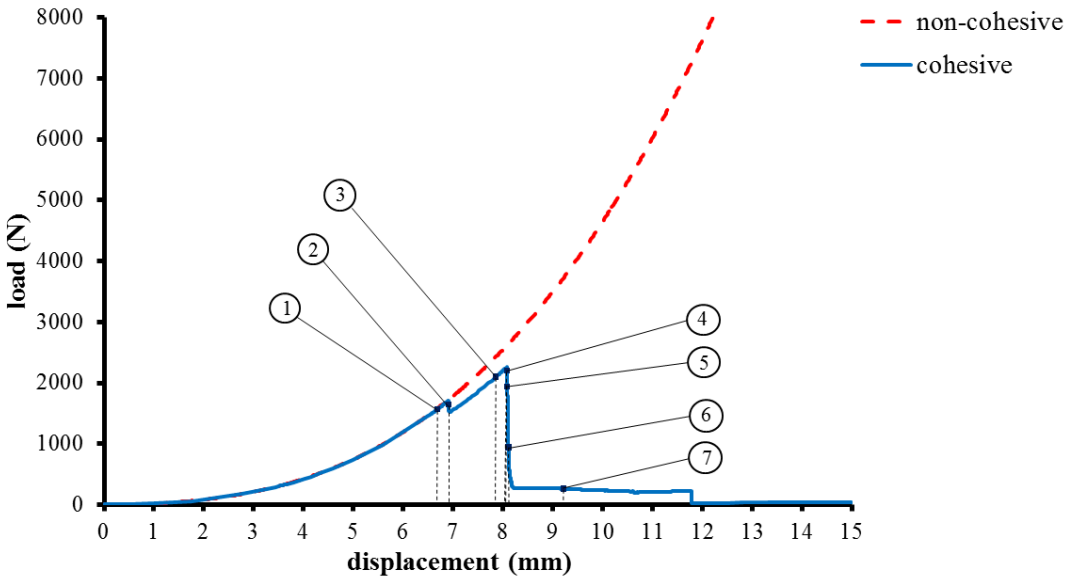

Figure 5.15- Load –displacement curves for cohesive and non-cohesive models for 0° pull load

As seen in Figure 5.16, at pt1 in Figure 5.15 which is close to the initial debond displacement, filler corners are the high stress locations for S22 component and filler/stringer interface at the radius are the high stress locations for S12 component. Maximum S22 stress value is around 60 MPa at the top filler corner where S12 is almost 0 MPa. Maximum S12 stress values are around 70 MPa at the left and right stringers at 57° from the horizontal axis where S22 is around 20 MPa. Debond initiates at 78° from the horizontal axis as explained in the next chapter. At the debond location, S22 is around 45 MPa and S12 is around 45 MPa which shows the mixed-mode delamination initiation.

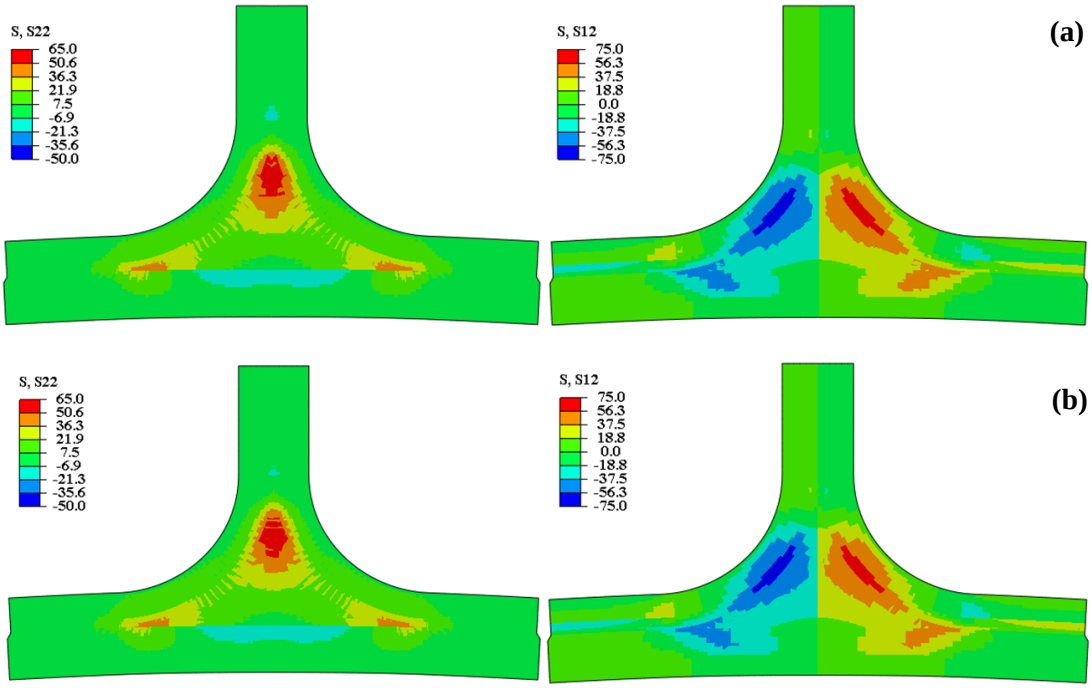

Figure 5.16- S22 and S12 stress components captured at pt1 in Figure 5.15 a) non-cohesive model (displacement = 6.60 mm, load=1529N) b) cohesive model (displacement = 6.60 mm, load=1517N)

Delamination/debond process for cohesive model

S22 and S12 stress contour plots at the delamination/debond initiation and during the propagation process are shown in Figure 5.17 (a-f), at points 2, 3, 4, 5, 6, 7 (Figure 5.15), respectively. The S22 stress contours are shown on the left side of the figures and S12 stress contours are shown on right side of the figures.

Figure 5.17 (a) shows the stress contours at pt2 (Figure 5.15) (6.91 mm displacement and 1675 N load). At the filler/right stringer interface in the curved region, an initial debond initiates with a length of 0.2 mm (one element size) at 78° from the horizontal axis and propagates unstably where the crack tips are shown by the arrows in Figure 5.17 (a). A small load drop is seen with the initial debond as shown in Figure 5.15 and a new stress fields are developed. Stress concentrations are developed in front of the crack tips. At the upper crack front, S22 is around 80 MPa and S12 is around 10 MPa indicating a Mode I dominated crack growth. At the lower crack front S22 is around 60 MPa and S12 is around 80 MPa indicating a mixed-mode crack growth.

Figure 5.17 (b) shows the stress contours at pt3 (Figure 5.15) (7.86 mm displacement and 2101 N load) where debond has propagated in the lower and upper directions on the bonding line. Upper crack front grows through the stringer/stringer interface to some displacement from the filler tip and stabilizes, because left stringer starts to act as main load carrying member and load on the right stringer is eliminated. Lower crack stops at the filler corner because of the compressive S22 stress component. Therefore, the stable behavior of the crack tips lead to an increase in the load-displacement curve from the local minimum of 1519 N with a decreased stiffness (Figure 5.15). Meantime, stress concentration at the filler/left stringer interface is still present. S22 stress component is around 50 MPa at the filler/left stringer interface at 62° from the horizontal axis and S12 component is around 45 MPa at the filler/left stringer interface at the 22° from the horizontal axis.

Figure 5.17 (c) shows the stress contours at pt4 (Figure 5.15) (8.08 mm displacement and 2233 N load), near the maximum load point of 2256 N at the end of the stable crack growth, just before the next load drop. At pt4, a second debond initiates at the filler/left stringer at 67° from the horizontal axis. A sudden load drop is seen after the debond initiates. As in the right debond, the upper crack grows under Mode I dominated loading (S22=100 MPa, S12=10 MPa) and lower crack grows under mixed-mode loading (S22=80 MPa, S12=70 MPa).

Figure 5.17 (d) shows the stress contours at pt5 (Figure 5.15) (8.08 mm displacement and 2127 N load). After the initiation, debond at the filler/left stringer interface rapidly grows in upper and lower directions and filler completely

separates from the stringer. Stress concentrations are seen at the front of the rapidly growing crack tips with maximum S22 and S12 stress values with 135 MPa and 174 MPa, respectively. Until the separation of the filler from the stringers, the lower crack tip at the filler/right stringer interface does not propagate.

Figure 5.17 (e) shows the stress contours at the continuation of the load drop at pt6 (Figure 5.15) (8.11 mm displacement and 796 N load). After separation of the filler from the left stringer, debonds grow together through the skin/stringer interfaces. During the rapid debond growth; delaminations appear between the upper 45° plies of the skin at left and right sides of the filler at -5.89 mm and 7.88 mm, respectively. After delamination initiation, lower crack tips of debonds and delaminations continue to grow through the stringer flange tips. Stress concentrations can be observed at all of the crack tip and at the same time decreasing stress values around the curved region of the structure.

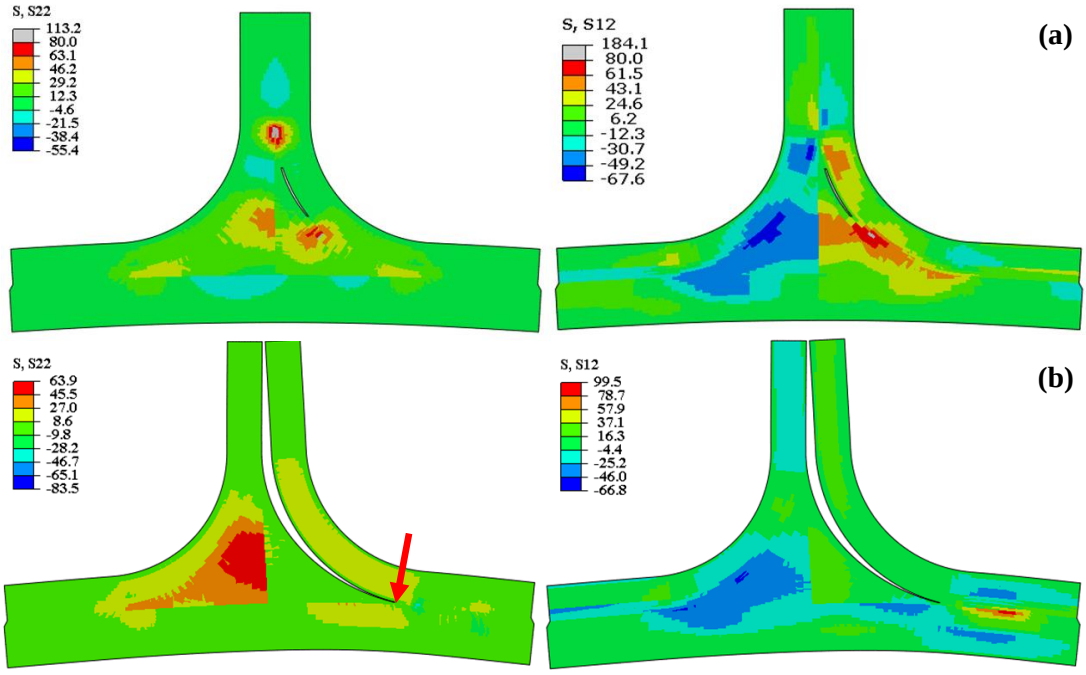

Figure 5.17- S22 and S12 stress components captured at critical points on the load-displacement curve of the cohesive model a) pt2 (displacement = 6.91 mm, load=1675 N), b) pt3 (displacement = 7.86 mm, load=2101 N)

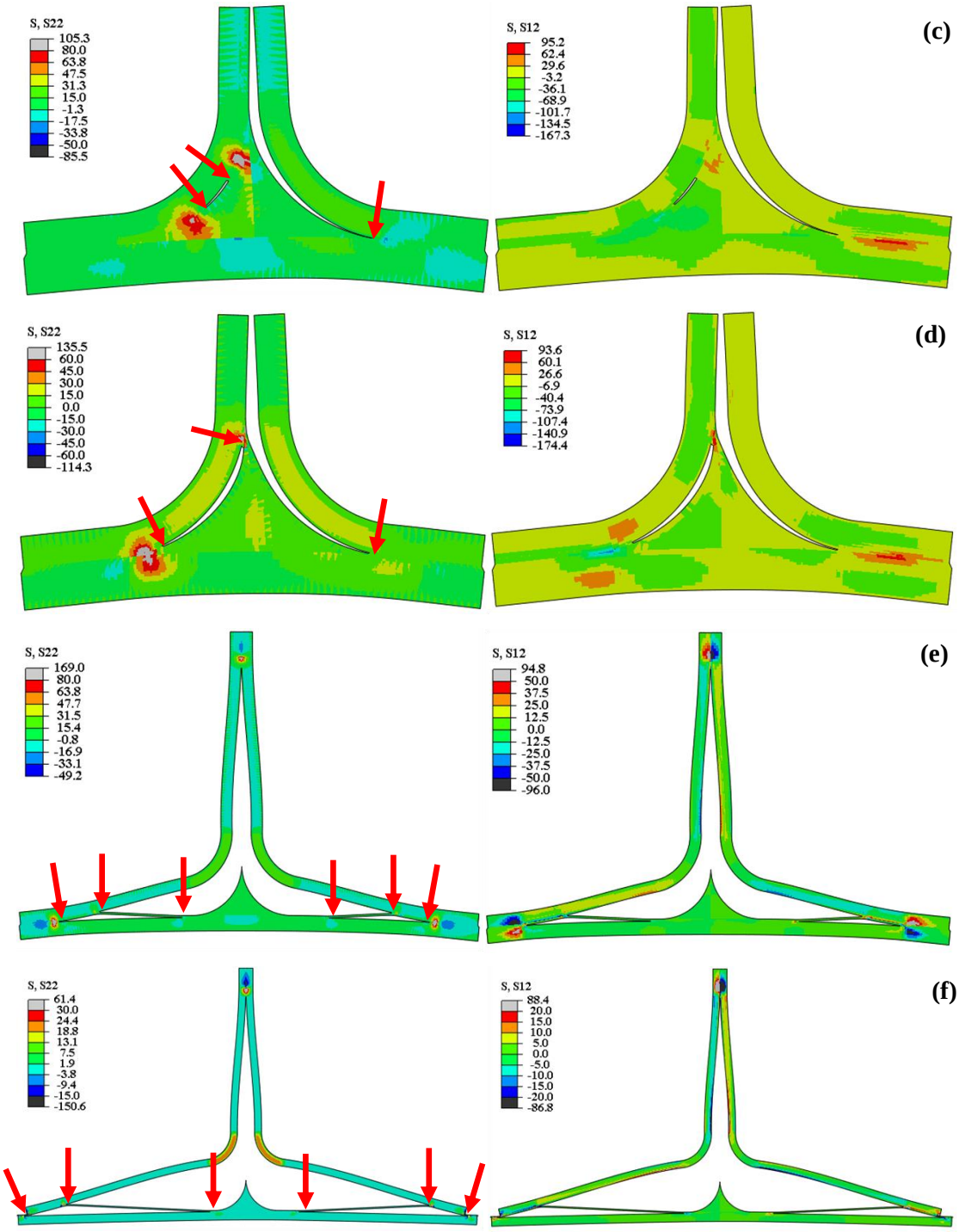

Figure 5.17 contd- S22 and S12 stress components captured at critical points on load-displacement curve of the cohesive model, c) pt4 (displacement = 8.08 mm, load=2233 N), d) pt5 (displacement = 8.08 mm, load= 2127 N), e) pt6 (displacement = 8.11 mm, load=796 N), f) pt7 (displacement = 9.11 mm, load=262 N)

During debond/delaminations which occur in a single load drop, unstable crack growth leads to skin/stiffener debonding and delamination between skin plies. Unstable crack growth continues until the delaminations between the skin plies stop under the stringer flange tips. After this point, debonds grow in a stable manner. Figure 5.17 (f) shows the stress contours at pt7 on the stable region of the load-displacement curve (Figure 5.15) (9.11 mm displacement and 262 N load, ≈ 10% of the maximum load). Final failure of the structure occurs with the complete separation of stringers from the skin.

From the above discussion, it can be stated that filler area is critical in terms of delamination/debond initiation and propagation. Stress concentrations around this region cause the initial cracks. Delamination/debond initiation and propagation generally show a mixed-mode behavior. High stress concentrations at the crack tips cause the further propagation. Filler/stringer separation causes a significant load drop which shows the importance of the filler for the structural integrity. T-joint almost fails during the sudden load drop. At the later stages of the process, delaminations are seen between the upper skin plies which stabilize the cracks and cause a residual strength. This shows the importance of modeling cohesive layers for the complete interface length.

Numerical issues

Effect of Mesh Refinement: To see the effects of a finer mesh on the cohesive model results, current FE model is modified: 0.1mm element size and 3 elements per ply are used for the composite skin and stringers; 0.1 mm element size is used for filler and cohesive layers. Other properties of the FE model are kept constant. The result shows that, during debonding of the upper filler corner from the left stringer, convergence problems arise even for very small step increments. The elements in the upper filler corner distorts significantly and the very rapid increase in debond is not captured. With the help of some trial runs, it is seen that when coarser mesh is used for the filler section, stress and displacement fields are averaged within bigger elements and convergence problem is resolved.

A new FE model for fine mesh is created with a different assembly concept to overcome this convergence problem. Within this model, the four parts of the

structure and bonding lines are generated individually and assembled together with tie elements. This model allows different mesh densities for different parts as seen in Figure 5.18. 0.1 mm element size and 3 elements per ply are used for stingers and skin, 0.05mm element size is used for debond line and 0.2 mm element size is used for filler. By using coarse elements for the filler, solution is achieved with no convergence problem. Figure 5.19 shows the coarse mesh and fine mesh model load-displacement curves which are almost the same. The delamination/debond behavior and the stress fields for the fine mesh model is also same with the coarse model as seen in Figure 5.20. Disadvantage of the new fine mesh model is the long computation time. Therefore, the coarse mesh model with 0.2 mm element size is considered as safe for further investigations.

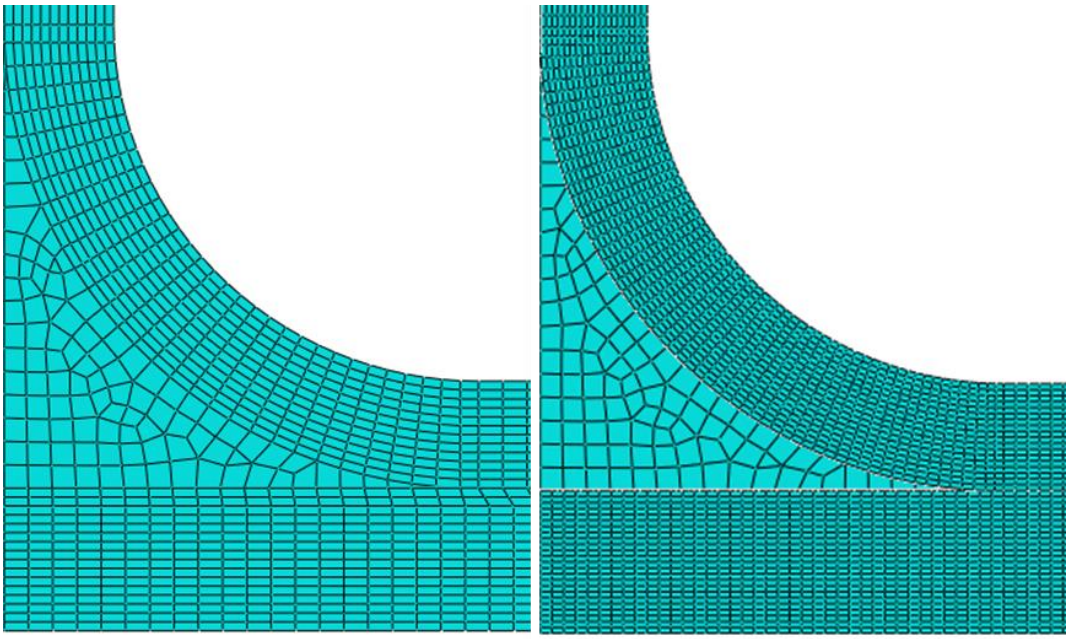

Figure 5.18- Coarse vs fine mesh cohesive models

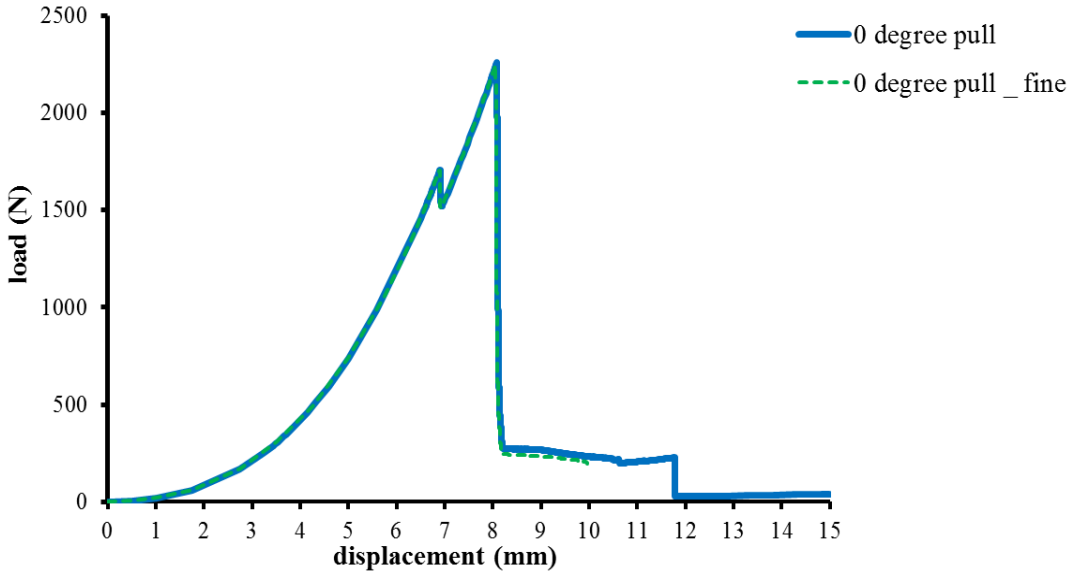

Figure 5.19- Load –displacement curves for the coarse and the fine mesh cohesive models for 0^0 pull load

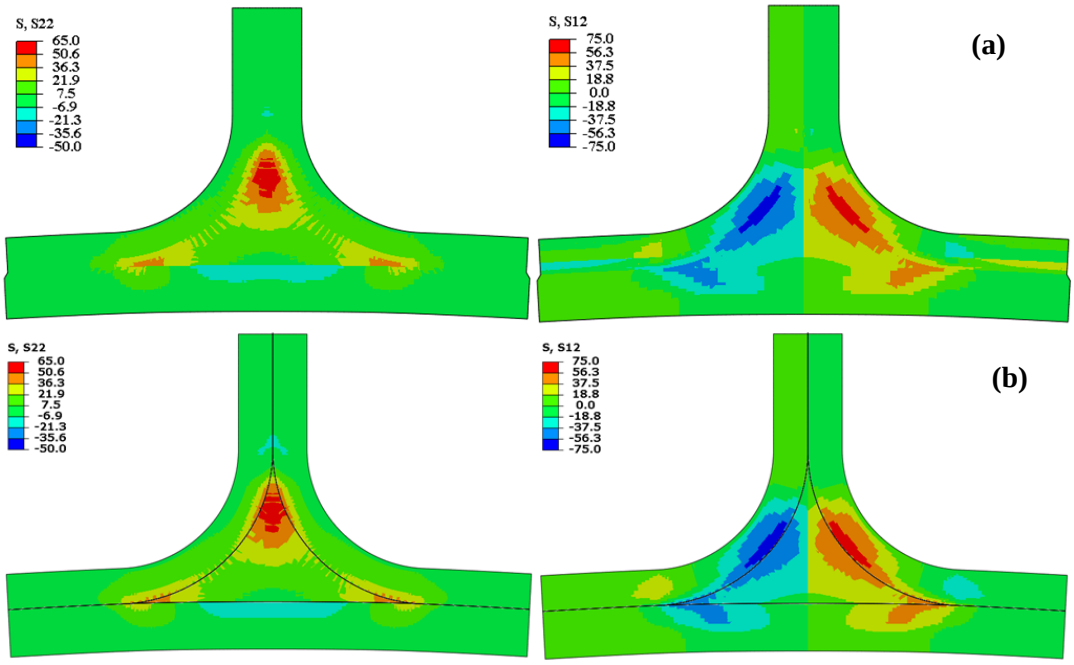

Figure 5.20- S22 and S12 stress components captured at pt1 in Figure 5.15 a) coarse mesh cohesive model (displacement = 6.60 mm, load=1517N), b) fine mesh cohesive model (displacement = 6.60 mm, load=1525N)

5.2.2.3 Failure Modes For 0^0 Pull Load

In this part of the T-joint study, a parametric study is conducted by varying geometrical and material properties to capture the failure mechanisms which are presented in Section 5.1. Load-displacement curves and delamination/debond behaviors are compared with the current FE model (base model) for 0° pull load.

5.2.2.3.1 Failure Mechanism 1 – Debond at the filler/stringer interfaces

The first failure mechanism is the debond of the filler/stringer interfaces as shown in Figure 5.1. The considered T-joint in Section 5.2.2.2 shows the first failure mechanism; therefore further study mainly focuses on capturing the other three failure mechanisms.

5.2.2.3.2 Failure Mechanism 2 – Delamination between the stringer plies

The second failure mechanism is the delamination between the stringer plies as shown in Figure 5.2. Five different approaches are investigated to capture the second failure mechanism; (a) changing the ply sequence of the stringers, (b) increasing the fracture toughness values (G_{IC} and G_{IIC}) of the FM300 adhesive material, (c) increasing the interface strength values ($t_I^0$and t_{II}^0) of the FM300 adhesive material, (d) decreasing the fracture toughness values (G_{IC} and G_{IIC}) of the IM7/8552 composite material and (e) decreasing the interface strength values ($t_I^0$and t_{II}^0) of the IM7/8552 composite material.

a-) 1st approach:

The placement of the 0^0 and 90^0 plies of the stringers are interchanged to change the failure mechanism to delamination between the stringer plies. The original layup of the base model is [45/45/0/0/90/90] (layup A) whereas the modified layup is [45/45/90/90/0/0] (layup B).

Load-displacement curves for the layup A and the layup B are shown in Figure 5.21. Although, the load-displacement behaviors of the layups show similar features, first and second load drop points decrease for the layup B. First load drop

point reduces to 1428 N from 1706 N and second load at maximum load reduces to 2001 N from 2256 N. Towards the end of the load-displacement curve, crack growth stabilizes with almost zero stiffness for both layups, but residual strength remains longer for layup B. Some critical points (pt1 – pt7) are shown on the load-displacement curve of the layup B which are used to discuss the delamination/debond initiation (Figure 5.22) and propagation process (Figure 5.23) in detail.

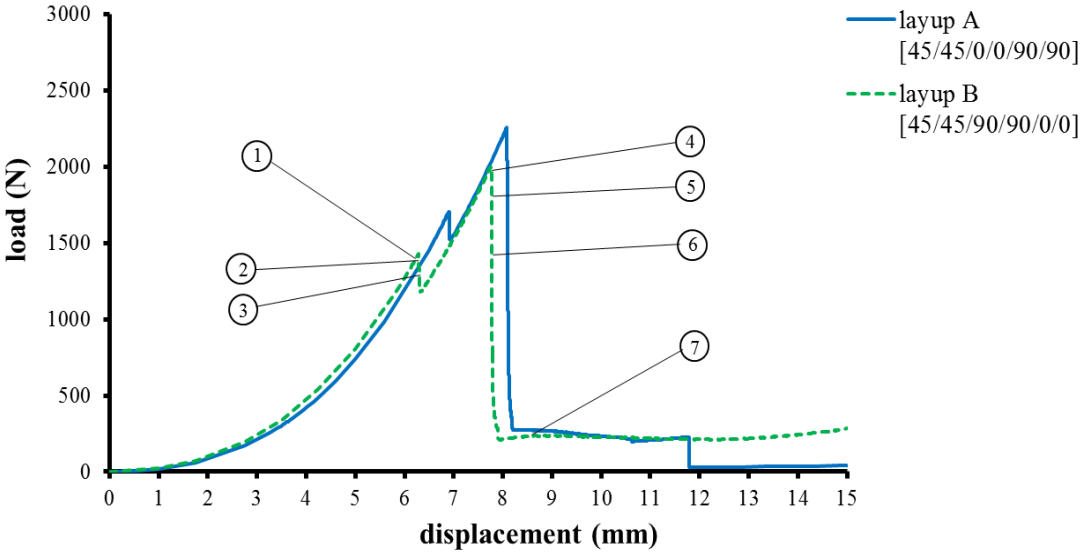

Figure 5.21- Load–displacement curves for the layup A and the layup B for 0^0 pull load

S22 and S12 stress contours for the modified layup are shown at the points 1, 2 and 3 (Figure 5.21) in Figure 5.22 corresponding to the delamination initiation process. An initial debond is seen between the filler/right stringer interface at 78° from the horizontal axis. Before the failure at the initial debond location (filler/right stringer interface) (at pt1 displacement = 6.27 mm, load=1423 N), S22 is around 40 MPa and S12 is around 40 MPa as seen in Figure 5.22 (a) indicating that failure initiates in mixed-mode. Figure 5.22 (b) shows that an initial debond is seen between the filler/right stringer interface (at pt2 with 6.29 mm displacement and 1415 N load) (1^{st} failure mechanism) at 78° from the horizontal axis which is almost the same with the base model. Additionally, a delamination is seen between the 5^{th} and 6^{th} right stringer plies near the filler corner (2^{nd} failure mechanism) as the debond approaches the filler corner (at pt3 with 6.30 mm displacement and

1287 N load) as shown in Figure 5.22 (c). The initial debond and delamination cause the first load drop on the load-displacement curve in Figure 5.21.

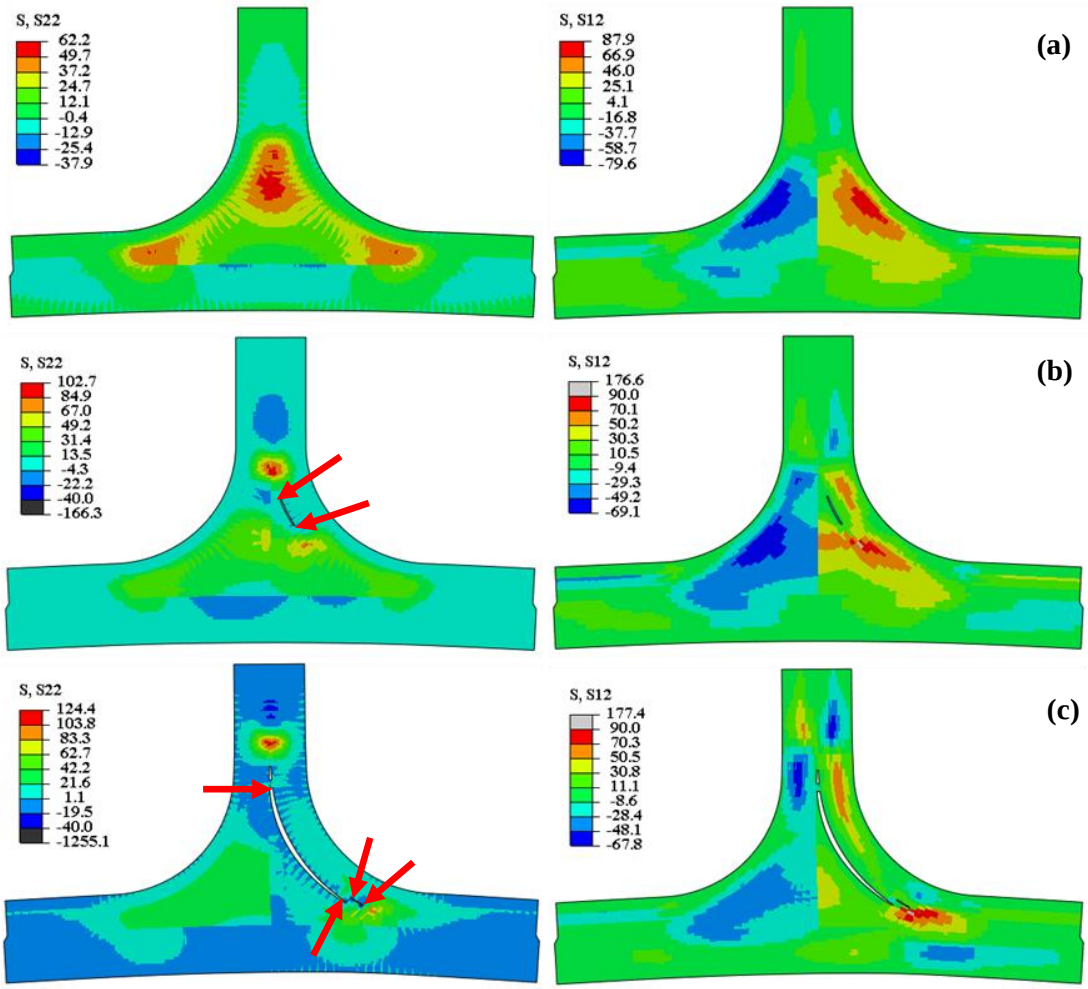

Figure 5.22- S22 and S12 stress components captured at the initial delamination point for the layup B a) pt1 (displacement = 6.27 mm, load=1423 N), b) pt2 (displacement = 6.29 mm, load=1415 N), c) pt3 (displacement = 6.30 mm, load=1287 N)

Delamination initiation/propagation scenario for the modified layup is shown in Figure 5.23 through the points 2, 3, 4, 5, 6 and 7 (Figure 5.21). Figures 5.23 (a) and (b) correspond to the initial debond and delamination points which are discussed in the above paragraphs. After the initial failures, lower crack tip of the debond propagates until the right filler corner and stops. Upper crack tip of the debond stops 1.4 mm above the upper filler corner. Delamination between the stringer plies propagates only in the flange direction. Therefore, load starts to

increase after the initial drop. As displacement is increased, a series of debonds and delaminations are observed after the maximum load point is reached (7.76 mm displacement and 2001 N load). A debond appears at the filler/left stringer interface (at pt4 with 7.76 mm displacement and 1984 N load) at 55° from the horizontal as seen in Figure 5.23 (c). A delamination appears between the 5^{th} and 6^{th} plies of the left stringer (at pt5 with 7.77 mm displacement and 1851 N load) near the left filler corner as seen in Figure 5.23 (d). Another delamination appears between the 4^{th} and 5^{th} plies of the left stinger (at pt6 with 7.77 mm displacement and 1486 N load) just to the left of the left filler corner as seen in Figure 5.23 (e). Both debond and delaminations are observed during the sudden load drop on the load-displacement curve in Figure 5.21. As displacement increase further, failure stabilizes after the crack between 4^{th} and 5^{th} plies of the left stinger reaches the flange tip as seen in Figure 5.23 (f).

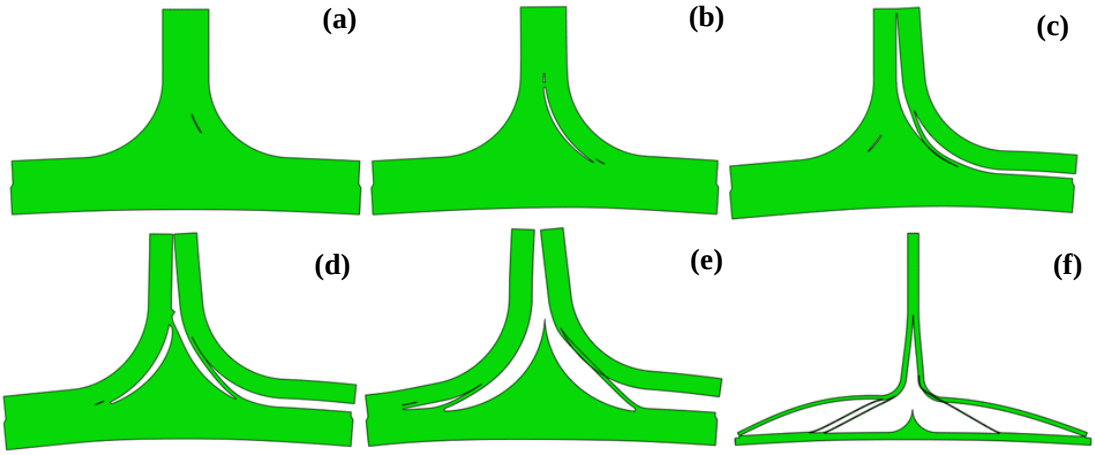

Figure 5.23- Delamination/debond propagation for the layup B a) pt2 (displacement = 6.29 mm, load=1415 N), b) pt3 (displacement = 6.30 mm, load=1287 N), c) pt4 (displacement = 7.76 mm, load=1984 N), d) pt5 (displacement = 7.77 mm, load=1851 N), e) pt6 (displacement = 7.77 mm, load=1486 N), f) pt7 (displacement = 8.43 mm, load=230 N)

In summary, interchanging 0° and 90° stringer plies reduces the first and second failure loads because of the delaminations between the stringer plies in addition to the debond between filler/stringer interfaces. Towards the end of the failure process, although residual strengths are approximately the same, layup B

carries the load for longer displacement. Delaminations of the upper skin plies are replaced by the delamination of the 4th and 5th plies of the left stinger. Therefore, failure initiation and propagation scenario is changed by changing the layup. One of the two layup configurations should be chosen according to design needs considering the advantages and disadvantages.

b-) 2nd approach:

The fracture toughness values (G_{IC} and G_{IIC}) of the FM300 adhesive material for Modes I and II are increased to 800% to change the failure mechanism to the delamination between the stringer plies.

Load-displacement curves for the base model and the increased fracture toughness are shown in Figure 5.24. For the increased toughness, the area under the load-displacement curve, failure initiation load and maximum load increase in considerable amounts. There are three load drops on the curve. First load drop point is at 2730 N, second load drop is at 4728 N and last drop is at 4968 N which is the maximum load point. Sudden load drop after the maximum load causes convergence problems for the increased toughness, therefore load–displacement and failure propagation cannot be captured for further loading. Some critical points (pt1 – pt4) are shown on the load-displacement curve of the increased toughness which will be used to discuss the delamination/debond initiation (Figure 5.25) and propagation process (Figure 5.26) in detail.

S22 and S12 stress contours for the increased toughness are shown in Figure 5.25 at the points 1 and 2 (Figure 5.24) corresponding to the delamination initiation process. Figure 5.25 (a) shows that, before the crack initiation (at pt1 with 8.09 mm displacement and 2583 N load), there are S22 stress concentrations at the filler corners and there are S12 stress concentrations around the filler/stringer interfaces at 48° from the horizontal. Before the failure, at the initial failure location, S22 is around 30 MPa and S12 is around 80 MPa indicating the failure initiates in mixed-mode. Figure 5.25 (b) shows that an initial delamination with 0.60 mm length (3 element size) is seen between 5th and 6th left stringer plies (at pt2 with 8.27 mm displacement and 2721 N load) at 60° from the horizontal axis.

The initial delamination causes a small load drop on the load-displacement curve in Figure 5.24.

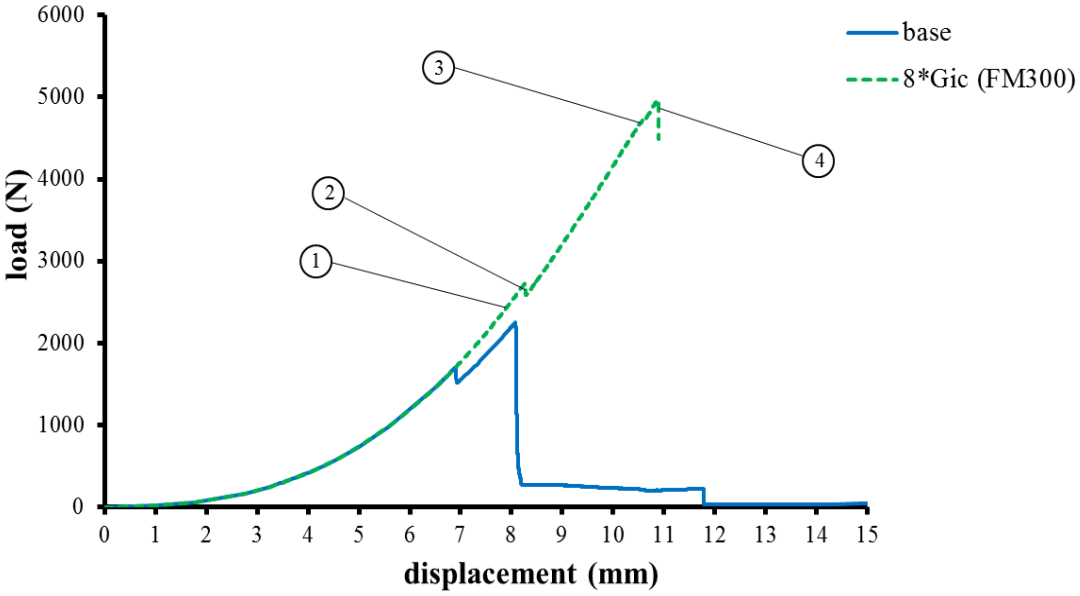

Figure 5.24- Load–displacement curves for the base and the increased fracture of the FM300 adhesive material for 0^0 pull load

Delamination initiation/propagation scenario for the increased toughness is shown in Figure 5.26 through the points 2, 3 and 4 (Figure 5.24). Figures 5.26 (a) corresponds to the initial delamination point which is discussed in the above paragraph. After the initial failure, delamination grows in upper and lower directions suddenly. With the increasing displacement, upper crack front slows after 3.33 mm above the upper filler corner and lower crack front slows after 5.52 mm from the left filler corner. As displacement is increased further, a debond initiates at the filler/right stringer interface (at pt3 with 10.63 mm displacement and 4728 N load) as shown in Figure 5.26 (b). This debond causes a negligible load drop (Figure 5.24) because of the high fracture toughness of the adhesive material which slows down the crack propagation. Load increases until another debond initiates at the filler/left stringer interface (pt4 with 10.89 mm displacement and 4856 N load) as shown in Figure 5.26 (c) after the maximum load point (10.88 mm displacement and 4968 N load). After the debond initiation at the filler/left stringer interface, a sudden load drop is observed (Figure 5.24) which causes numerical convergence problems.

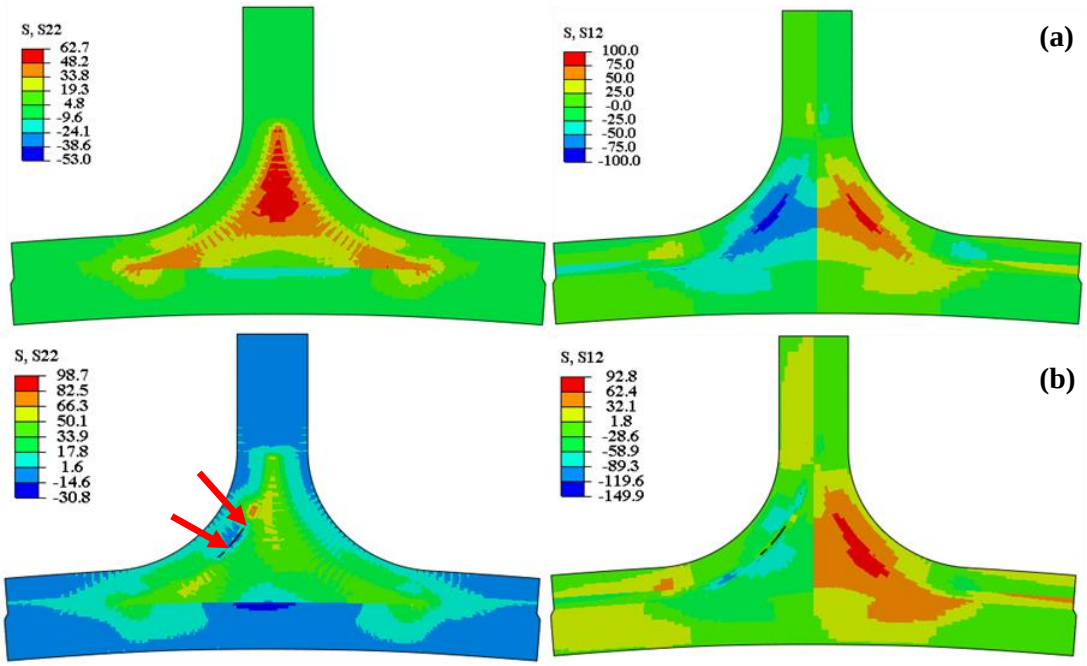

Figure 5.25- S22 and S12 stress components captured at initial delamination points of the increased fracture toughness of the FM300 adhesive material a) pt1 (displacement = 8.09 mm, load=2583 N), b) pt2 (displacement = 8.27 mm, load = 2721 N)

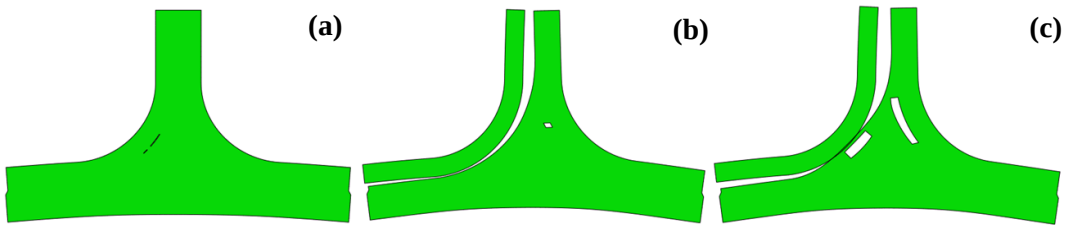

Figure 5.26- Delamination/debond propagation for the increased fracture toughness of the FM300 adhesive material a) pt2 (displacement = 8.27 mm, load = 2721 N), b) pt3 (displacement = 10.63 mm, load = 4728 N), c) pt4 (displacement = 10.89 mm, load = 4856 N)

In summary, the area under the load displacement curve, initial failure load and displacement, maximum failure load and displacement increase by huge amounts for the increased toughness values compared to the base model. Initial failure is observed between the stringer plies in contrast to the debond initiation in the base model. Although delamination between the stringer plies (2^{nd} failure mechanism) is captured, 800% increase in fracture toughness values is hard to

achieve. But, Z pins or some other crack arresting mechanism can be used to increase the area under the load displacement curve and the maximum failure load which can be considered as fracture toughness increase.

c-) 3rd approach:

The interface strength values (t_I^0 and t_{II}^0) of the FM300 adhesive material for Modes I and II are increased to 130% to change the failure mechanism to delamination between the stringer plies.

Load-displacement curves for the base model and the increased fracture toughness are shown in Figure 5.27. For the increased strength, the area under the load-displacement curve, failure initiation load and maximum load increase in considerable amounts. There are four load drops on the curve indicating the gradual failure of the structure. First load drop point is at 2241 N, second load drop is at 3034 N, third load drop is at 4085 N and last drop is at 5504 N which is the maximum load point. Sudden load drop after the maximum load causes convergence problems for the increased strength, therefore load–displacement and failure propagation cannot be captured for further loading. Some critical points (pt1 – pt7) are shown on the load-displacement curve of the increased strength which will be used to discuss the delamination/debond initiation (Figure 5.28) and propagation process (Figure 5.29) in detail.

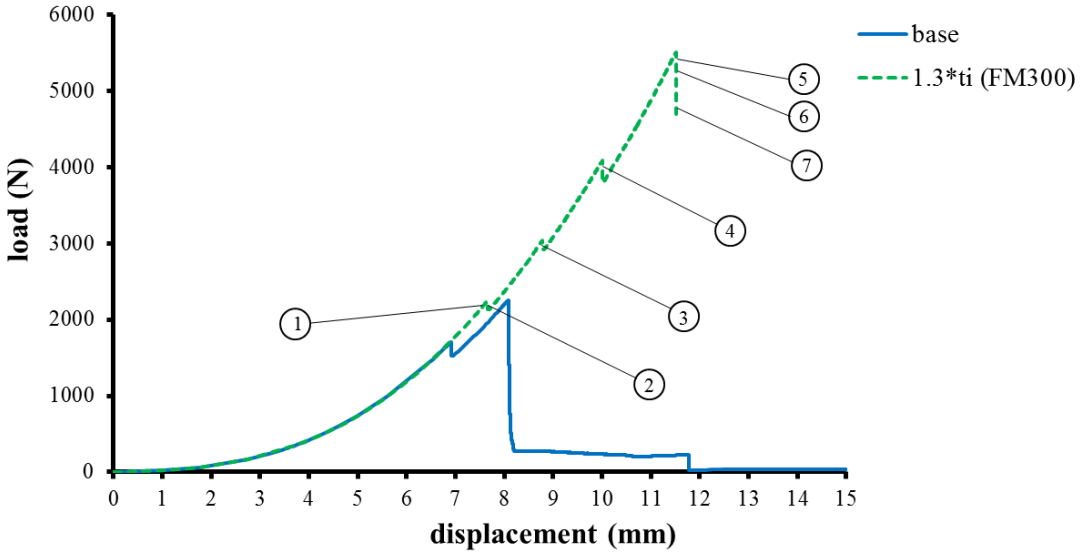

Figure 5.27- Load–displacement curves for the base and the increased interface strength of the FM300 adhesive material for 0^0 pull load

S22 and S12 stress contours for the increased interface strength are shown in Figure 5.28 at the points 1 and 2 (Figure 5.27) corresponding to the delamination initiation process. Figure 5.28 (a) shows that, before the crack initiation (at pt1 with 7.64 mm displacement and 2234 N load), there are S22 stress concentrations at the filler corners and there are S12 stress concentrations between the stringer plies at the curved region at 57° from the horizontal. At the initial debond location before the initiation, S22 is around 35 MPa and S12 is around 70 MPa indicating the failure initiates in mixed-mode. Figure 5.28 (b) shows that an initial delamination with 0.60 mm length (3 element size) is seen between 5th and 6th right stringer plies (at pt2 with 7.65 mm displacement and 2234 N load) at 72° from the horizontal axis. The initial delamination causes a small load drop on the load-displacement curve as seen in Figure 5.27.

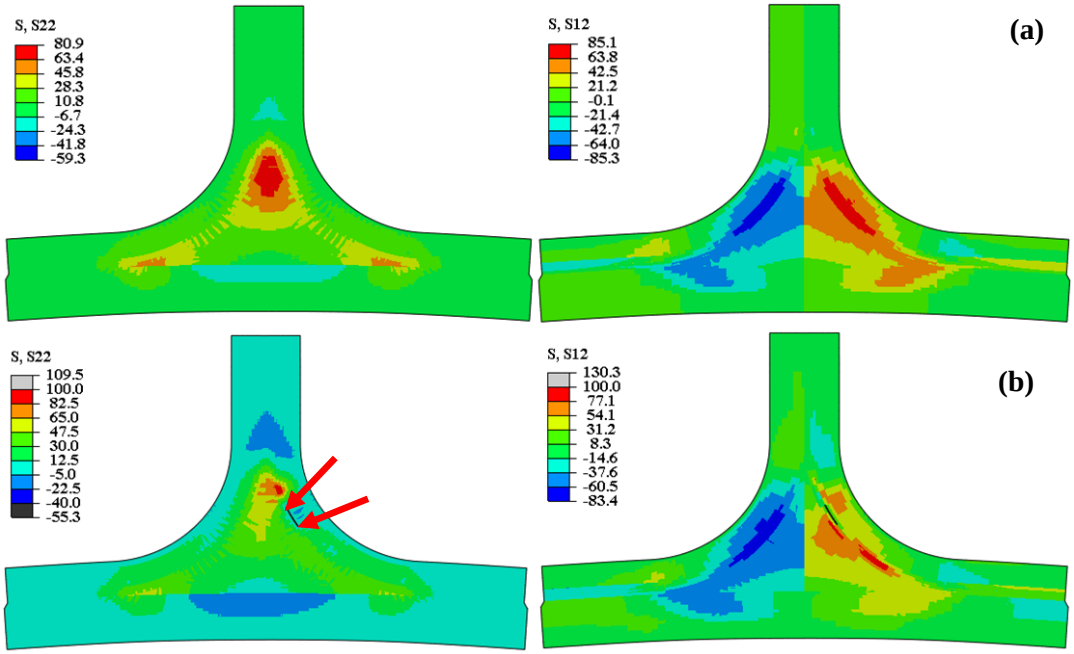

Figure 5.28- S22 and S12 stress components captured at the initial delamination point of the increased interface strength of the adhesive FM300 material a) pt1 (displacement =7.64 mm, load = 2234 N), b) pt2 (displacement =7.65 mm, load = 2234 N)

Delamination initiation/propagation scenario for the increased strength is shown in Figure 5.29 through the points 2, 3, 4, 5, 6 and 7 (Figure 5.27). Figures 5.29 (a) correspond to the initial delamination point which is discussed in the

above paragraph. After the initial failure, delamination grows in upper and lower directions suddenly. With the increasing displacement, upper crack front slows after 3.53 mm above the upper filler corner and lower crack front slows after 5.13 mm from the right filler corner. Therefore, load starts to increase after the initial drop. With the increase in displacement, another delamination is seen between 5^{th} and 6^{th} left stringer plies (at pt3 with 8.78 mm displacement and 3030 N load) as seen in Figure 5.29 (b). This delamination causes a load drop on the load-displacement curve (Figure 5.27). After the initial sudden growth, upper crack stops 2.54 mm above the upper filler corner and lower crack front slows after 6.52 mm from the left filler corner. Therefore, load starts to increase with the increase in displacement once again. A debond is seen in at the filler/right stringer interface (at pt4 with 10.01 mm displacement and 4077 N load) and a delamination is seen between the skin upper plies near the right filler corner as seen in Figure 5.29 (c). After the last delamination and debond, all the crack fronts stabilizes and load starts to increase until the maximum load point (11.51 mm displacement and 5504 N load). Near the maximum load point, a debond at the filler/left stringer interface (at pt5 with 11.51 mm displacement and 5493 N load) and a delamination between the upper skin plies near to the right filler corner (at pt6 with 11.51 mm displacement and 5396 N load) appear as shown in Figure 5.29 (d) and (e). Excessive delamination/debonds (at pt7 with 11.52 mm displacement and 4697 N load) are shown in Figure 5.29 (f) at the last step of the sudden load drop (Figure 5.27). Sudden load drop causes convergence problems, therefore load–displacement and failure propagation cannot be captured for further loading.

In summary, the area under the load-displacement curve, initial failure load and displacement, maximum failure load and displacement are increased by huge amounts for the increased interface strength values of the adhesive material compared to the base model. A 30% increase in interface strength results in more than 200% increase in maximum failure load. Failure initiation and propagation scenario is also changed. Delamination between the stringer plies are observed in addition to debonds at the filler/stringer interfaces and delaminations between the skin plies. A 30% increase in the interface strength and a 800% increase in fracture toughness give similar results. But, 30% increase in the strength seems to

be more achievable. Therefore, an adhesive material with higher interface strength may be the choice over the material with the increased toughness.

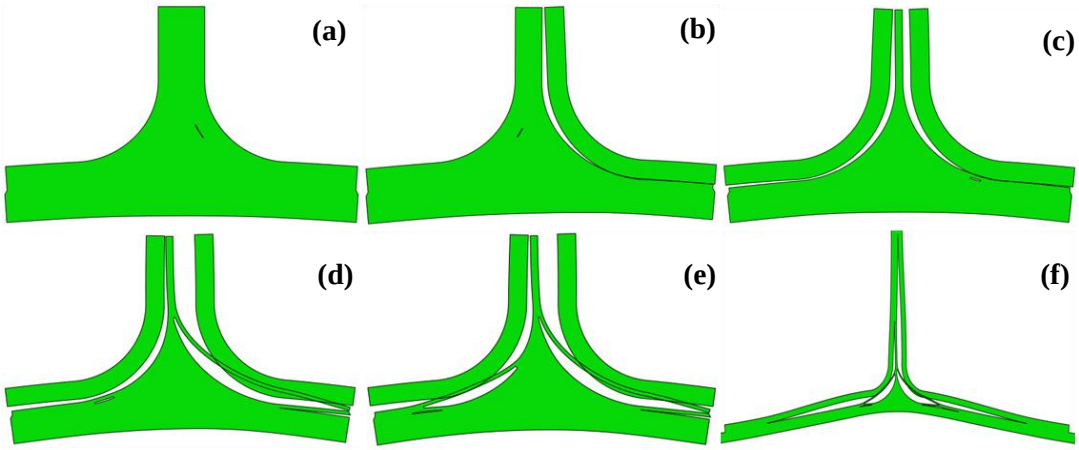

Figure 5.29- Delamination/debond propagation for the increased interface strength of the FM300 adhesive material a) pt2 (displacement = 7.65 mm, load = 2234 N), b) pt3 (displacement = 8.78 mm, load = 3030 N), c) pt4 (displacement = 10.01 mm, load = 4077 N), d) pt5 (displacement = 11.51 mm, load = 5493 N), e) pt6 (displacement = 11.51 mm, load = 5396 N), f) pt7 (displacement = 11.52 mm, load = 4697 N)

d-) 4th approach:

Fracture toughness values (G_{IC} and G_{IIC}) of the composite IM7/8552 material for Modes I and II are decreased with the same amount to change the failure mechanism to delamination between the stringer plies. Although, fracture toughness values are decreased to 20% of the initial values, initial failure is still the debond between the filler/stringer interface. The cohesive zone length decreases to 0.15 mm from 0.75 mm according to Equations (4.8- 4.9 and 4.10) and at least 2 or 3 elements should be used to get reliable results. Element size becomes 0.05 mm for the decreased toughness which causes a huge computation time. Therefore, element size cannot be decreased and fracture toughness of the composite material is not decreased further.

e-) 5th approach:

Interface strength values (t_I^0 and t_{II}^0) of the composite IM7/8552 material for Modes I and II are decreased with the same amount to change the failure mechanism to delamination between the stringer plies.

Load-displacement curves for the base model and the decreased interface strength are shown in Figure 5.30. Although, interface strength values of the composite material are decreased, the area under the load-displacement curve and maximum load increase, initial failure load remains approximately the same. There are three load drops on the curve. First load drop point is at 1648 N, second load drop is at 2033 N and last drop is at 2546 N which is the maximum load point. Sudden load drop after the maximum load causes convergence problems for the decreased interface strength, therefore load–displacement and failure propagation cannot be captured for further loading. Some critical points (pt1 – pt6) are shown on the load-displacement curve of the decreased interface strength which will be used to discuss the delamination/debond initiation (Figure 5.31) and propagation process (Figure 5.32) in detail.

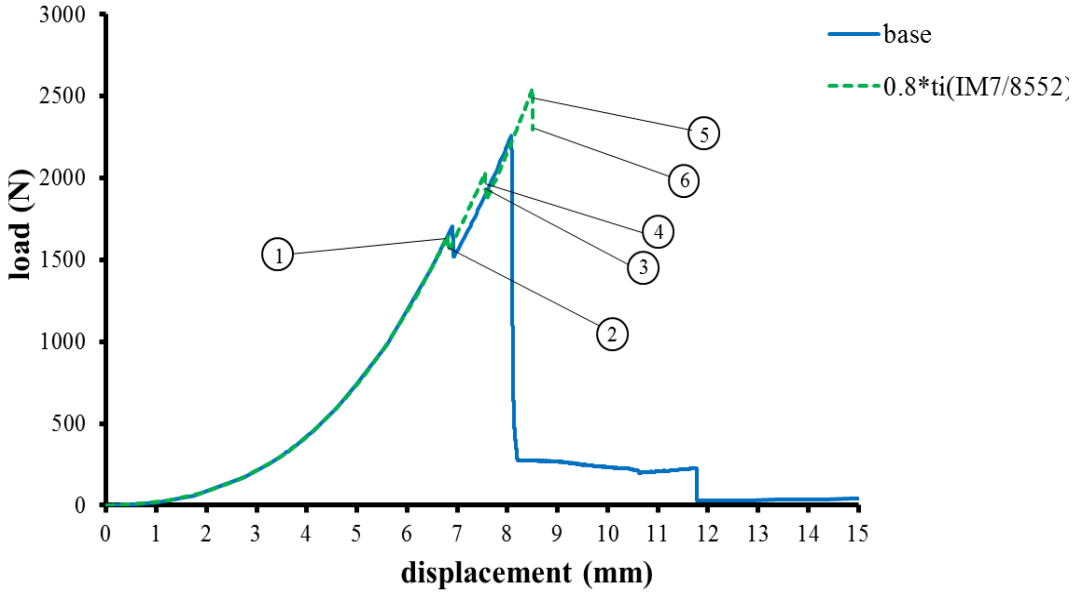

Figure 5.30- Load –displacement curves for the base and the decreased interface strength of the IM7/8552 composite material for 0^0 pull load

S22 and S12 stress contours for the decreased strength are shown in Figure 5.31 at the points 1 and 2 (Figure 5.30) corresponding to the delamination initiation process. Figure 5.31 (a) shows that before the crack initiation (at pt1 with 6.82 mm displacement and 1647 N load), there are S22 stress concentrations at the filler corners and there are S12 stress concentrations around the filler/stinger interfaces at 50° from the horizontal. At the initial debond location before the initiation, S22 is around 30 MPa and S12 is around 60 MPa indicating the failure initiates in mixed-mode. Figure 5.31 (b) shows that a delamination with 0.80 mm length (4 element size) between 5th and 6th left stringer plies initiates (at pt2 with 6.82 mm displacement and 1640 N load) at the curved region at 73° from the horizontal axis. The initial delamination causes a small load drop on the load-displacement curve (Figure 5.30).

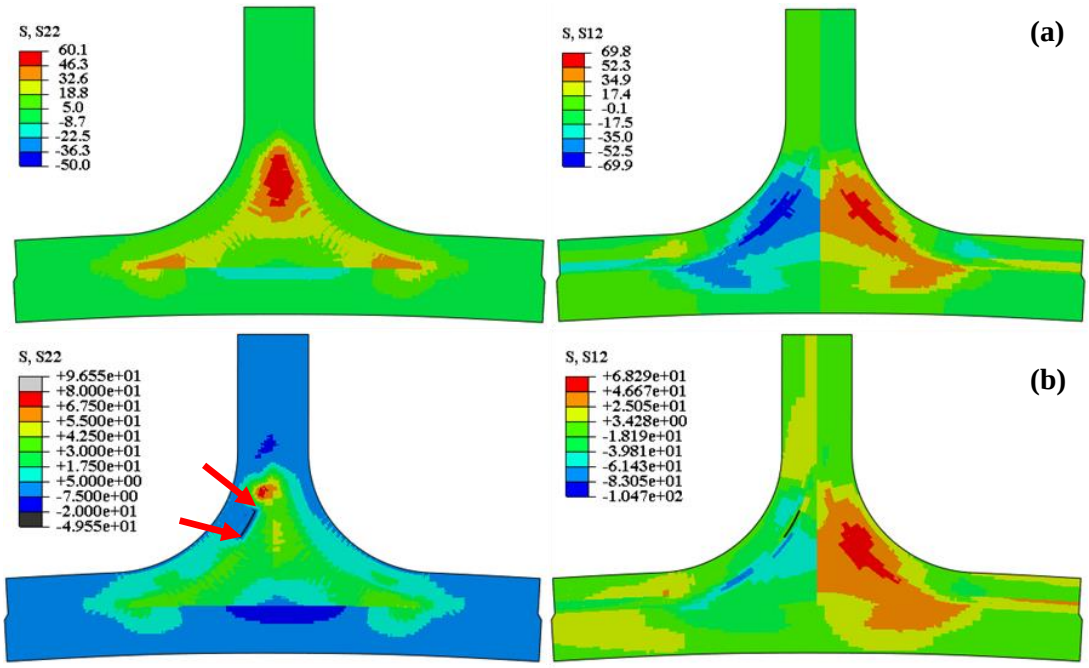

Figure 5.31- S22 and S12 stress components captured at the initial delamination point of the decreased interface strength of the IM7/8552 composite material a) pt1 (displacement =6.82 mm, load = 1647 N), b) pt2 (displacement =6.82 mm, load = 1640 N)

Delamination initiation/propagation scenario for the decreased strength is shown in Figure 5.32 through the points 2, 3, 4, 5 and 6 (Figure 5.30). Figures 5.32 (a) corresponds to the initial delamination point which is discussed in the above

paragraph. After the rapid increase in the debond, upper crack front slows 1.94 above the upper filler corner and lower crack front slows 2.74 mm from the left filler corner. Therefore, load starts to increase after the first delamination. As the displacement is increased, a debond at the filler/left stringer interface (at pt3 with 7.56 mm displacement and 2019 N) and a delamination in the skin upper plies (at pt4 with 7.56 mm displacement and 1946 N) are observed near the left filler corner as shown in Figure 5.32 (b) and (c). With the increase in the failures at the left side, right of the structure starts to carry much load and crack tips are stabilized at the left side, only upper crack tip of the initial delamination grows in a stable manner. This situation increases the carried load by the structure until maximum load point (8.51 mm displacement and 2546 N load). Near the maximum load point, a debond at the filler/right stringer initiates as seen in Figure 5.32 (d) (at pt5 with 8.51 mm displacement and 2530 N load), which cause a sudden load drop (Figure 5.30). The sudden load drop causes convergence problems, therefore load–displacement behavior and failure propagation cannot be captured for further loading.

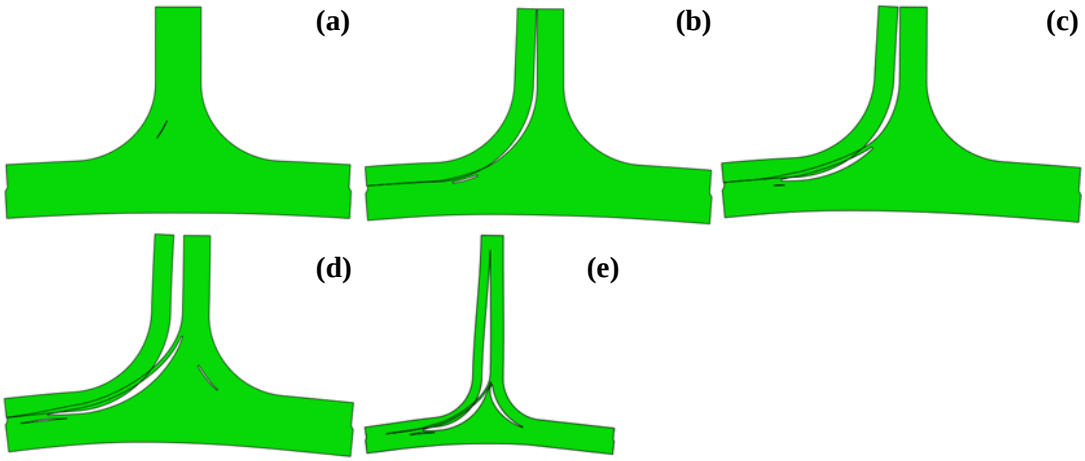

Figure 5.32- Delamination/debond propagation for the decreased interface strength of the IM7/8552 composite material a) pt2 (displacement = 6.82 mm, load = 1640 N), b) pt3 (displacement = 7.56 mm, load = 2019 N), c) pt4 (displacement = 7.56 mm, load = 1946 N), d) pt5 (displacement = 8.51 mm, load = 2530 N), d) pt6 (displacement = 8.51 mm, load = 2293 N)

In summary, although interface strength values of the composite IM7/8552 material decrease, the area under the load displacement curve, maximum failure load and displacement increase compared to the base model. Initial failure load remains almost constant and gradual degradation of the structure causes the gradual consumption of the absorbed strain energy rather than a rapid decrease. According to the results, leading delaminations between the stringer plies prior to debonds causes the increase in the absorbed energy and the maximum load. By ignoring the negligible decrease in the first failure load and letting a gradual degradation of the structure may be a choice for a damage tolerant design.

5.2.2.3.3 Failure Mechanism 3 – Debond of stringer flange tips from skin

The third failure mechanism is the debond of the stringer flange tips from the skin as shown in Figure 5.3. Two different approaches are investigated to capture the third failure mechanism; (a) decreasing the stringer flange length and (b) increasing the stringer thickness.

a-) 1st approach:

Stringer flange length, is decreased to change the failure mechanism to the debond of stringer flange tips from the skin. The base model has 56 mm flange length whereas stringer flange length decreased to 20 mm for the modified model.

Load-displacement curves for the base model and decreased flange length are shown in Figure 5.33. Compared to the base model, the decreased stringer flange length load displacement curve has only one load drop with no initial failure. The structure also shows no residual strength. Some critical points (pt1 – pt3) are shown on the load-displacement curve of the decreased flange length which are used to discuss the delamination/debond initiation (Figure 5.34) and propagation process (Figure 5.35) in detail.

S22 and S12 stress contours for the decreased flange length are shown at the points 1 and 2 (Figure 5.33) in Figure 5.34 corresponding to the delamination initiation process. Figure 5.34 (a) shows that, before the crack initiation (at pt1 with 7.70 mm displacement and 1935 N load), there are S22 stress concentrations

at the filler corners and flange tips and there are S12 stress concentrations at the flange tips and around the filler/stringer interfaces at the curved region at 60° from the horizontal. At the initial debond location (flange tips) before the failure initiation, S22 is around 30 MPa and S12 is around 70 MPa indicating the failures initiate in mixed-mode. Debond of the stringer flange tips from the skin are observed (at pt2 with 7.74 mm displacement and 1960 N load) as shown in Figure 5.34 (b) near the maximum load point (7.84 mm displacement and 2012 N load).

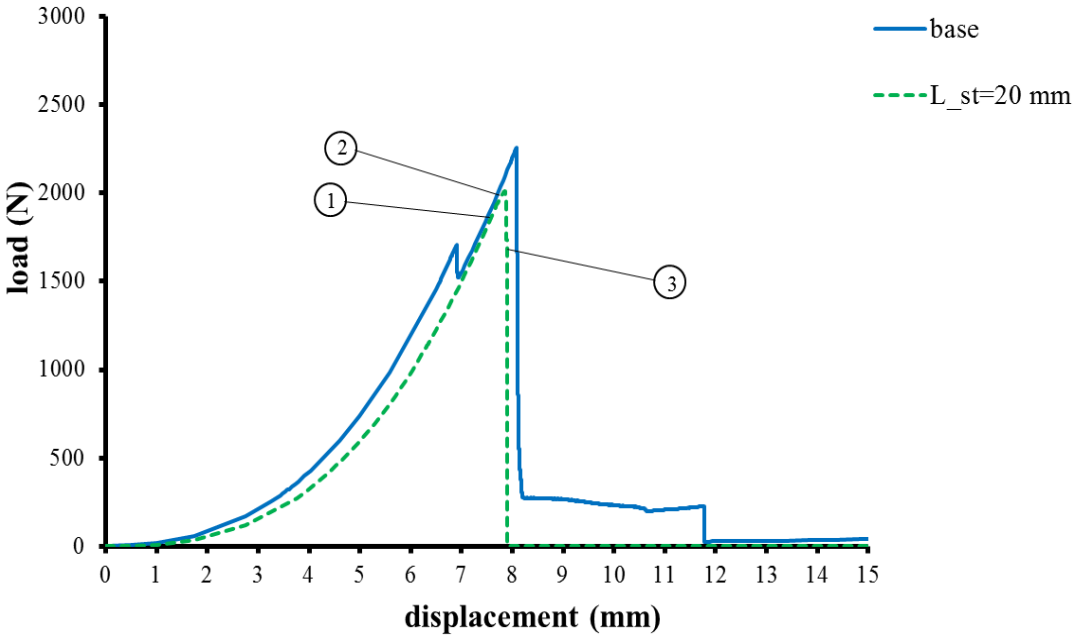

Figure 5.33- Load–displacement curves for the base model and the decreased stringer flange length for 0^0 pull load

Delamination initiation/propagation scenario for the decreased stringer length is shown in Figure 5.35 through the points 2 and 3 (Figure 5.33). Figures 5.35 (a) corresponds to the initial debond point which is discussed in the above paragraph. After the initial failure, debond propagates to the center of the structure as shown in Figure 5.35 (b). The propagation results in a complete separation of the stringers from the skin in a sudden load drop (Figure 5.33). There is no other delamination or debond in the structure other than the debond between the skin and the stringer.

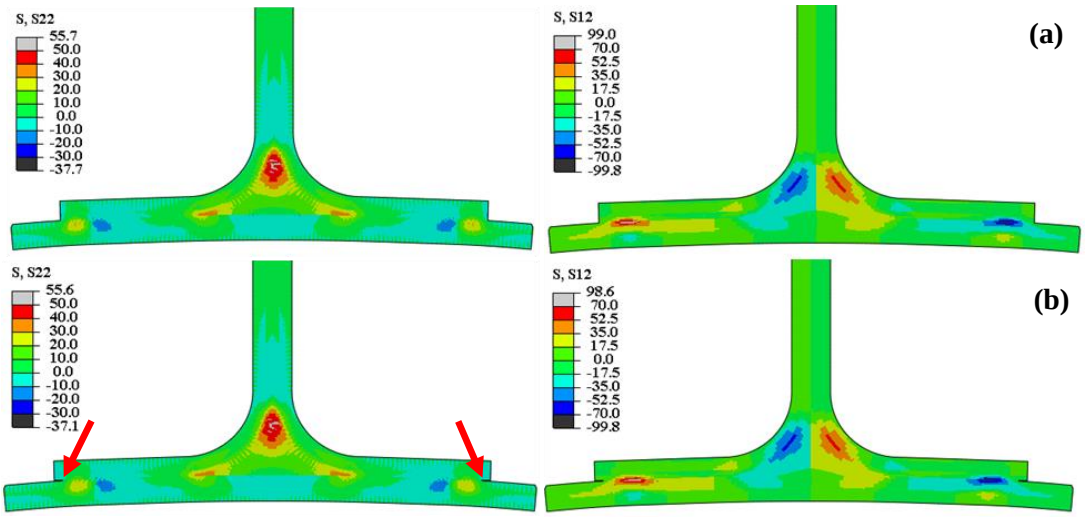

Figure 5.34- S22 and S12 stress components captured at the initial delamination point for the decreased stringer flange length a) pt1 (displacement =7.70 mm, load = 1935 N), b) pt2 (displacement =7.74 mm, load = 1960 N)

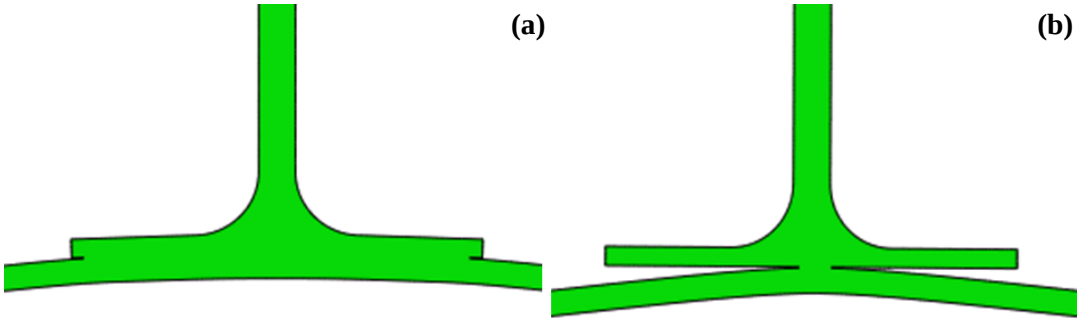

Figure 5.35- Delamination/debond propagation for the decreased stringer flange length a) pt2 (displacement = 7.74 mm, load = 1960 N), b) pt3 (displacement = 7.90 mm, load = 1665 N)

Only one load drop is present in the load-displacement curve with no initial delamination or debond. The area under the load-displacement curve decrease and the maximum failure load decrease to 2012 N from 2257 N for the decreased stringer flange length compared to the base model. The T-joint also shows no residual strength with the decreased flange length. Advantage of the decreased length is the higher initial failure load compared to the base model. Therefore, if no delamination methodology is chosen for the damage tolerance analysis, decreasing the flange length is a good choice which also brings weight reduction. Failure

initiation and propagation scenario completely change with the reduction of the stringer length. But the complete separation of the stringer from skin without any internal damage in the parts may be desirable in terms of the repair and maintenance point of view. Because, current parts may be used again with the proper repair methods which can also restore the initial stiffness and strength of the structure.

b-) 2nd approach:

Stringer thickness is increased to change the failure mechanism to the debond of stringer flange tips from the skin. The base model has 0.9 mm thickness whereas stringer thickness is increased to 2.7 mm for the modified model.

Load-displacement curves for the base model and increased stringer thickness are shown in Figure 5.36. Compared to the base model, the decreased stringer flange length curve has only one load drop with no initial failure. The structure also shows no residual strength. Some critical points (pt1 – pt3) are shown on the load-displacement curve of the increased stringer thickness which are used to discuss the delamination/debond initiation (Figure 5.37) and propagation process (Figure 5.38) in detail.

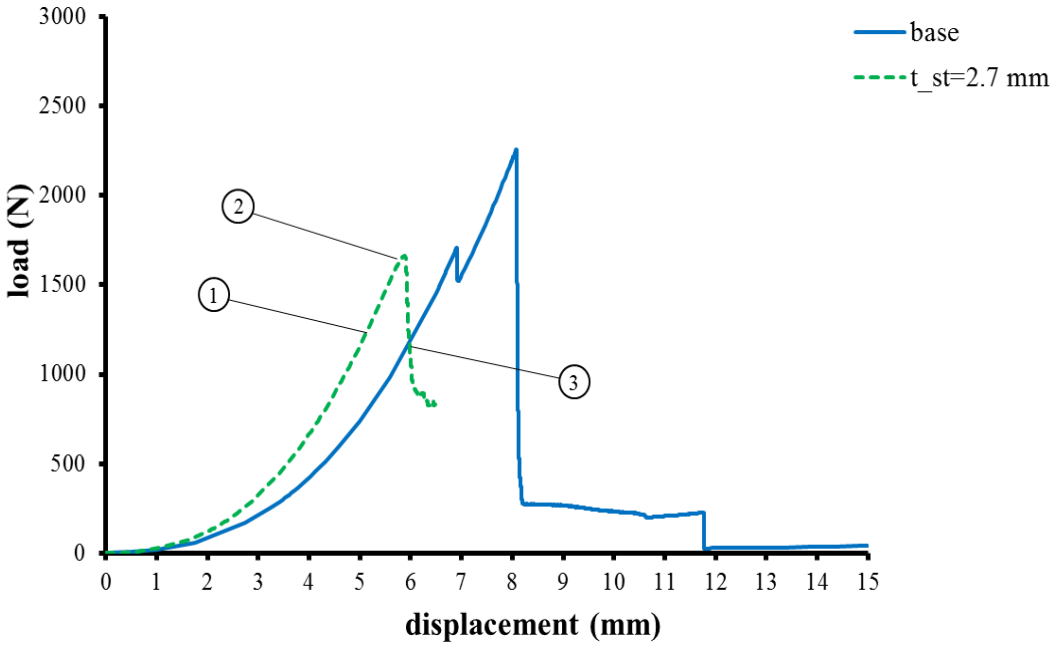

Figure 5.36- Load–displacement curves for the base model and the increased stringer thickness for 0^0 pull load

S22 and S12 stress contours for the increased thickness are shown at the points 1 and 2 (Figure 5.36) in Figure 5.37 corresponding to the delamination initiation process. Figure 5.37 (a) shows that, before the crack initiation (at pt1 with 5.06 mm displacement and 1193 N load), there are S22 stress concentrations at the filler corners and flange tips and there are S12 stress concentrations at the flange tips and around the filler/stringer interfaces at the curved region at 60° from the horizontal axis. At the initial debond location before the failure initiation, S22 is around 40 MPa and S12 is around 60 MPa indicating the failures initiate in mixed-mode. Initial debond of the stringer flange tips from the skin are observed (at pt2 with 5.70 mm displacement and 1593 N load) as shown in Figure 5.37 (b).

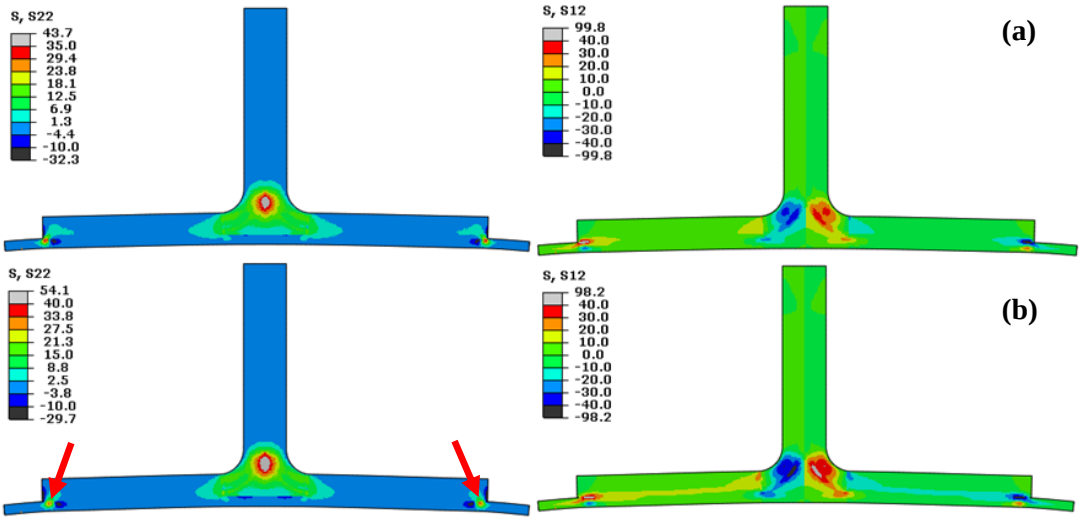

Figure 5.37- S22 and S12 stress components captured at the initial delamination point for the increased stringer thickness a) pt1 (displacement = 5.06 mm, load = 1193 N), b) pt2 (displacement = 5.70 mm, load = 1593 N)

Delamination initiation/propagation scenario for the increased stringer thickness is shown in Figure 5.38 through the points 2 and 3 (Figure 5.36). Figures 5.38 (a) corresponds to the initial debond point which is discussed in the above paragraph. After the debonds initiated, load increase to maximum point (5.90 mm displacement and 1662 N). A sudden load drop is observed for further increase in displacement (Figure 5.36). Debonds move towards the midpoint as seen in Figure

5.38 (b) (at pt3 with 5.97 mm displacement and 1186 N load) and a complete separation of the stringers from the skin occurs.

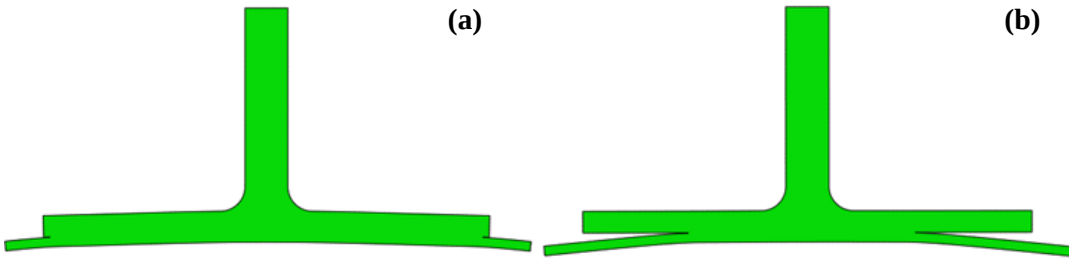

Figure 5.38- Delamination/debond propagation for the increased stringer thickness a) pt2 (displacement = 5.70 mm, load = 1593 N), b) pt3 (displacement = 5.97 mm, load = 1186 N)

Only one load drop is present in the load-displacement curve with no initial delamination or debond. The area under the load displacement curve, maximum failure load and displacement are decreased for the increased stringer thickness compared to the base model. Failure initiation and propagation scenario completely change. The T-joint also shows no residual strength with the increased stringer thickness. Stiff stringer flanges do not deform much compared to skin and interlaminar stresses are created between skin and stringers which cause the debonds. Therefore, a gradual reduction of the stringer flange thickness should be preferred in the structures.

5.2.2.3.4 Failure Mechanism 4 –Debond in filler/stringers intersection in vertical direction

Filler area is left empty to change the failure mechanism to the failure initiation by debonding of filler/stringers intersection in the vertical direction as seen in Figure 5.4.

Load-displacement curves for the base model and empty filler are shown in Figure 5.39. Compared to the base model the area under the load-displacement curve and the max load decrease in considerable amounts. Initial stiffness of the structure also decreases. Some critical points (pt1 – pt4) are shown on the load-displacement curve of the empty filler area which will be used to discuss the

delamination/debond initiation (Figure 5.40) and propagation process (Figure 5.41) in detail.

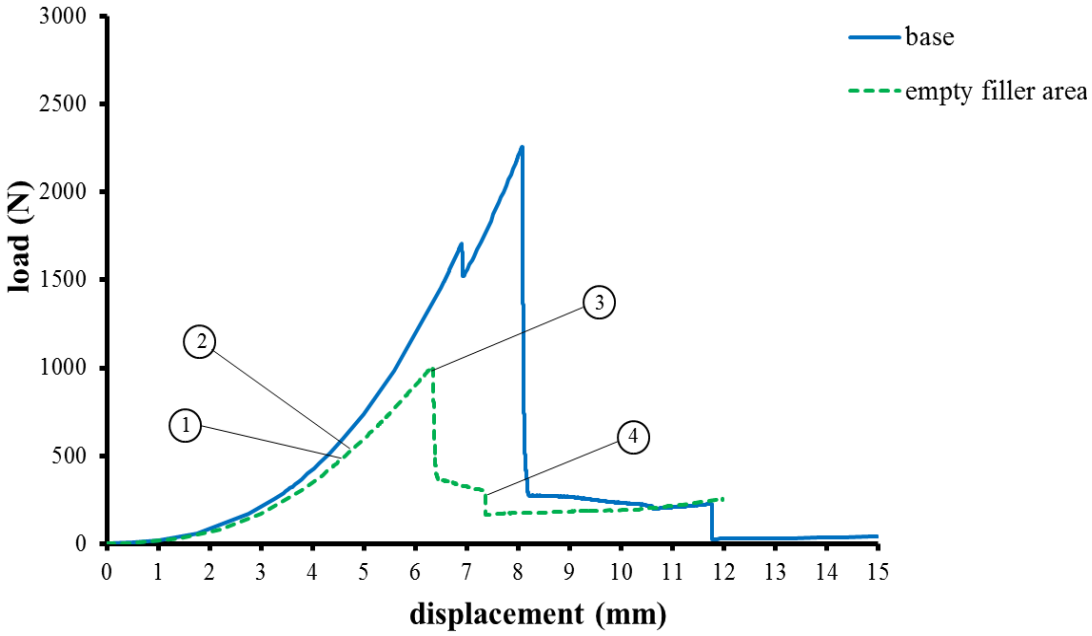

Figure 5.39- Load–displacement curves for the base model and the empty filler area for 0^0 pull load

S22 and S12 stress contours for the empty filler area are shown at the points 1 and 2 (Figure 5.39) in Figure 5.40 corresponding to the delamination initiation process. Figure 5.40 (a) shows that, before the crack initiation (at pt1 with 4.64 mm displacement and 502 N load), there is S22 stress concentration at the upper filler corner and there are S12 stress concentration at the left and right filler corners. At the initial debond location, upper filler corner, before the initiation, S22 is around 50 MPa and S12 is almost 0 MPa indicating the failure initiates in Mode I. Debond of the stringers are observed at the filler upper corner (at pt2 with 4.85 mm displacement and 556 N load) as shown in Figure 5.40 (b). Compared to the other numerical simulations, a load drop is not observed for the initial failure in the load-displacement curve of the empty filler area.

Delamination initiation/propagation scenario for the empty filler area is shown in Figure 5.41 through the points 2, 3 and 4 (Figure 5.39). Figures 5.41 (a) corresponds to the initial debond point which is discussed in the above paragraph. After the initial failure, debond propagates in the vertical direction between the

stringer interface with the same stiffness trend before the failure. Near the max load point (6.33 mm displacement and 1004 N load), debonds are seen at the skin/stringer interfaces near the filler corners as shown in Figure 5.41 (b) (at pt3 with 6.33 mm displacement and 997 N load). A sudden load drop is then seen in the load –displacement curve (Figure 5.39). Another small sudden load drop is seen after the initiation of delaminations between the skin upper plies under the stringer flange tips (at pt4 with 5.37 mm displacement and 200 N load), residual strength is then reached (Figure 5.39).

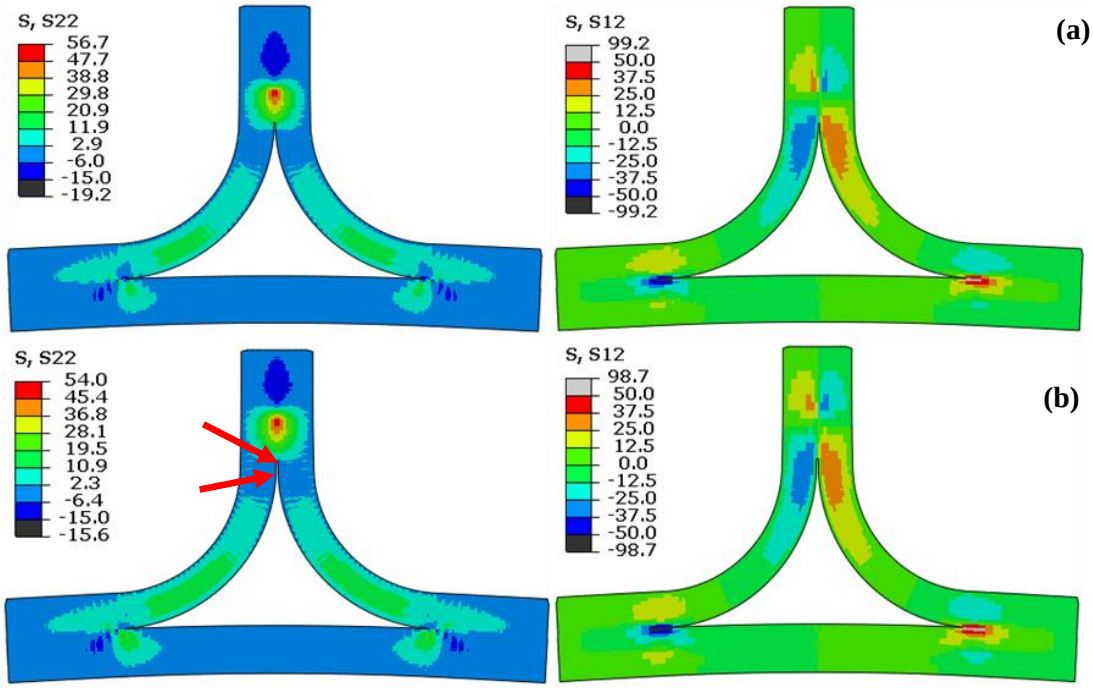

Figure 5.40- S22 and S12 stress components captured at the initial delamination point for the empty filler area a) pt1 (displacement = 4.64 mm, load = 502 N), b) pt2 (displacement = 4.85 mm, load = 556 N)

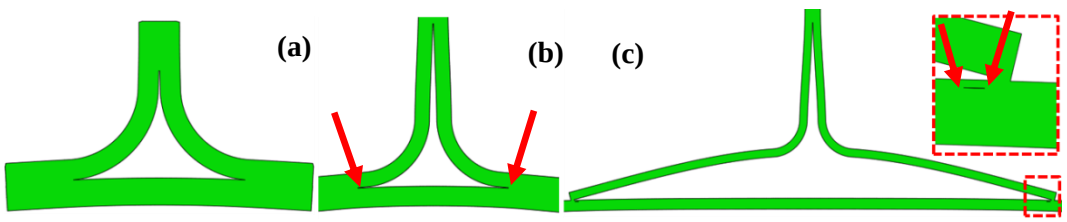

Figure 5.41- Delamination/debond propagation for the empty filler area a) pt2 (displacement = 4.85 mm, load = 556 N), b) pt3 (displacement = 6.33 mm, load = 997 N), c) pt4 (displacement = 7.37 mm, load = 200 N)

In summary, the initial stiffness of the structure, the area under the load-displacement curve and the maximum failure load decrease. It can be stated that, a filler material is necessary for the structure for high load carrying capacity. Compared to the other numerical simulations, initial debond between the stringers does not cause a load drop. Sudden load drop is seen when the stringers start to separate from the skin. Therefore, high bonding strength between the skin and stringers is crucial in terms of structural integrity. Z-pins, sewing or some other strengthening mechanism between the skin and stringers near the filler corners can be used to enhance the carried load by the structure especially when the area between the skin and the stringers is not filled with a material.

In Chapter 5, delamination/debond behavior of T-joints is investigated with 2D FE models with CZM. In Section 5.1, failure initiation mechanisms of T-joints are presented which are observed in the literature. In Section 5.2, numerical studies of the considered T-joint are presented. In section 5.2.1, the geometry and the FE model of the T-joint are explained. In Section 5.2.2, numerical studies of the T-joint are presented. For ease of following, numerical studies which are carried out in Section 5.2.2 are summarized in Table 5.4. Other than the investigated parameters in Section 5.2.2.3, boundary conditions, filler material, stringer curvature radius, skin thickness, etc. affect the failure behavior of the structure and may be further investigated.

Table 5.4– Summary of the T-joint numerical studies

Section	Explanations
Section 5.2.2.1 – Angle Pull Loads	Delamination/debond behavior of the T-joint is studied for 0°, 45° and 90° pull loads.
Section 5.2.2.2 – Cohesive vs. Non-Cohesive Models For 0° Pull Load	Cohesive vs. non-cohesive model numerical results are compared for 0° pull load. Delamination/debond behavior of the cohesive model is discussed in detail.

Table 5.4 contd– Summary of the T-joint numerical studies

Section 5.2.2.3 – Failure Modes For 0° Pull Load	In a parametric study, by changing geometry and material properties of the T-joint, failure initiation mechanisms which are given in Section 5.1 are tried to be captured for 0° pull load.
1st failure mechanism: Debond at filler/stringer interfaces	Base T-joint model shows this failure mechanism which is discussed in Section 5.2.2.2.
2nd failure mechanism: Delamination between the stringer plies	1st approach: The placement of the 0^0 and 90^0 stringer plies are interchanged.
	2nd approach: The fracture toughness values (G_{IC} and G_{IIC}) of the FM300 adhesive material are increased to 800%.
	3rd approach: The interface strength values (t_I^0 and t_{II}^0) of the FM300 adhesive material are increased to 130%.
	4th approach: The fracture toughness values (G_{IC} and G_{IIC}) of the IM7/8552 composite material are decreased. This approach is not able to change the initiation mechanism.
	5th approach: The interface strength values (t_I^0 and t_{II}^0) of the IM7/8552 composite material are decreased to 80%.
3rd failure mechanism: Debond of the stringer flange tips from the skin	1st approach: The stringer flange length is decreased to 20 mm from 56 mm.
	2nd approach: The stringer thickness is increased to 2.7 mm from 0.9 mm.
4th failure mechanism: Debond at the filler/stringers intersection in vertical direction	1st approach: The filler area is left empty.

CHAPTER 6

SUMMARY AND CONCLUSION

Chapters 4 and 5 are the main focus of this study. Therefore, summaries and conclusions of these chapters are provided below.

Following summaries and discussions can be made for the study of standard fracture tests, DCB, ENF and MMB, in Chapter 4:

- DCB, ENF and MMB test numerical load-displacement curves agree well with the analytical solutions and numerical and experimental results from the literature. Therefore, Abaqus CZM is considered to be able to predict delamination initiation and propagation in composite materials correctly.
- In the sensitivity study for DCB and ENF tests, it is seen that investigated FE and CZM parameters (element type, element size, viscosity value, penalty stiffness, interface strength and fracture toughness) have the same effect on the load-displacement curves for each test.
- CPE4I (plane strain, full integration, enhanced strain modes) and CPE4R (plane strain, reduced integration) element types give closer results to the analytical solution compared to CPE4 (plane strain, full integration) elements especially for coarse meshes.
- CPE4I element type requires more computing time because of the full integration, but they should be the choice for coarse mesh models and complex geometries. This is due to the fact that they don’t suffer from the shear locking and hourglass effects under flexural loading which are seen in CPE4 and CPE4R elements, respectively,
- As element size decreases, numerical results get closer to the analytical solution for all element types. Increase in the element size cause oscillations in the numerical solutions in the delamination propagation

region (softening region). Therefore, a suitable element size should be chosen for optimal solution with less computation time.

- Increase in the viscosity value eliminates the oscillatory behavior in the softening region and requirement of finer mesh. However, use of higher values cause unconservative results with an increase in the area under the load-displacement curves and viscous dissipation energy. Decrease in the viscosity value causes oscillations in the softening region and convergence problems. Values around 1e-5 are generally used in the literature and seem to be an optimal choice for the current FE and cohesive parameters for the fracture test simulations.
- FE models with very low penalty stiffness show decrease in initial elastic stiffness with no delamination. For FE models with very high stiffness, the area under load-displacement curve increases and the solution diverges from the analytical solution with the oscillatory. One interesting result of the increased penalty stiffness is the increase in the stress values around the crack tip which are higher than the interface strength. Therefore, very low and very high penalty stiffness values should be avoided in numerical simulations. Although, stiffness values around 1e5 -1e6 seem to give reliable results, stiffness value should be decided based on numerical trial studies and experimental results.
- Decreasing the interface strengths decreases the maximum traction and the area under the load-displacement curves. One advantage of decreasing the strength value is the increased cohesive zone length; therefore, coarser mesh can be used without convergence difficulties. Numerical solutions get closer to analytical result as interface strength increases but convergence problems occur.
- Increasing the fracture toughness values increase the area under the load-displacement curves. Initial stiffness of the structure is not affected by the fracture toughness change whereas the maximum traction increases with increasing fracture toughness.
- As each parameter in the sensitivity study of the DCB test is changed, the final crack and the cohesive zone lengths also change. Therefore,

experimental results are required to match the crack size and the cohesive length with the numerical results if crack or cohesive lengths are important parameters for the analysis.

Following summaries and discussions can be made for the numerical T-joint study in Chapter 5:

- Detailed delamination initiation and also propagation scenarios are captured for T-joints for 0°, 45° and 90° pull loads. In the literature, numerical studies mainly focus on the initiation process; in this study, propagation behavior until the complete failure is also captured. Numerical results show that, delamination initiation/propagation scenarios are different for each loading case. Bonding lines and ply interfaces of the skin and stringers around the filler/stringer interfaces are critical locations for delamination initiation and propagation which shows stress concentrations. It is seen that delaminations initiate and propagate in mixed-mode generally.
- FE models of T-joints in the literature generally include cohesive layers at the bonding lines and at most additional cohesive layers in the neighboring skin/stringer ply interfaces of the bonding lines. Or, a few cohesive layers are inserted in FE models at the interfaces that are seen critical in the experiments. In this study, a detailed FE model of the considered T-joint is created which has cohesive layers for all bonding lines and the ply interfaces of the skin and stringers. Therefore, it could be possible to see the delamination/debond initiation and propagation through the complete structure during the complete loading history.
- In the comparison of the FE model results with and without cohesive layers for 0° pull load, it is shown that the addition of the cohesive layers does not affect the elastic behavior in terms of the load-displacement behavior and stress fields.
- Four delamination initiation mechanisms are observed for T-joints in the literature: (1) debond of the filler/stringer interface, (2) delamination between the plies in the stringer laminate at the curved region, (3) debond of the stringer flange tips from the skin, (4) debond of filler/stringers

intersection in the vertical direction. In a parametric study, these mechanisms are captured by modifying the T-joint geometry or material properties.

- Failure Mechanism 1 is the debond of the filler/stringer interface. This mechanism is the default failure mechanism for the base T-joint model and is discussed in the above paragraphs.
- Failure Mechanism 2 is the delamination between the stringer plies. Five different approaches are investigated to capture the second failure mechanism.

- 1st approach is interchanging the placement of the 0^0 and 90^0 plies of the stringers (from [90/90/0/0/45/45] to [0/0/90/90/45/45]). Failure scenario changes with the change in ply sequence; the 1^{st} and 2^{nd} failure mechanism occur almost at the same time. The first and second failure loads decrease because of the delaminations between the stringer plies in addition to the debonds. Towards the end of the failure process, modified layup shows the residual strength for longer displacement. Therefore, the modified layup can be a design choice for its residual strength.
- 2nd approach is increasing the fracture toughness values (G_{IC} and G_{IIC}) of the FM300 adhesive material to 800% of the initial values. The area under the load displacement curve, the initial failure load and displacement, the maximum failure load and displacement increase significantly by increasing fracture toughness. Although delamination between the stringer plies is captured, 800% increase in fracture toughness values is hard to achieve. But, Z pins or some other crack arresting mechanism can be used to increase the area under the load displacement curve and the maximum failure load which can be considered as fracture toughness increase.
- 3rd approach is increasing the interface strength values (t_I^0 and t_{II}^0) of the FM300 adhesive to 130% of the initial value. The area under the load-displacement curve, the initial failure load and displacement, the maximum failure load and displacement increase significantly by increasing interface strength. Delamination propagation scenario is also changed. A 30%

increase in the interface strength seems to be achievable maybe with some other matrix material.

- 4th approach is decreasing the fracture toughness values (G_{IC} and G_{IIC}) of the IM7/8552 composite material. Although, fracture toughness values are decreased to 20% of the initial values, initial failure is still the first failure mechanism. Because of the lower cohesive zone length, small element size is required which causes a huge computation time. Therefore, element size cannot be decreased and fracture toughness of the composite material is not decreased further.
- 5th approach is decreasing the interface strength values (t_I^0 and t_{II}^0) of the IM7/8552 composite material to 80% of the initial values. Although interface strength values are decreased, the area under the load displacement curve, the maximum failure load and displacement increase. By ignoring the negligible decrease in the first failure load and letting a gradual degradation of the structure may be a choice for a higher performance of the T-joint.

• Failure Mechanism 3 is the debond of stringer flange tips from skin. Two different approaches are investigated to capture the second failure mechanism.

- 1st approach is decreasing the stringer flange length to 20 mm from 56 mm. Only one load drop is present in the load-displacement curve with the complete separation of the stringers from the skin. The area under the load-displacement curve and the maximum load decrease and the T-joint shows no residual strength. If no delamination methodology is chosen for damage tolerance analysis, decreasing the flange length is a good choice for which maximum load is higher than the initial failure of the base model. Decreasing stringer flange length also brings weight reduction to structure. The complete separation of the stringer from the skin without any internal damage in the parts may be desirable in terms of repair and maintenance point of view. Because, current parts may be used again with the proper repair methods which also restore the initial stiffness and strength of the structure.

- 2nd approach is increasing the stringer thickness to 2.7 mm from 0.9 mm. By increasing the stringer thickness, only one load drop is seen in the load-displacement curve with the complete separation of the stringers from the skin. Although, a considerable material is added to the structure, the area under the load displacement curve, the maximum failure load and displacement decrease with no residual strength. Stiff stringer flanges do not deform as much as compared to skin and interlaminar stresses are created between the skin and stringers at the flange tips; therefore, a gradual reduction of the stringer flange thickness should be preferred in structures.

- Failure Mechanism 4 is the debond in filler/stringers intersection in the vertical direction. By leaving the filler area empty, this mechanism is captured. The initial stiffness of the structure, the area under the load-displacement curve, the initial and maximum failure loads decrease significantly. Therefore, a filler material is necessary for the structure to increase the load carrying capacity. Compared to the other numerical simulations, initial debond between the stringers does not cause a load drop, instead sudden load drop occurs when the stringers start to separate from the skin. Therefore, high bonding strength between the skin and stringers is crucial in terms of structural integrity. Z-pins, sewing or some other strengthening mechanism between the skin and stringers near the filler corners can be used to enhance the load carrying capacity of the structure.

Concluding Remarks:

- DCB, ENF and MMB numerical simulations show that the Abaqus CZM can be considered as a reliable tool for the delamination initiation and propagation prediction.

- In the DCB and ENF sensitivity studies, it is shown that numerical results depend on various FE model and cohesive parameters: element size, element type, viscosity, interface stiffness, interface strength and fracture toughness. Depending on the requirements, an optimal numerical solution with less computation time can be achieved by modifying these parameters.

- In the DCB sensitivity study, it is shown that crack and cohesive zone lengths are different for different cohesive zone parameters. Therefore, validation of the numerical solutions with the experiment may be required to capture the correct set of parameters.
- Numerical results for the T-joint show that, delamination initiation and propagation scenarios are different for 0°, 45° and 90° pull loads. By modeling multiple cohesive layers in the structure, multiple delaminations/debonds during the complete loading history are able to be captured. Additionally, the residual strengths of the T-joints and multiple load drops on the load-displacement curves are captured.
- T-joint numerical results show that the geometry and material parameters affect the delamination/debond initiation and propagation process. The initial and maximum failure loads, the area under load-displacement curve and stress fields are affected. Different failure initiation mechanisms can be captured by changing the geometry or material parameters. Therefore, a design solution can be determined for the optimal solution with a parametric study as in this paper.

CHAPTER 7

FUTURE WORK

Future work for the composite T-joint study can be conducted in two different objectives.

1st objective of the future work can be to develop the current 2D FE model of the T-joint to a 3D aircraft panel and investigate the static and dynamic load effects on the structure. This study can be conducted in the following steps:

1- Explicit runs can be carried out with the current 2D FE model for 0° pull load and results can be compared with the implicit solutions. Crack growth speeds can be investigated with the explicit runs.

2- Explicit runs can be carried out with the current 2D FE model for low velocity impact load. Delamination/debond behavior can be investigated and crack growth speeds can be investigated.

3- In the literature, it is observed that, composite material fiber/matrix damages affect the delamination/debond behavior. Therefore, composite material fiber/matrix damages (Puck, Hasnhin, Tsai-Hill criteria, etc.) can be included into the 2D T-joint FE model to capture a more realistic structural behavior. Steps 1-2 can be repeated with the modified model.

4- A 3D FE model of the current T-joint geometry can be created. Steps 1-3 can be repeated with the 3D FE model.

5- A 3D FE model of a stiffened panel can be created to investigate the delamination/debond behavior.

6- Implicit runs can be carried out with the 3D stiffened panel for axial compression and shear load cases.

7- Explicit runs can be carried out with the 3D stiffened panel axial compression and shear load cases and for low velocity impact load.

2nd objective of the future work can be to strengthen the structure in through the thickness direction to prevent delaminations/debonds. Available strengthening methods (Z-pins, sewing, etc.) can be investigated and some modifications to these methods may be given to maximize their effects. A new method maybe developed based on the findings through the strengthening study, a new manufacturing method maybe proposed which provides through the thickness strength.

REFERENCES

[1] Orifici, A.C., Shah, S.A., Herszberg, I., Kotler, A., Weller, T., "Failure Analysis in Postbuckled Composite T-Sections", Composite Structures 86 (2008) 146–153

[2] Orifici, A.C., Thomson, R.S., Herszberg, I., Weller, T., Degenhardt, R., Bayandor, J., "An Analysis Methodology for Failure in Postbuckling Skin–Stiffener Interfaces", Composite Structures 86 (2008) 186–193

[3] Degenhardt, R., Kling, A., Rohwer, K., Orifici, A.C., Thomson, R.S., "Design And Analysis of Stiffened Composite Panels Including Post-Buckling And Collapse", Computers and Structures 86 (2008) 919–929

[4] "COCOMAT Home Page", www.cocomat.de (10 October 2013)

[5] Orifici, A.C., Abramovich, H., Herszberg, I., Kotler, A., Weller, T., Thomson, R.S., Bayandor, J., "Failure in Skin-Stiffener Interfaces Under Postbuckling Loads", http://www.cocomat.de/Endmeeting/Abstracts/24_CRC-ACS_Orifici.pdf (22 December 2013)

[6] Orifici, A.C., Thomson, R.S, Degenhardt, R., Bisagni, C., Bayandor, J., "A Finite Element Methodology for Analyzing Degradation and Collapse in Postbuckling Composite Aerospace Structures", Journal of Composite Materials, Vol. 0, No. 00/2009

[7] Orifici, A.C., Thomson, R.S., Degenhardt, R., Kling, A., Rohwer, K., Bayandor, J., "Degradation Investigation in a Postbuckling Composite Stiffened Fuselage Panel", Composite Structures 82 (2008) 217–224

[8] Orifici, A.C., Alberdi, I.O.Z., Thomson, R. S., Bayandor, J., "Compression and Post-Buckling Damage Growth and Collapse Analysis of Flat Composite Stiffened Panels", Composites Science and Technology 68 (2008) 3150–3160

[9] Orifici, A.C., Thomson, R.S., Degenhardt, R., Bisagni, C., Bayandor, J., "Development of a Finite-Element Analysis Methodology for The Propagation Of Delaminations in Composite Structures", Mechanics of Composite Materials, Vol. 43, No. 1, 2007

[10] Orifici, A.C., Thomson, R.S., Degenhardt, R., Büsing, S., Bayandor, J., "Development of a Finite Element Methodology for Modeling Mixed-Mode Delamination Growth in Composite Structures", Paper presented at 12th Australian International Aerospace Congress Australia, 2007

[11] Mandell, J.F., Cairns, D.S., Samborsky, D.D., Morehead, R.B., Haugen D.J., "Prediction of Delamination in Wind Turbine Blade Structural Details", Journal of Solar Energy Engineering-transactions of The Asme - J SOL ENERGY ENG 01/2003; 125(4).

[12] Phillips, H. J., Shenoi R.A., "Damage Tolerance of Laminated Tee Joints in FRP Structures", Composites Part A 29A (1998) 465-478 1998

[13] Dharmawan, F., Thomson, R.S., Li, H., Herszberg, I., Gellert, E., "Geometry and Damage Effects in A Composite Marine T-Joint", Composite Structures 66 (2004) 181–187

[14] Li, H.C.H., Dharmawan, F., Herszberg, I., John, S., "Fracture Behavior of Composite Maritime T-Joints", Composite Structures 75 (2006) 339–350

[15] Hawkins, G.L., Shenoi, R.A., "A Parametric Study To Determine The Influence Of Geometric Variations On The Performance Of A Bulkhead To Shell Plating Joint", University of Southampton, Department of Ship Science, Faculty of Engineering and Applied Science, Large Deflection Behavior of GRP Panels with Attachments, Ship Science Report No. 68, February 1993

[16] Cui, H., Li, Y., Koussios, S., Beukers, A., "Parametric Evaluation On The Curved Part Of Composite T-Joints Based On Numerical Simulation", 27th International Congress of the Aeronautical Sciences, Nice-France, 2010

[17] University of Deleware, Center for Composite Materials, http://www.ccm.udel.edu/Tech/Lam3D/Theory.htm (29 December 2013)

[18] Hélénon, F., Wisnom, M.R., Hallett, S.R., Trask R.S., "Numerical Investigation into Failure of Laminated Composite T-Piece Specimens Under Tensile Loading", Composites: Part A 43 (2012) 1017–1027

[19] Camanho, P.P., Dávila, C.G., "Mixed-Mode Decohesion Finite Elements for the Simulation of Delamination in Composite Materials", NASA/TM-2002-211737

[20] Song, K., Dávila, C.G., Rose, C.A., "Guidelines and Parameter Selection for the Simulation of Progressive Delamination", Abaqus Users' Conference, 2008

[21] Albiol, D., "Buckling Analyses of Composite Laminated Panels with Delamination", Tesi di Laurea, Politecnico Di Milano, Italia

[22] Abaqus/CAE V6.12 User's Manual

[23] Reeder, J.R., "Refinements to the Mixed-Mode Bending Test for Delamination Toughness", NASA Langley Technical Report Server, 2000

[24] Bruyneel, M., Delsemme, J.P., Jetteur, Ph., Germain, F., "Modeling Inter-Laminar Failure in Composite Structures: Illustration on an Industrial Case Study", Appl. Compos. Mater. (2009) 16:149–162

[25] Turon, A., Camanho, P.P., Costa, J., Dávila, C.G., "A Damage Model for the Simulation of Delamination in Advanced Composites Under Variable-Mode Loading", Mechanics of Materials 38 (2006) 1072–1089

[26] http://ksm.fsv.cvut.cz/~sejnom/download/pm10_tisk.pdf (05 July 2013)

[27] Raju, I.S., O'Brien, T.K., "Fracture Mechanics Concepts, Stress Fields, Strain Energy Release Rates, Delamination Initiation and Growth Criteria", Edited by Srinivasan Sridharan, Delamination Behaviour Of Composites, Woodhead Publishing, 2008

[28] Tomblin, J., "Overview of Composite Material Trends in Aviation Manufacturing", 2006, National Institute for Aviation Research (NIAR), Wichita State University, http://webfiles.wichita.edu/cedbr/WIRED_comp_ov_5_14_08.pdf (07 August 2013)

[29] http://www.boeing.com/commercial/aeromagazine/articles/qtr_4_06/article_04_1 . html, (05 July 2013)

[30] Tay, T.E., "Characterization And Analysis Of Delamination Fracture In Composites: An Overview Of Developments From 1990 to 2001", Appl. Mech. Rev. Vol. 56, no 1, January 2003

[31] Riccio, A., "Delamination in the Context of Composite Structural Design", Edited by Srinivasan Sridharan, Delamination Behaviour of Composites, Woodhead Publishing, 2008

[32] Anderson, T.L., “Fracture Mechanics – Fundamentals and Applications”, 2nd edition, CRC Press, 1995

[33] Griffith, A. A., “The Phenomena of Rupture and Flow in Solids”, Philosophical Transactions of the Royal Society of London. Series A, Containing Papers of a Mathematical or Physical Character, Vol. 221(1921), 163-198

[34] Irwin, G.R., “Analysis of Stresses and Strains Near the End of a Crack Traversing in a Plate”, Jnl. of Applied Mechanics, Trans. of ASME, 24, 1957, 351–369

[35] D5528-01, “Standard Test Method for Mode I Interlaminar Fracture Toughness of Unidirectional Fiber-Reinforced Polymer Matrix Composites”, American Society for Testing and Materials

[36] WK22949, “New Test Method for Determination of the Mode II Interlaminar Fracture Toughness of Unidirectional Fiber-Reinforced Polymer Matrix Composites Using the End-Notched Flexure (ENF) Test”, American Society for Testing and Materials

[37] D6671/D6671M-06, “Standard Test Method for Mixed Mode I-Mode II Interlaminar Fracture Toughness of Unidirectional Fiber Reinforced Polymer Matrix Composites”, American Society for Testing and Materials

[38] Silva, L.F.M., Campilho, R.D.S.G., “Advances in Numerical Modeling of Adhesive Joints”, Springer Briefs in Applied Sciences and Technology, 2012, pp. 1-93

[39] Meeks, C., Greenhalgh, E., Falzon, B.G., “Stiffener Debonding Mechanisms in Post-Buckled CFRP Aerospace Panels”, Composites: Part A 36 (2005) 934–946

[40] Rice, J.R., “A Path Independent Integral and the Approximate Analysis of Strain Concentration by Notches and Cracks”, Journal of Applied Mechanics, Vol.35, 1968, pp. 379-386

[41] Oliveira, J.M.Q., Moura, M.F.S.F., Silva, M.A.L., Morais, J.J.L., “Numerical Analysis of the MMB Test For Mixed-Mode III Wood Fracture”, Composites Science and Technology 67 (2007) 1764–1771

[42] Burlayenko, V.N., Sadowski, T., “FE Modeling Of Delamination Growth In Interlaminar Fracture Specimens”, Budownictwo i Architektura 2 (2008) 95-109

[43] Orifici, A.C., Herszberg, I., Thomson, R.S., “Review of Methodologies For Composite Material Modeling Incorporating Failure”, Composite Structures 86 (2008) 194–210

[44] Krueger, R., “The Virtual Crack Closure Technique History, Approach and Applications”, NASA/CR-2002-211628

[45] Zafošnik, B., Ren, Z., Ulbin, M., Flašker, J., “Evaluation Of Stress Intensity Factors Using Finite Elements”, http://www.fenet.org/downloads/FENet_Meetings/Trieste_Italy_Sep_2002/ FENET_Trieste_Sept2002_DLE_Zafosnik.pdf (03 December 2013)

[46] Dieter, G.E., “Mechanical Metallurgy” – SI Metric Edition, McGraw-Hill Bok Company

[47] Dugdale, D.S., “Yielding Of Steel Sheets Containing Slits”, Journal of Mechanics and Physics of Solids, 8,100–104, 1960

[48] Barenblatt, G., “The Mathematical Theory of Equilibrium Cracks in Brittle Fracture”, Adv. Appl. Mech. 7, 55–129, 1962.

[49] Hillerborg, A., Mode´er, M., Petersson, P.E., “Analysis of Crack Formation and Crack Growth In Concrete By Means Of Fracture Mechanics And Finite Elements”, Cement Concr. Res. Vol. 6, 773–782, 1976

[50] Alfano, M., Furgiuele, F., Leonardi, A., Maletta, C., Paulino, G.H., “Fracture Analysis of Adhesive Joints Using Intrinsic Cohesive Zone Models”, Atti del Congresso IGF19 Milano, 2007

[51] Chowdhury, S.R., Narasimhan, R., “A Cohesive Finite Element Formulation For Modeling Fracture And Delamination In Solids”, Sādhanā, Vol. 25, Part 6, December 2000, pp. 561–587

[52] Tvergaard, V., Hutchinson, J.W., “The Relation Between Crack Growth Resistance And Fracture Process Parameters In Elastic-Plastic Solids”, J. Mech. Phys. Solids Vol. 40, No. 6, pp. 1377-1397, 1992

[53] Zimmermann, K., Zenkert, D., Siemetzki, M., “Testing and Analysis of Ultra Thick Composites”, Composites: Part B 41 (2010) 326–336

[54] Alfano, G., Crisfield, M. A., “Finite Element Interface Models For The Delamination Analysis Of Laminated Composites: Mechanical And Computational Issues”, Int. J. Numer. Meth. Engng 2001; 50:1701-1736

[55] Davies, G.A.O., Ankersen, J., “Virtual Testing Of Realistic Aerospace Composite Structures”, J Mater Sci (2008) 43:6586–6592

[56] Turon, A., Dávila, C.G., Camanho, P.P., Costa, J., “An Engineering Solution for solving Mesh Size Effects in the Simulation of Delamination with Cohesive Zone Models”, http://ntrs.nasa.gov/archive/nasa/casi.ntrs.nasa.gov/ 20070038334_ 2007037796.pdf

[57] Camanho, P.P., Dávila, C.G., De Moura, M. F., “Numerical Simulation of Mixed-mode Progressive Delamination in Composite Materials”, Journal of Composite Materials, Vol. 37, No. 16, 2003

[58] Rao, V.V.S., Veni, K.K., Sinha, P.K., “Behavior of Composite wing T-joints in Hydrothermal Environments”, Aircraft Engineering and Aerospace Technology, Volume 76, Number 4, 2004, pp. 404–413

[59] Benzeggagh, M.L., Kenane, M., “Measurement Of Mixed-Mode Delamination Fracture Toughness Of Unidirectional Glass/Epoxy Composites With Mixed-Mode Bending Apparatus”, Composites Science and Technology 56 (1996) 439-449

[60] Inglis C.E., “Stress in a Plate Due To the Presence of Cracks and Sharp Corners”, Transactions of the Institute of Naval Architects, Vol.55, 1913, pp. 219-241

[61] Trask, R.S., Hallett, S.R., Helenon, F.M.M., Wisnom, M.R., “Influence Of Process Induced Defects On The Failure Of Composite T-Joint Specimens”, Composites: Part A 43 (2012), pp. 748–757

[62] efunda, Introduction to Fracture Mechanics, http://www.efunda.com/ formulae/solid_mechanics/fracture_mechanics/fm_intro.cfm (8 November 2013)

[63] Eleni Chatzi, “The Finite Element Method for the Analysis of Non-Linear and Dynamic Systems Presentation”, http://www.ibk.ethz.ch/ch/education/femII/ education/index_EN/Lecture2.pdf (05 January 2013)

[64] Barsoum, R.S. “On The Use Of Isoparametric Finite Elements In Linear Fracture Mechanics”, International Journal For Numerical Methods In Engineering, Vol. 10, 25-37 (1976)

[65] Firehole Composites, Analysis Software and Services, “Guidelines for Determining Finite Element Cohesive Material Parameters”, http://info.firehole.com/Portals/161239/docs/ guidelines-for-coheseive-parameters_ ebook.pdf (12 December 2013)

[66] Chen, J., Fox, D., “Numerical investigation into multi-delamination failure of composite T-piece specimens under mixed mode loading using a modified cohesive model”, Composite Structures 94 (2012), 2010–2016

[67] Chen, J., Ravey, E., Hallett, S., Wisnom, M., Grassi, M., “Prediction of Delamination in Braided Composite T-piece Specimens”, 16th International Conference on Composite Materials, Kyoto, Japan, 2007

[68] Belytschko, T., Gracie, R., Ventura, G., “A Review of Extended Generalized Finite Element Methods for Material Modeling”, Modelling and Simulation in Materials Science and Engineering Volume 17, 043001, 2009

[69] Hellen, T.K., “On the Method of Virtual Crack Extensions”, International Journal For Numerical Methods in Engineering, Vol. 9, 187-207 (1975)

[70] Reeder, J. R., Crews, J. R., “Mixed-Mode Bending Method for Delamination Testing”, AIAA Journal, Volume 28, Number 7, July 1990, Pages 1270—1276.

[71] Psarras, S., Pinho, S.T., Falzon, B.G., “Damage-Tolerant Design of Stiffener Run-Outs: A Finite Element Approach”, InTech, 2012